Ground-based remote sensing of methane - estimating emissions on facility and regional scales

Andreas Luther

München 2021

Ground-based remote sensing of methane - estimating emissions on facility and regional scales

Andreas Luther

Dissertation
an der Fakultät für Physik
der Ludwig–Maximilians–Universität
München

vorgelegt von
Andreas Luther
aus Ingolstadt

München, den 8. April 2021

Erstgutachter: Prof. Dr. André Butz
Zweitgutachter: Prof. Dr. Mark Wenig
Tag der mündlichen Prüfung: 9. Juni 2021

Zusammenfassung

Atmosphärisches Methan (CH_4) verursacht den zweitgrößten Strahlungsantrieb der langlebigen Treibhausgase. CH_4 Konzentrationen in der Erdatmosphäre sind seit dem Jahr 1750 um einen Faktor von ca. 2.5 gestiegen. Die Quellabschätzung und Bestimmung ist entscheidend, um den Einfluss der anthropogenen Emissionen auf den globalen Klimawandel zu verstehen. CH_4 Emissionen, die bei der Kohleproduktion entstehen, sind eine der Hauptquellen für anthropogenes CH_4 in der Atmosphäre. Polen ist der größte Steinkohle Produzent in der EU und der Großteil der Kohle wird im Oberschlesischen Kohlerevier (OK) abgebaut. Beim Kohleabbau wird CH_4 direkt am Flöz emittiert und aus Sicherheitsgründen aus der Mine ventiliert. Verschiedene Emissionsinventare schätzen die Methanemissionen des OK zwischen $344\,\mathrm{kt\,a^{-1}}$ (EUROSTAT, 2020b) und $720\,\mathrm{kt\,a^{-1}}$ (Janssens-Maenhout et al., 2017). Diverse, kürzlich erschienene Studien (Luther et al., 2019; Kostinek et al., 2020; Fiehn et al., 2020) legen eine generelle Übereinstimmung der abgeschätzten Emissionen mit dem European-Pollutant Release and Transfer Register (E-PRTR 2014) nahe ($466\,\mathrm{kt\,a^{-1}}$). Während der *Carbon dioxide and Methane Mission 2018* (CoMet), wurden fünf, tragbare, bodengestützte, direkt gegen die Sonne messende, Fourier Transformation infrarot Spektrometer (FTS) im OK installiert. Eines der Instrumente wurde auf der Ladefläche eines Kleintransporters befestigt, um stop-and-go Messungen im Lee von einzelnen Minen-Belüftungseinrichtungen durchzuführen. Dabei wurde die emittierte CH_4-Fahne im Abstand von ca. 1 bis 10 km zur Quelle durchquert. Mit Hilfe einer Massenbilanz-Methode und Wind-Information von drei 3D Wind Lidaren, wurde die Emission mit z. B. $6 \pm 1\,\mathrm{kt\,a^{-1}}$ für einen einzelnen Schacht und mit $109 \pm 33\,\mathrm{kt\,a^{-1}}$ für eine kleine Gruppe von Schächten abgeschätzt. Die Fehler, die durch Unsicherheiten der Windbestimmung zustande kommen, belaufen sich typischerweise auf 20%.

Die anderen vier FTS wurden in den vier Himmelsrichtungen in ca. 50 km Abstand zum Zentrum des OK platziert. Das Instrument im Luv maß das Hintergrund-CH_4. Das Instrument im Lee maß Hintergrund und die emittierte Überhöhung. Die Differenz der beiden Messungen ergibt die Methanemissionen, welche aus dem OK stammen. Modellläufe mit WRF (Weather Research and Forecast Model), verbessert durch die Assimilierung von 3D Wind Lidar Daten, treiben ein Lagrangesches Dispersionsmodell (FLEXPART) an, um die Methanverteilung zu simulieren. Die Residuen zwischen simulierten und gemessenen CH_4 Überhöhungen werden mit einer Phillips-Tikhonov regularisierten, nicht-negativen Methode der kleinsten Quadrate minimiert. Dabei werden die E-PRTR Daten als a-priori Information verwendet. Die Regularisierungsparameter werden graphisch mittels der L-Kurven bestimmt. Die atmosphärische Variabilität wird durch ein Ensemble aus verschiedenen Modellläufen mit leicht veränderten meteorologischen Parametern repräsentiert. Eine von sechs Fallstudien stimmt mit den E-PRTR Abschätzungen überein. Die anderen fünf Fallstudien schätzen die Emissionen der beobachteten Regionen 1.4 bis 3 mal höher ein als das E-PRTR berichtet. Die durch das Modell-Ensemble eingeführten Fehler variieren zwischen 10% und 32%.

Damit wurde gezeigt, dass die mobile Massenbilanz-Methode und die, auf einem stationären Messnetzwerk basierende Modellmethode im Prinzip mit Fehlern in der Größenordnung von 20 % funktionieren und zur Verifikation von instantanen Emissionen, sowohl von einzelnen Quellen, als auch von regional gruppierten Quellen angewendet werden können.

Abstract

Atmospheric methane (CH_4) causes the second largest radiative forcing of the long living greenhouse gases. The methane concentration in the Earth's atmosphere increased by a factor of roughly 2.5 since 1750. The quantification of methane sources is crucial to understand the underlying carbon cycle and hence, the impact of anthropogenic emissions on the global changing climate. Methane emissions from coal production are one of the main sources of anthropogenic CH_4 in the atmosphere. Poland is the largest hard coal producer in the European Union with the Polish area of the Upper Silesian Coal Basin (USCB) as the main part of it. During the coal mining process, methane is emitted from the coal bed and vented through exhaust shafts to keep the mine safe for workers. Different inventories estimate the emission of the USCB between $344\,\mathrm{kt\,a^{-1}}$ (EUROSTAT, 2020b) and $720\,\mathrm{kt\,a^{-1}}$ (Janssens-Maenhout et al., 2017). However, recent studies (Luther et al., 2019; Kostinek et al., 2020; Fiehn et al., 2020) show a general agreement with the E-PRTR inventory, which suggests $466\,\mathrm{kt\,a^{-1}}$ (E-PRTR 2014) for the USCB. During the Carbon dioxide and Methane Mission 2018 (CoMet), five portable, ground-based, direct sun-viewing Fourier transform infrared spectrometers (FTS) are deployed in the USCB. One instrument is mounted on a truck to perform stop-and-go measurements downwind of single facilities by crossing the emitted methane plumes in 1 to 10 km distance. With a mass balance approach making use of wind information from three co-deployed 3D wind lidars, the emissions of the coal mine ventilation shafts are estimated ranging from $6 \pm 1\,\mathrm{kt\,a^{-1}}$ for a single shaft to $109 \pm 33\,\mathrm{kt\,a^{-1}}$ for a small group of shafts. Wind-related relative errors on the emission estimates typically amount to 20 % for the mobile instrument approach.

The other four FTS are deployed in the four cardinal directions around the USCB in approx. 50 km distance to the center of the basin. The upwind instrument measures the background methane information from which the downwind observations are deducted to receive regional methane enhancements. WRF (Weather Research and Forecast) model runs with assimilated 3D wind lidar data feed a Lagrangian particle dispersion model (FLEXPART) to simulated the methane distribution. The residuals between simulated and measured enhancements are minimized with a Phillips-Tikhonov regularized, non-negative least squares approach using the E-PRTR inventory data as a-priori information. The regularization parameters are graphically chosen via L-curve determination. Atmospheric variability is expressed through an ensemble of different model runs, each with altered, basic meteorological parameters. One of six case studies agree with the E-PRTR estimates. The other five case studies suggest 1.4 to 3 times higher emissions than reported by the E-PRTR. The errors introduced by the model ensemble range between 10 % and 32 %.

The functional principle of the mobile mass balance method and the model approach based on stationary network observations could thus be demonstrated. With general errors amounting to 20 %, the two methods may be applied to verify instantaneous emissions on facility scale as well as on regional scale.

Contents

Chapter 1

Introduction

Methane (CH_4) is an important greenhouse gas. Since pre-industrial times its concentration in the Earth's atmosphere increased by a factor of 2.5 from roughly 720 ppb to about 1867 ppb in 2019 (Dlugokencky, 2019) – an unprecedented high value during the last 800 000 years, at least. Anthropogenic influence on this rise is proven (e.g. Bousquet et al., 2006; Loulergue et al., 2008; Kirschke et al., 2013; IPCC, 2013; Nisbet et al., 2014; Conley et al., 2016; Schwietzke et al., 2016; Worden et al., 2017; Alvarez et al., 2018; Saunois et al., 2020; Hmiel et al., 2020).

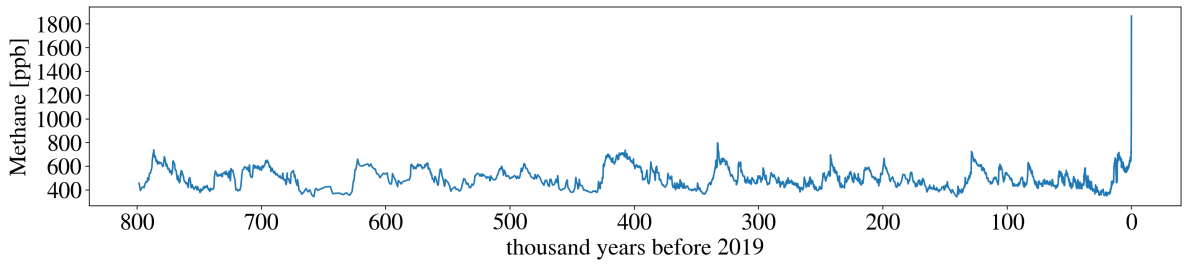

Figure 1.1: Measured methane concentration in the Earth's atmosphere for the last 800 000 years. Data from Loulergue et al. (2008); Etheridge et al. (1998); Dlugokencky (2019).

Figure 1.1 displays methane data dating back about 800 000 years. Loulergue et al. (2008) measured air trapped in ice cores from Antarctica and they were able to reconstruct the methane concentration of the Earth's atmosphere from the last 800 000 years to roughly 1000 years before present. The methane concentration from 1000 years before present to 1983 is measured in air trapped in ice cores from East-Antarctica and Greenland (Etheridge et al., 1998). Since 1983 the methane concentration is globally monitored at several sites and in different countries. Periodical patterns which occur roughly every 100 000 years represent glacial-interglacial transitions with concentrations ranging from about 380 ppb to nearly 800 ppb which is by far lower than concentrations nowadays ($\approx$ 1867 ppb in 2019 (Dlugokencky, 2019)).

Although the methane concentration in the Earth's atmosphere is rising since 1750, there was a short period between 1999 and 2006 when the rise halted. The reasons for that are still unknown and the methane budget seems to be poorly understood. As human activity is responsible for roughly two-thirds of the methane emissions, anthropogenic influence is likely involved in the renewed rise since 2007 (Bousquet et al., 2006; Kirschke et al., 2013; Schwietzke et al., 2016; Nisbet et al., 2016; Helmig et al., 2016; Worden et al., 2017). Methane observations are important to better understand the underlying processes.

After carbon dioxide (CO_2), methane causes the second largest radiative forcing of the long-lived greenhouse gases, ahead of the third important greenhouse gas nitrous oxide (N_2O). Water vapor is not considered here although it causes most of the greenhouse effect, but – except for rising temperatures causing more water to vaporize – its atmospheric cycling is too fast for human activity to have a substantial direct effect on concentrations. Radiative forcing measures the instantaneous amount of energy (in units of $\mathrm{Wm^{-2}}$), added to the Earth's energy budget – nowadays compared to preindustrial times. Greenhouse gases absorb and emit thermal radiation and hence, influence the radiation budget. When more greenhouse gases are available less energy is radiated into space which results in a heat input to the Earth system and a positive radiative forcing. Natural changes connected to sun activity are with $+0.05\,\mathrm{Wm^{-2}}$ to $+0.1\,\mathrm{Wm^{-2}}$ small compared to the current net human induced radiative forcing of over $+2\,\mathrm{Wm^{-2}}$ (IPCC, 2013). The Earth's surface temperature changes with about $+0.8\,\frac{\mathrm{K}}{\mathrm{Wm^{-2}}}$ which would result in $+1.6\,\mathrm{K}$ compared to the 1750 surface temperature. About $+1\,\mathrm{Wm^{-2}}$ is caused by current methane levels directly or indirectly due to increased tropospheric ozone production and altered stratospheric water vapor (IPCC, 2013).

With its relatively short lifetime in the Earth's atmosphere of about 9 years ($CO_2 \approx 100$ years[1], $N_2O \approx 121$ years), mainly confined by the oxidation with the hydroxyl radical OH (Thompson, 1992), the warming effects of methane can potentially be mitigated in the same period, if emissions are reduced. Other, minor methane depleting processes are oxidation by methanotropic bacteria in aerated soils, chlorine and oxygen radicals in the stratosphere, or chlorine radicals in marine regions (Kirschke et al., 2013). The lifetime of methane or any other greenhouse gas also plays an important role when it comes to global warming potential (GWP). This quantity is a multiple of the heat absorbed by every greenhouse gas in comparison to how much heat the same mass of carbon dioxide would absorb. Since different gases have different lifetimes in the atmosphere, the global warming potential changes with lifetime. Methane – with a relatively short lifetime (≈ 9 years) – has a GWP of over 80 when considering a 20 years period. The number which is most prominently mentioned is a GWP of 28 for methane which refers to a 100 years time frame (IPCC, 2013).

Oxidation of methane is its predominant sink whereas its sources are numerous. Methane emissions are categorized in three groups: a) biogenic, b) thermogenic, and c) pyrogenic (Saunois et al., 2016). Under anaerobic conditions, bacteria can produce biogenic methane

[1]Note, that about 15 % to 40 % of the emitted CO_2 will remain in the atmosphere longer than 1000 years (IPCC, 2013), similar to nuclear waste lifetimes (Archer, 2005)

e.g. in wetlands, rice paddies, sewage, landfills, ruminants, and termites. It takes geological timescales to produce thermogenic methane which remains in the ground e.g. within coal beds and oil reservoirs as natural gas. Incomplete combustion is a source for pyrogenic methane.

All different sources and sinks can be estimated using two approaches: 1) *bottom-up* methods are upscaling emissions by using generalized measurements or reported company activity data and emission factors for e.g. a single ruminant, swamp, landfill, or a coal mine. The results form the basis for greenhouse gas inventories which can be used to assign emissions to e.g. a certain industry branch, a country, or a continent and to validate emission declarations within the UN Framework Convention on Climate Change (UNFCCC) (Dlugokencky et al., 2011).

2) The *top-down* approach relies on the measurements of greenhouse gases with initially unknown origin in the atmosphere. Gradients of the measured gases are then reconstructed by a variety of models and methods to find the underlying source strength.

This work will focus on top-down methods to quantify methane emissions from hard coal mines. Resulting estimates are compared to bottom-up methane inventories.

There is a variety of methane observational techniques ranging from ground-based to space-borne instruments in order to achieve top-down emission estimates. The Global Greenhouse Gas Reference Network measures the three most important greenhouse gases CO_2, CH_4, and N_2O at over 50 sites worldwide, including the Mauna Loa observatory which is known for its long-term, stable, and background-representative observations due to its remote location on Hawaii (NOAA). This ground-based network is the baseline of atmospheric greenhouse gas observations and measures the gas concentrations in the ambient air in-situ. Similar measurement techniques, also involving ambient air observations are used e.g. in handheld instruments (Chen et al., 2020), on cars (Maazallahi et al., 2019), unmanned aerial vehicles (UAV) (Berman et al., 2012; Andersen et al., 2018) and aircraft (e.g. O'Shea et al., 2014; Cambaliza et al., 2014; Conley et al., 2017; Kostinek et al., 2019; Fiehn et al., 2020; Kostinek et al., 2020). In general these instruments suck in ambient air and analyze the composition in-situ using laser based absorption spectroscopy in the infra-red wavelength range.

Another major field of greenhouse gas observations is sensing the composition of the atmosphere remotely. By using the absorbing properties of the target gases their concentration can be estimated by measuring light which is transmitted, reflected, and scattered by the Earth's atmosphere or surface. The light source is either artificial (e.g. LIDAR (Ehret et al., 2017)) or natural sunlight: the Scanning Imaging Absorption Spectrometer for Atmospheric Chartography (SCIAMACHY) is a ultraviolet (UV), visible (VIS) and near-infrared (NIR) space borne spectrometer which was operated aboard the ENVISAT satellite (Bovensmann et al., 1999; Frankenberg et al., 2005). With GOSAT (Greenhouse Gas Observing Satellite) a Fourier Transform Infrared Spectrometer (FTS) was deployed in space to measure methane with up to 10 km x 10 km spatial resolution (Yokota et al., 2004; Kuze et al., 2009; Butz et al., 2011). The TROPOspheric Monitoring Instrument (TROPOMI) is payload of the satellite Sentinel-5 Precursor (S-5 P). It marks the next generation of greenhouse gas remote sensing with a spatial resolution of 7 km x 3.5 km

(Veefkind et al., 2012; Butz et al., 2012). Observations from passive, space-based instruments rely on sunlight backscattered to space by the Earth's surface and atmosphere where scattering effects (by e.g. aerosols) may alter the lightpath introducing a systematic bias (Butz et al., 2010).

Ground-based remote sensing of direct sunlight has the advantage of a simpler light path compared to satellite light path geometry as the light travels through the Earth's atmosphere only once until it reaches the detector. The Total Carbon Column Observing Network (TCCON) employs 25 ground-based FTS located all around the globe. These instruments record direct solar radiation spectra from which the total atmospheric columns of CO_2, CO, N_2O, CH_4, H_2O, HDO, and HF are estimated. These observations are the reference for satellite missions and complement the ground-based in-situ measurements (Wunch et al., 2011). Recently, Frey et al. (2019) tested a more compact generation of FTS spectrometers for long-term stability with the aim of supplementing the TCCON network in remote areas – the so called Collaborative Carbon Column Observing Network COCCON. This network relies on portable EM27/SUN spectrometers which are also the main instrument type discussed in this work:

The sun-viewing FTS of the type EM27/SUN are developed by the Karlsruhe Institute of Technology in collaboration with Bruker Optics (Gisi et al., 2012). These instruments measure the column-averaged dry-air mole fractions of methane (XCH_4) and other gases by measuring direct-sun absorption spectra in the shortwave-infrared spectral range (around $6000\,\mathrm{cm}^{-1}$). The general performance of the EM27/SUN has been demonstrated at remote sites as the Namibian desert (Frey et al., 2021) and at polar latitudes (Jacobs et al., 2020). Further, the devices have been used to investigate site-to-site biases of the TCCCON stations (Hedelius et al., 2017). Recently, Hase et al. (2015), Vogel et al. (2019), Makarova et al. (2020), Dietrich et al. (2021) and Jones et al. (2021) combined several of these FTS instruments into ad-hoc networks in the vicinity of major cities to estimate urban CO_2 and CH_4 emissions respectively. Chen et al. (2016) and Viatte et al. (2017) estimated methane sources related to natural gas production and agricultural activity. Toja-Silva et al. (2017) verified power plant emissions with computational fluid dynamics (CFD) simulations using measurements of two EM27/SUN instruments in Munich. Klappenbach et al. (2015) demonstrated the principle of mobile deployment of an EM27/SUN on a research vessel requiring a custom-built solar tracker to compensate for the motion of the platform. Butz et al. (2017) mounted the EM27/SUN on a small truck to measure the volcanic CO_2 plume of Mt. Etna by recording plume transects in stop-and-go patterns. Kille et al. (2019) separated natural, from agricultural CH_4 emissions using a network of four EM27/SUN instruments. Shipborne measurements above the Pacific Ocean and comparison to S5P/TROPOMI data are carried out by Knapp et al. (2021).

Generally, about 20 % of the global methane source (Fig. 1.2) is thought to be caused by the fossil fuel industry (Bousquet et al., 2006; Schwietzke et al., 2016; Saunois et al., 2020).

In particular hard coal mining is an extensive source for CH_4. The EU emits less than 1% of the global anthropogenic CH_4 emissions by fossil fuel production and use, with a share of roughly 30% which is released from the Upper Silesian Coal Basin (USCB) alone,

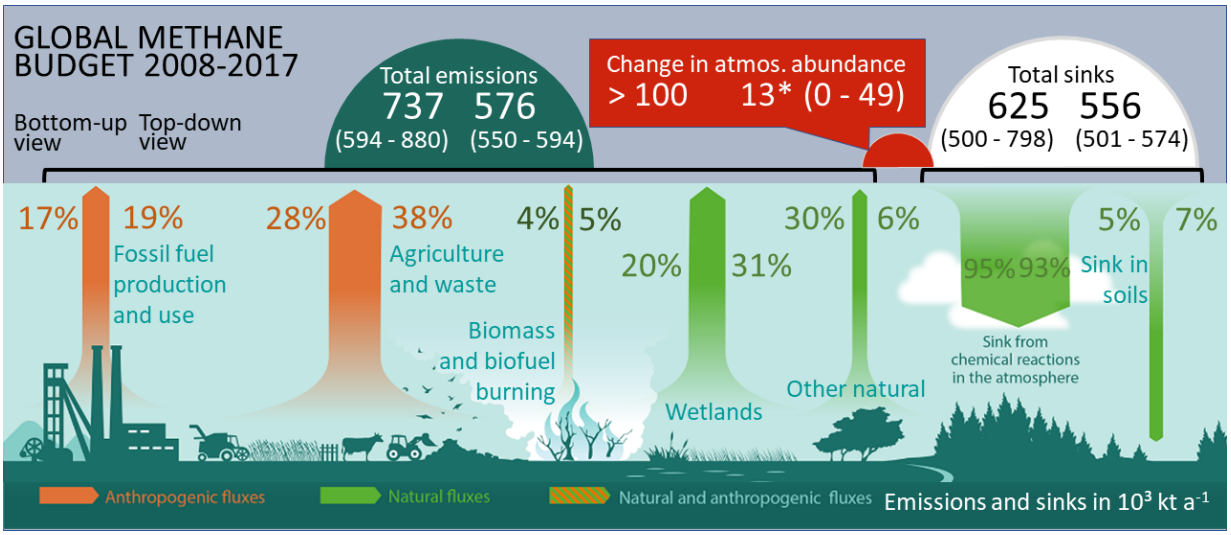

Figure 1.2: Global CH_4 budget for 2008–2017. Both bottom-up (left) and top-down (right) estimates (in $10^3\,\mathrm{kt\,a^{-1}}$) are displayed for each emission and sink category, as well as for total emissions and total sinks. "Other natural" emissions includes inland waters, geological sources, oceans, termites, wild animals, permafrost, and vegetation. * The observed growth rate is 18.2 (17.3 to 19) $\cdot 10^3\,\mathrm{kt\,a^{-1}}$ and differs from the top-down budget imbalance. Figure adapted from Saunois et al. (2020).

one of the biggest hard coal producing regions in Europe. The USCB roughly comprises an area of $7500\,\mathrm{km^2}$ centered at 50.1 N, 18.8 E with about 70 methane ventilating hard coal mining shafts. A variety of *bottom up* inventories report different total CH_4 emissions for the USCB:

With $720\mathrm{kt\,a^{-1}}$, EDGAR v4.3.2, the Emission Database for Global Atmospheric Research (Janssens-Maenhout et al., 2017) reports a rather high estimate compared to other inventories. The GESAPU database estimates $405\mathrm{kt\,a^{-1}}$ for 2010 (Bun et al., 2019). The Copernicus Atmosphere Monitoring Service CAMS reports $632\mathrm{kt\,a^{-1}}$ (Granier et al., 2019). Scarpelli et al. (2020) estimates 685 $\mathrm{kt\,a^{-1}}$ with an uncertainty of over 60 %. EUROSTAT (2020b) reports $344\mathrm{kt\,a^{-1}}$ for 2018 for the whole of Poland. The E-PRTR (European Pollutant Release and Transfer Register, http://prtr.ec.europa.eu/, 2014) reports emissions of $466\,\mathrm{kt\,a^{-1}}$. The highest estimate (EDGAR v4.3.2) is more than twice as high as the lowest (EUROSTAT). There is significant disagreement among the *bottom up* inventories, which requires scientific clarification in terms of *top down* approaches involving CH_4 measurements and observational based emission estimation methods.

For that reason, the European hard coal mining hot-spot, the USCB was the main target of the Carbon dioxide and Methane mission 2018 (CoMet) which covered roughly three weeks from 23 May to 12 June 2018. During CoMet, several aircraft and ground-based instruments were co-deployed to evaluate strategies on how to verify local CH_4 emissions. Several studies estimated methane emissions for the USCB that roughly agree with the E-PRTR inventory (Fiehn et al., 2020; Kostinek et al., 2020), although Krautwurst et al.

(2021) finds some discrepancies, when comparing the estimates for small groups of sources.

Here, I report on our contribution to emission estimation and to the CoMet measurement campaign based on observations of a network of four stationary and one mobile EM27/SUN. Our measurements led to facility and regional scale emission estimates which are partly published in Luther et al. (2019), the first paper on CoMet.

The remainder of this work is structured as follows: Chapter 2 introduces the Earth's atmosphere and its molecular absorption features, and gives an overview over coal mining processes. The key instrument of this work, the EM27/SUN and the corresponding spectral methane retrieval, together with basic explanations of the used atmospheric transport models are summarized in Chapter 3. Chapter 4 reports on CoMet0.5, the pre-survey of CoMet, which involved three stationary and one quasi-mobile FTS spectrometer, leading to useful improvements regarding measurement and modeling strategy for the main CoMet campaign. Chapter 5 describes the emission estimation with a single mobile EM27/SUN measuring at facility scales. The results of the stationary FTS network, aiming at regional scales, are presented in Chapter 6. The emission estimations on both scales together with the scientific gain are discussed in the last Chapter 7 which also gives an outlook on what to expect from the used instruments and methods.

Chapter 2

Theoretical background

The sections 2.1 and 2.2 are based on Petty (2006), Wallace and Hobbs (2006), Wendisch and Yang (2012), and Stamnes et al. (2017) followed by a short introduction in coal mining and its emissions and impacts in section 2.3.

2.1 The Earth's atmosphere

'Our' solar system has formed 4.5 billion years ago from gravitational coalescence of dust and volatile compounds as water, methane, ammonia and other substances. A subsequent epoch of continual impacts by smaller planetesimals, led to heating and degassing which resulted in the liberation of water vapor and other substances, forming a primordial atmosphere and oceans. About 3.8 billion years ago the system stabilized and early microbes formed in the oceans. Epochs with entirely frozen oceans were rare although the luminosity of the sun was 30 % lower than today, indicating that the early Earth's atmosphere must have contained a high amount of greenhouse gases. It is assumed, that methane (CH_4) might have been the dominant greenhouse gas with concentrations of two to three orders of magnitude greater than today. Volcanism and plate tectonics continuously recycled the atmosphere with mostly steam, CO_2, SO_2, H_2, CO, H_2S, CH_4, and N_2. The rise of cyano bacteria 3 to 3.8 billion years ago led to a roughly 1.5 billion years long process to accumulate Oxygen (O_2) in the atmosphere. With Oxygen present, the Ozone (O_3) layer developed protecting the Earth's surface and early life from damaging ultraviolet (UV) radiation. Fast forward to around 2.5 million years ago, the Earth's system cooled due to a decline in CO_2 concentrations, which were about an order of magnitude higher than today. Reduced plate tectonics and therefore reduced volcanic emission of CO_2 together with an accelerated CO_2 removal due to limestone formation declined the levels of atmospheric CO_2. In the last 800 thousand years, glacial epochs alternate with interglacial epochs with recurring maximum and minimum concentrations of CO_2 and CH_4 in the atmosphere significantly lower than today (Wallace and Hobbs, 2006).

Present day global average air pressure at the surface is 985 hPa. This corresponds to roughly 5.1×10^{18} kg of different gases building the Earth's atmosphere. Segmented

into different horizontal layers structured by temperature gradient changes with altitude, it continuously expands into space until the free path length of single molecules is large enough that diffusion is more important than turbulence in terms of vertical mixing. Figure 2.1 schematically shows the Earth's radius R_e in comparison to the height of the Homosphere ($R_e + 100\,km$), the approximate orbit height of the international space station ISS ($R_e + 400\,km$), and the approximate total height ($R_e + 500\,km$) of what is considered to represent the whole Earth's atmosphere. Beyond that border, the free path length of predominantly light molecules (H, H_2, and He) is large enough, that they can eventually escape into free space during periods, when the sun is active. In the middle panel the Homosphere is shown, ranging from ground level up to about 100 km, a height, above diffusion is the dominant vertical transport process. Every distinct temperature gradient change marks the border, the so called 'pause', between two sublayers of the Homosphere which are called Thermosphere, Mesosphere, Stratosphere, and Troposphere, as seen from top to bottom, each with different properties.

Due to exponential decrease of air density with height, about 80 % of the atmospheric mass is concentrated in the lowest $\sim$ 10 km, the Troposphere. The right panel of figure 2.1 displays the schematic Tropopause, which varies mainly with latitude between about 8 km at the poles and up to 18 km at the equator. It is roughly divided into two parts: the free Troposphere above, and the planetary boundary layer (PBL) below, marked in black. The PBL height varies depending on e.g. time of the day, latitude, or meteorological parameters as temperature, pressure, or cloud cover (Wendisch and Yang, 2012). The surface directly influences the PBL, in contrast to the free Troposphere above. The PBL extends through the lowest kilometer and contains roughly 10 % of the atmosphere's mass (Holton, 1973).

99.96 % of the volume concentration of dry air in the Earth's atmosphere is shared between three gases: Nitrogen (N_2) with 78.08 %, Oxygen (O_2) with 20.95 %, and Argon (Ar) with 0.93 %. Depending on the ambient temperature and humidity, water vapor (H_2O) can amount to 5 % by volume, e.g. in the tropics. The remaining 0.04 % of the volume of the atmosphere consists, among others, of the prominent greenhouse gases Carbon Dioxide (CO_2), Ozone (O_3), Methane (CH_4), and Nitrous Oxide (N_2O) (Stamnes et al., 2017). Atmospheric concentrations of all of these gases are impacted by human influence. The amount of water vapor in the atmosphere is closely related to temperature. The higher the temperature, the more water evaporates, which results in a positive feedback loop. Human activity which rises global temperatures triggers this feedback. Combustion of fossil fuels is the main reason for a rise of anthropogenic CO_2. Livestock, landfills, natural gas, and coal mining emissions are the main sources of anthropogenic CH_4. Another, considerable methane source (roughly 2 %) is caused by a rising Termite population, spreading on cleared rain forest grounds. Agriculture is the main source of anthropogenic N_2O emissions. Nitrogen oxides (NOx) and CO emissions by motor vehicles or the industry promote the O_3 formation in the Troposphere, where it is a greenhouse gas, absorbing infrared radiation.

This work focuses on the greenhouse gas methane (CH_4) and its emissions by coal mining. I will discuss its dispersion inside the planetary boundary layer (PBL), how it can be measured with ground-based, remote sensing spectrometers within hours after release,

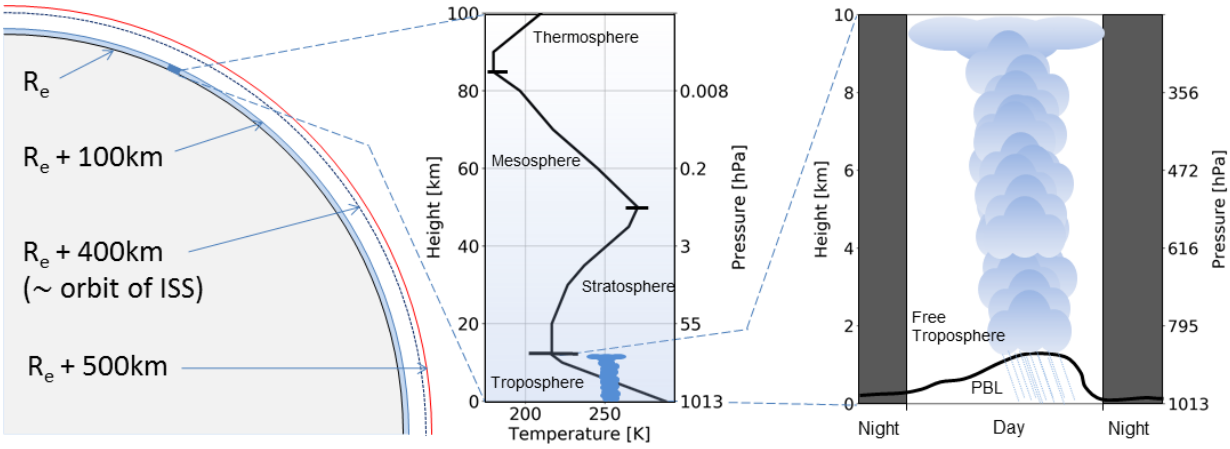

Figure 2.1: True to scale diagram of the Earth radius (R_e) with the depth of the Homosphere and the orbit of the International Space Station in the left panel. The middle panel shows the temperature profile in the Homosphere. The right panel schematically depicts the Troposphere with convective clouds during a typical mid-latitude summer storm. The black line indicates a typical daily cycle of the planetary boundary layer (PBL) which represents the height of the lowest part of the atmosphere directly influenced by the surface. Above the PBL the wind is roughly parallel to levels of the same pressure. The PBL height generally marks the level of condensation and hence, the cloud bottom height.

and finally, how one can quantitate the emission rates of single sources/facilities and groups of sources.

2.2 Molecular absorption and the greenhouse effect

H_2O, CO_2, CH_4, O_3 and other greenhouse gases only appear in traces occupying just a fraction of the total volume of the atmosphere. However, these gases interact with radiation and are responsible for almost all of the important absorption (and emission) processes in the atmosphere (Petty, 2006). Radiation cannot exchange random amounts of energy as the energy is always quantized which is formulated as $E = h\nu$, with the Planck constant h (6.626×10^{-34} J s) being the ratio of the smallest possible energy turnover E to the oscillation-frequency ν. Thus, the energy that a photon carries, is proportional to the frequency of the radiation and inversely proportional to the wavelength of the radiation (more energetic $\rightarrow$ higher frequency = shorter wavelength). A photon absorbed by a system (or a molecule), must increase the internal energy of the system by the amount of energy the photon carries. The internal energy of a gas molecule can be formulated as $E = E_t + E_r + E_v + E_e$, with *translational* kinetic energy E_t (random molecular motion, i.e. temperature), *rotational* and *vibrational* kinetic energy E_r and E_v (for polyatomic molecules), and electrostatic potential energy E_e. The *translational* kinetic energy part is unquantized (i.e. related to the temperature and speed of the observed gas molecules).

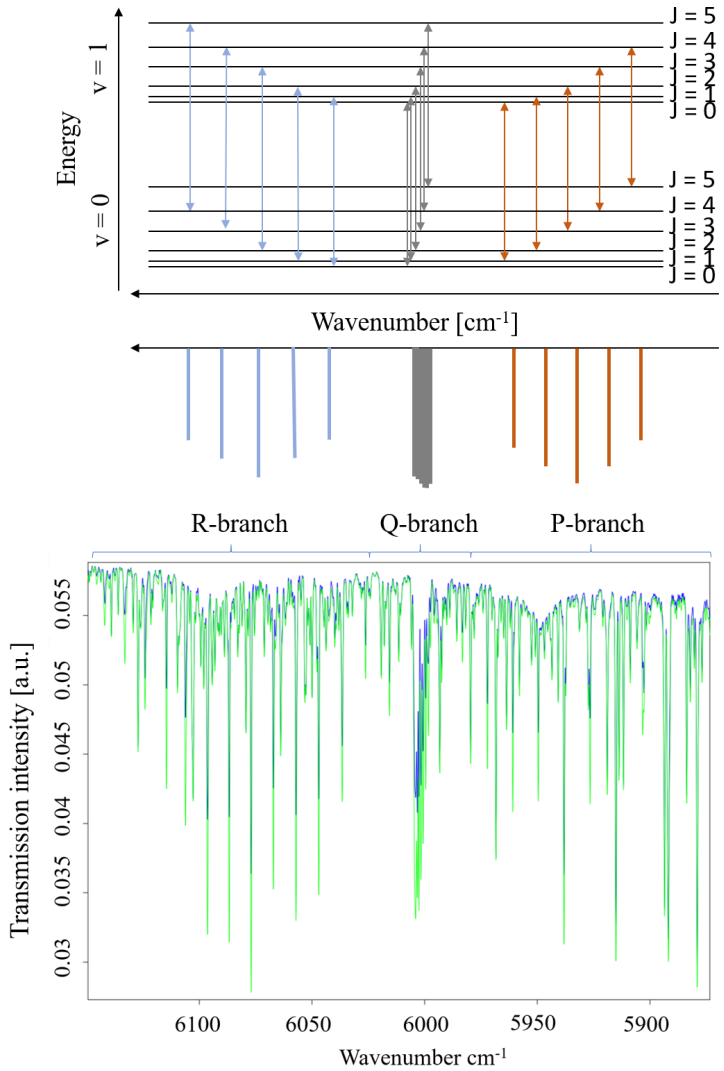

Figure 2.2: Energy transitions for the vibrational states v = 0, and v = 1 with split-up rotational states J = 0 to J = 5 for arbitrary wavenumbers in the top panel. The schematic transitions correspond to the R-branch for $\Delta J = +1$, the Q-branch for $\Delta J = 0$ where ΔE is associated with vibrational transitions, and the P-branch for $\Delta J = -1$. The middle panel depicts the corresponding schematic absorption lines with varying intensity according to its population density. The lower panel depicts two real, measured spectra (green and blue) of atmospheric total column (the light path directly to the sun) methane under similar conditions minutes apart next to a coal mine ventilation shaft. The differences in the two recorded spectra are visible with the naked eye, caused by strong methane absorption. Note, that the lower panel depicts the attribution to R, Q, and P-branch transitions in the $2\nu_3$ band around 1.6μm. This is the absorption band used for retrieving methane concentration information. The absorption band related to the greenhouse effect is located around 7.6μm - an otherwise relatively transparent part of the atmospheric spectrum.

Quantum mechanics predicts the other internal energy portions as quantized. A molecule can only have discrete vibrational frequencies, rotation rates and electronic states, and an atom can only have certain electron orbit configurations. The energy needed to change between these energy states is species-specific and constrained to certain energy levels, already hinting towards the gas characteristic absorption information used in spectroscopy to distinguish between different molecules and to measure concentrations.

In general, vibrational transitions are associated with higher energies and shorter wavelengths than rotational transitions. The vibrational absorption lines are split up into many different closely spaced rotational absorption lines. Figure 2.2 illustrates the vibrational-rotational transitions and also depicts real, measured spectra. The depicted P, Q, and R-branches pool groups of energy level transitions. Quantum mechanics and thus, Schrödinger's equation explains, that the angular momentum of a rigid molecule is restricted to discrete values which involve the rotational quantum number $J = 0, 1, 2, \ldots$. The vibrational quantum number v is also quantized and, similar to J, can only take positive integer values. Energy transitions which require higher energies, e.g. from $v = 0$ and $J = 1$ to $v = 1$ and $J = 2$ ($\Delta J = +1$) form the R-branch. Energy transitions associated with lower energies $\Delta J = -1$ form the P-branch. Vibrational transitions ($\Delta J = 0$) forming the Q-branch, are only allowed if the molecule has an angular momentum parallel to its symmetry axis. For these molecules, e.g. methane (CH_4), transitions for $\Delta J = 0$ may occur forming the Q-branch.

Absorption lines in the Earth's atmosphere are not delta-functions in wavelength as it might seem from the schematic in the middle panel of Fig. 2.2, but they undergo various broadening mechanisms. Three processes lead to a broadening of the spectral lines: **Natural broadening** ensures, that an absorption line must have a finite width, due to the Heisenberg uncertainty principle, although it is inconsequential compared to the other two broadening processes in our context. **Doppler broadening** occurs due to Doppler shifting of frequencies, at which the gas molecules receive radiation, by translational motions towards or away from the radiation source. Collisions between molecules interrupting the natural transitions and leading to a deviation of the natural line position are summarized as **pressure broadening**. The latter is the main tropospheric line broadening process. Greenhouse gases as H_2O, CO_2, CH_4, and N_2O absorb (and emit) infrared (IR) radiation influencing the Earth's system. An actually measured CH_4 atmospheric absorption spectrum incorporating all these effects is shown in the lower panel of Fig. 2.2.

The greenhouse effect

Fourier (1827) first explained, that the Earth's atmosphere acts like the glass of a greenhouse, letting through shortwave radiation but retaining the long wave radiation emitted from the ground. Arrhenius (1896) postulates that the influence of the absorbing properties of carbonic acid and hence CO_2 and water vapor in the Earth's atmosphere are *"comparatively small on the heat from the sun, but must be of great importance in the transmission of rays from the earth."*

Solar and terrestrial radiation propagate with different wavelengths (shortwave and

longwave) and thus, occur at different parts of the electromagnetic spectrum. Shortwave solar radiation which had the chance to transmit relatively free through the atmosphere (for a moment, not considering clouds, aerosols, O_2/O_3 absorption etc.), is absorbed by the Earth's surface and used to heat the surface. Then, the Earth's surface radiates thermal radiation with longer wavelengths which the greenhouse gases such as e.g. H_2O, CO_2, CH_4, N_2O, or O_3 in the Earth's atmosphere absorb. Some of the absorption bands of e.g. CO_2 at 15 µm are already saturated close to the Earth's surface, meaning, that no more IR radiation can be transmitted further than that particular atmospheric level (except, if regarding the wings of the band). But, the absorbed radiation is also reemitted in all directions. This continuously happens until a point in the atmosphere is reached, at which reduced pressure and density (and therefore CO_2 concentration) lead to unsaturated CO_2 bands again. At this point some IR radiation can finally find its way into space. The more CO_2 or other greenhouse gases are present in the atmosphere, the higher the level is, at which the terrestrial radiation can exit the atmosphere. Because the temperature of the relevant atmospheric levels decreases with height, the finally emitted radiation corresponds to lower temperatures compared to an atmosphere containing less greenhouse gases. The sun still delivers the same amount of radiation but the Earth emits with a lower temperature, which describes a net warming of the Earth as the input is greater than the output.

Methane consists of five atoms, four H, and one C. The number of vibrational modes for this nonlinear molecule is nine. Due to its symmetry five of these modes are equivalent. Two of the remaining modes have a measurable impact on outgoing longwave fluxes in the Earth's atmosphere around 3.3 µm and 7.6 µm. The latter absorption band is located in an otherwise relatively transparent region of the atmospheric spectrum giving rise to the high influence in IR absorption of methane, making it the second strongest greenhouse gas of the long-lived greenhouse gases. The strongest, long-lived greenhouse gas is CO_2. Its absorption band around 15 µm is saturated (already after a few meters above the ground) and positioned close to the longwave emission maximum of the Earth's atmosphere. Both species, CO_2 and CH_4 absorb infrared light at wavelengths close to the *atmospheric infrared window*, which roughly is in the region between 8 and 14 µm. In this *window*, H_2O does generally not absorb in the IR and especially in dry air the window is expanded to its edges, where CH_4 and CO_2 have their absorption bands. The atmospheric IR window is important for the Earth's energy budget. With rising greenhouse gas concentrations, the transmission of longwave radiation through the atmospheric window is decreased, which leads to a net warming as explained above.

With his calculations Arrhenius (1896) predicts a $+5^\circ$ C to $+6^\circ$ C warming for a doubled atmospheric CO_2 concentration which for that time corresponds to a rise from roughly 280 to 560 ppm. These results were fortuitous due to still inaccurate spectroscopic parameters, but the calculated temperature increase roughly agrees to modern climate model simulations. However, the author also expects the CO_2 concentration doubling process to take about 3000 years based on the CO_2 production of the nineteenth century. About 120 years later the value reaches 413.3 ppm in October 2020 which is nearly 75 % of 560 ppm. With the 2019 CO_2 growth rate of 2.56 ppm per year the doubling of the CO_2 concentration compared to values at the time of Arrhenius is reached in 61 years from 2020 on.

2.3 Coal mining emissions and impact

When observing coal mining emissions, questions arise about the technical and physical basis of the ventilation process. The present chapter addresses the gas composition in coal mines and how these gases form and the reasons for ventilation. Section 4.1 introduces detailed USCB-specific coal mining information and discusses the physical properties of the exhaust air.

There are several, for humans hazardous, gas mixtures which can occur during the process of underground coal extraction, containing gases such as CH_4, CO_2, O_2, N_2, H_2, He, and varying Hydrocarbons as well as CO, NO, and NO_2, with the latter three mainly emitted by mining equipment or explosives (Kim, 1973; Dahmann et al., 2009). These gases are known to form explosive mixtures or cause asphyxiation due to insufficient oxygen supply. Due to safety reasons for miners, these gases need to be ventilated out of the mines and are - in general - released into the atmosphere without further processing.

Coal-bed gas forms through abiotic and biotic breakdown of organic carbon (the main component of coals). The formation of large coal beds (and thus, carbon) began with the significant deposition of plant communities which later transitioned into peat deposits and finally coal. Massive plant expansion and diversification needed to build such peat reservoirs began in the Middle Devonian (roughly 400 Ma ago). The European coals are attributed to the Upper Carboniferous and beginning Permian (roughly 300 Ma ago) (Strąpoć et al., 2011). Depending on e.g. flora, climatic influences, and tectonics the character of the peat and therefore the resulting coal significantly varies. The formation of e.g. good-quality coal (low-sulfur, low-ash) benefits from ombrothrophic, rain-fed, and domed mires (Strąpoć et al., 2011).

The coal forming process starts as soon as plant waste or cattle manure deposits and is buried. The coalification process from Peat to Lignite, Subbituminous, Bituminous, and finally high rank coals such as Anthracite requires heat, pressure and geological timescales. The methanogenesis rate as well as the coal fraction that is convertible to methane is dependent on the coal rank. Low rank coals (generally younger and closer to the Earth's surface) show high methanogenesis and also a high fraction of coal that is convertible to CH_4. However, methane generally escapes more likely from layers close to the Earth's surface than from deeper layers, where the produced methane is trapped. This results in lignite (brown coal) mining emitting vanishingly low amounts of methane compared to hard coal mining (Thakur et al., 1994).

There are two processes forming coal bed methane: (i) Bacteria first degrade and then ferment the coal to methyl compounds, CO_2, H_2, and Acetate. In a next step, Archaea produce **biogenically** formed methane. (ii) **Thermogenic** coal bed methane is formed through pressure and heat in the course of geological time scales (Davis and Gerlach, 2018). The former occurs in 'under mature' coals (low rank). Thermogenic gas is the result of a chemical devolatilization (pyrolysis) that releases CH_4. Methane is primarily stored in coal through adsorption onto the coal surface; thus the pore surface area determines the maximum gas holding potential of a reservoir.

With concentrations up to 95 % directly in the coal bed, methane is considered as one of the main hazards in mining operations. Some of the mining air with methane concentrations as high as $> 30\,\%\,CH_4$ may further be processed for industrial usage. However, about 70 % of methane emissions from coal mining are ventilated in low concentrations of 0.1 to 1.5 % within the mining exhaust air as so called ventilation air methane (VAM) (Karakurt et al., 2011). Methods to increase the methane concentration in VAM in order to use it in industrial processes and thus, mitigate parts of its greenhouse effect are studied but not yet viable (Karakurt et al., 2011; Kurnia et al., 2019). From a global warming potential perspective, combustion of methane is preferred over ventilating it into the atmosphere as the combustion releases CO_2 which is a greenhouse gas itself but with less global warming potential than CH_4. However, ventilation is the standard procedure to reduce the hazards for mining workers.

In general, a single mine uses more than one ventilation shaft facility allocated at different locations depending on the underground spread of the mining activities. In addition, every mine also operates fresh air inlet facilities. Ventilation facilities do not all have the same appearance but in general have the ability to suck out air of the mine. Referring to a coal mine ventilation shaft in this work always refers to such a ventilation facility, where all possible single exhausts are pooled.

In addition to the global impact of ventilating methane to the atmosphere partly causing global warming, coal mining also has several implications on the local scale which are briefly discussed in relation to Poland and the USCB: The coal mining industry in Poland (including lignite and hard coal) employed nearly 82 thousand citizens of about 15.6 million total employees in Poland (roughly 0.5%) in 2018 (National Census of Population and Housing 2021). It is an economic key component and the main reason why Poland has a relatively low (but recently ascending) energy import dependency level of about 40 % compared to other EU states, e.g. Germany with roughly 60 % (EUROSTAT, 2020a). Besides the global warming potential, coal mining activity has seismic impacts (Stec, 2007), deteriorates the ground water and impacts human health mainly due to weathering processes of solid waste rock on coal mine dumping sites (Szczepanska and Twardowska, 1999; Antoszczyszyn and Michalska, 2016). The last deadly incident in the USCB happend on May 5, 2018 in the Zofiowka mine due to an earthquake and cost the lives of five miners (Polandin, 2018). The last methane explosion in the USCB happened in 2009 with 20 dead workers (BBC, 2009; Wikipedia, List of mining disasters in Poland, 2020).

Chapter 3

Measurements, methods and models

Under climate change forced by greenhouse gas emissions, observations of these gases are key to measure the status quo and to better understand the underlying biogeochemical cycles. Gases such as CO_2 and CH_4 are emitted by anthropogenic as well as natural sources and transported by winds to spread around the globe. The basis for robust emission estimates are accurate measurements of the abundances of the respective atmospheric constituents and related tracers, along with a detailed knowledge about meteorological parameters. A variety of different instruments and techniques exists, be it ground-based, airborne, spaceborne or passive and active remote sensing or in-situ measurements. This work focuses on ground-based, passive remote sensing of methane emitted by point sources and how the methane is dispersed by the local wind field. For this purpose, four stationary and one mobile FTS are deployed in the target region, the USCB in Poland.

Section 3.1 explains this spectrometer EM27/SUN used for all discussed CH_4 measurements. An introduction to the underlying principle of Fourier transform infrared spectroscopy is summarized in section 3.2. The spectral methane retrieval with the basics of Phillips-Tikhonov regularization is discussed in section 3.3. For the regional scales, where multiple sources can contribute to the observed concentration enhancement and where we need to consider a complex wind field pattern between the sources and the measurement stations, we need to model air parcel trajectories in detail. To this end, an Eulerian weather model (WRF, section 3.4) and a Lagrangian particle dispersion model (FLEXPART, section 3.5) are combined to track the path of CH_4 molecules from their source to their destination above the measurement instruments.

3.1 The Bruker EM27/SUN spectrometer

Developed by the Karlsruhe Institue of Technology (KIT) in collaboration with Bruker Optics^{TM} the EM27/SUN collects solar spectra in the range from 4000 cm^{-1} to 11000 cm^{-1}

or 2.5 µm to 0.9 µm (Gisi et al., 2012). The EM27/SUN uses a RockSolid^{TM} pendulum interferometer. The pendulum is gimbal-mounted which allows wear-free and frictionless motion. The retroreflectors move 0.45 cm against each other resulting in 1.8 cm optical path difference which maps into a spectral resolution of 0.5 cm^{-1}. A HeNe (Helium Neon) laser controls the sampling of the double sided interferograms. The instrument comes with a solar tracker to continuously feed direct sunlight into the casing and onto the pendulum interferometer. The tracker control is steered with the *CamTracker* software (Gisi et al., 2011) for the four stationary instruments, and a custom built tracker software for the mobile application (Klappenbach et al., 2015; Butz et al., 2017; Kleinschek et al., 2020; Knapp et al., 2021). An internal camera recording the spectrometer's field stop makes it possible to control the line of sight of the instrument. Other applications are e.g. open-path (Schütze and Sauer, 2016) or lunar measurements (Buschmann et al., 2017). The compact dimensions (35 x 40 x 27 cm^3) and the relatively low weight of roughly 25 kg allow for the instrument to be carried by one person. Its robust and compact design makes it suitable for measurement campaigns on moving platforms as ships or cars (Klappenbach et al., 2015; Butz et al., 2017; Kleinschek et al., 2020; Knapp et al., 2021).

Chen et al. (2016) states the precision, according to the Allan deviations, for XCH_4 for 120 s integration time with 0.3 ppb, which is about 0.02 % of the total column. The average instrument-to-instrument difference is observed to be 0.8 ppb for XCH_4 for an ensemble of instruments (Frey et al., 2019). The annual drift between the official TCCON product and the EM27/SUN is 0.9 ppb for XCH_4, which is within the 1σ precision of the comparison, 4.3 ppb for XCH_4 (Frey et al., 2019).

A sampling rate of 10 kHz and a typical coadding scheme of ten double-sided interferograms, results in one measurement per minute. However, the software needs some time during the start up of the measurement routine script which results in roughly 150 s recording duration for the very first observation of a measurement cycle. This is not problematic for the stationary instruments since the measurement cycle generally comprises all contiguous direct-sunlight hours, but needs to be considered for mobile observations, for which the start up procedure is repeated at every measurement position (see chapter 5.2).

3.2 Fourier transform infrared spectroscopy

Applications throughout the physical, chemical, and biological sciences make use of Fourier transform spectroscopy. In general, a gaseous mixture between a light source and a detector is examined by means of its light absorbing properties. In the framework of ground-based remote sensing of greenhouse gases, the light source is the sun, and the gaseous mixture consists of every molecule from the sun to the detector, which absorbs light in the spectral range of interest (for special interest in the course of this work, are the absorption features of methane and oxygen in the NIR spectral range). The remaining light forms a certain spectrum which is recorded as an interferogram by the Fourier transform spectrometer (Fig. 3.1). This section is based on Beer (1992) and Davis et al. (2001).

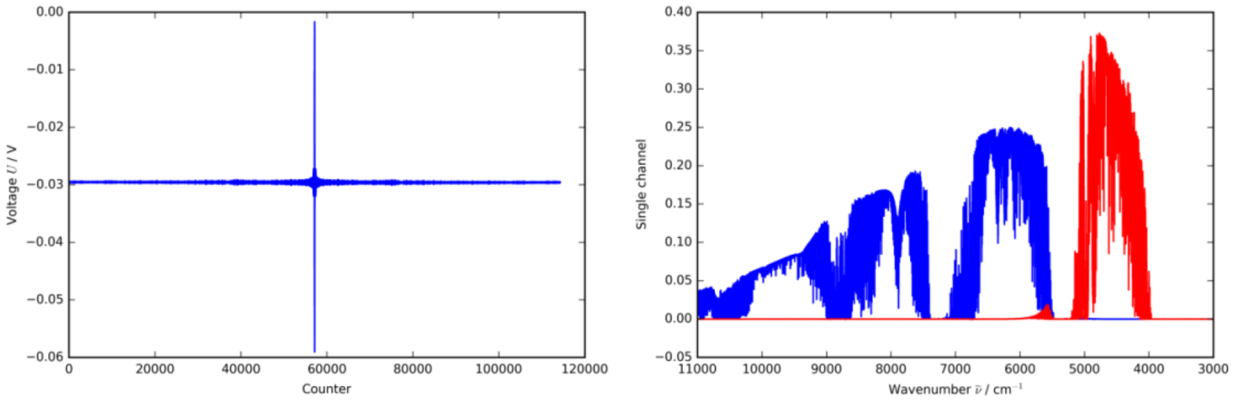

Figure 3.1: A measured interferogram (left panel) and its associated spectrum (right panel) after the Fourier transformation of the roughly $N = 12 \cdot 10^4$ sample points of the interferogram. The red part of the spectrum is measured by another detector and does not correspond with the interferogram in the left panel. The methane absorption band is located at around 6000 cm^{-1} in the right panel.

In general, the "heart" of a Fourier transform infrared spectrometer (FTS) is a Michelson interferometer. It detects an interferogram which is then Fourier transformed and analyzed for abundant gases. As schematically depicted in Figure 3.2, a light source (in this case the sun) delivers radiation with all absorption information onto a beamsplitter. One part travels to a fixed mirror, and another part of the light is transmitted through the beamsplitter and to a movable mirror. After recombining at the beamsplitter again, the light travels to the detector. The recombining process is responsible for the interference of the light which travels different distances for individual mirror positions of the moving mirror. The detector finally records an interference pattern as the intensity of the recombined light. The signal is composed of two parts, one unmodulated and thus, constant part (DC part of the interferogram) and a fluctuating part (AC part of the interferogram) which is commonly denoted as *the* interferogram. The DC part is used to filter out defective interferograms, since its baseline is indicative of source brightness fluctuations such as caused by (thin) clouds or mispointing. It is important to exactly measure the position of the moving mirror to determine the optical path difference between the light which traveled to the fixed mirror and the light which traveled to the moving mirror. Therefore, a Helium-Neon (HeNe) laser travels through the instrument and follows the same light path as the sunlight. The

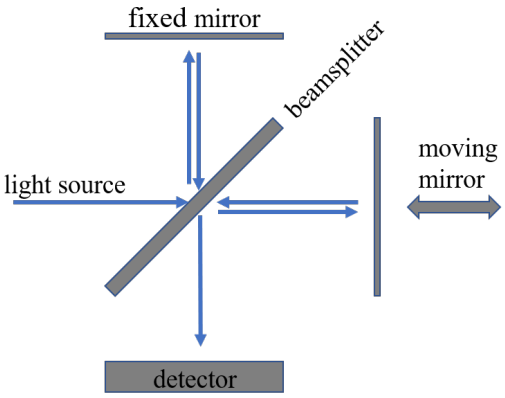

Figure 3.2: Schematic of a Michelson interferometer.

detector records a sample at each zero crossing of the laser interferogram.

All five FTS presented in this work are of the same type EM27/SUN (section 3.1), but each instrument has an unique optical alignment which individually influences the measured spectral lines, resulting in an instrument specific line shape (ILS). One part of the ILS is based on the finiteness of the interferogram due to the physical limit of the movable mirror motion and the not perfectly parallel incident radiation. The second part of the ILS describes optical misalignment. The ILS parameters of the spectrometers presented in this work, are evaluated with open path measurements of known length (stepwise 1.5 to 5 m) with an artificial light source according to (Frey et al., 2015). Throughout the discussed measurement period, the ILS is frequently measured and did not change significantly, which endorses the overall good stability of these FTS.

3.3 Spectral retrieval of Methane

The following chapter explains the principles of inversion theory and the underlying physics based on Rodgers (2000), Hase (2000) and Borsdorff et al. (2014). The technical description of the retrieval software includes parts of Luther et al. (2019). The inversion theory discussed in this work is used to calculate total column dry air mole fractions of different species in the atmosphere from FTS spectra.

For the purpose of passive remote sensing of direct sunlight, a forward model generates synthetic spectra which will be compared to measured spectra and the residuals will be minimized. A model which creates a synthetic spectrum generally needs information about the radiative transfer which is dependent on the position of the observer on the Earth's surface, the position of the sun, vertical profiles of temperature and pressure, mixing ratios of the relevant species, and the individual ILS of the instrument which measured the true spectra.

For the NIR spectral range, the atmosphere's emission is small compared to the sun's emission considering direct sun measurements. Furthermore, a direct sunlight photon is more likely to reach the detector than a scattered photon, to an extent, that scattering is negligible (in addition, the scattering of light on air molecules is described via the λ^4-dependency of Rayleigh scattering, mainly affecting the purple/blue and green parts of the visible spectral range). Scattered sunlight would need to be scattered at least twice and in the same direction as direct sunlight to reach the detector. Therefore, the general formulation of the radiative transfer reduces to Beer-Lambert's law:

$$I(\tau_\nu, \nu) = I_0(\nu)e^{-\tau_\nu} \tag{3.1}$$

with the spectral intensity I_0 which is attenuated by a medium with optical thickness τ_ν. The optical thickness τ_ν itself is dependent on the specific absorption cross section σ_i, the number density n_i for gas i, and on the slant geometric path z between the sun ($z = 0$) and the observer ($z = L$):

$$\tau_\nu = \int_0^L \sigma_i(z, \nu) \cdot n(z)dz. \tag{3.2}$$

The calculated intensity distribution as formulated in Eq. 3.1 generates the measurable spectrum $\tilde{I}(\nu_0)$ under additional consideration of the instrument's spectral response, the instrument dependent radiative contribution, and the convolution of the incident intensity spectrum $I(\tau_\nu, \nu)$ with the instrument's line shape (ILS) via a Fredholm integral of the first kind as explained in Hase (2000); Desbiens et al. (2006):

$$\tilde{I}(\nu_0) = \int_{-\infty}^{\infty} I(\tau_\nu, \nu)\, \mathrm{ILS}(\nu_0, \nu) \mathrm{d}\nu\,. \tag{3.3}$$

After discretization of the radiative transfer problem, the generated synthetic spectra are fitted to the measured spectra.

In a more generalized formulation, the forward model $\mathbf{F}$ is dependent on n quantities represented by the state vector $\mathbf{x}$, and describes the measurements $\mathbf{y}_{\mathrm{meas}}$ of dimension m, with the measurement error $\mathbf{e_y}$:

$$\mathbf{y}_{\mathrm{meas}} = \mathbf{F}(\mathbf{x}) + \mathbf{e_y}. \tag{3.4}$$

To this end, the forward model $\mathbf{F}(\mathbf{x})$ describes the discretized spectral measurement based on the physical understandings of the state. The measurement vector $\mathbf{y}_{\mathrm{meas}}$ describes the discretized wavelength as the measured IR spectrum. The state vector $\mathbf{x}$ includes the parameters to be determined, which are quantities such as the vertical methane profile, the continuum polynomial, and the spectral alignment.

After linearizing $\mathbf{F}$ around a first guess $\mathbf{x_0}$ Eq. 3.4 can be written in linear approximation as

$$\mathbf{y}_{\mathrm{meas}} - \mathbf{F}(\mathbf{x_0}) = \frac{\partial \mathbf{F}(\mathbf{x})}{\partial \mathbf{x}}(\mathbf{x} - \mathbf{x_0}) + \mathbf{e_y} = \mathbf{K}(\mathbf{x} - \mathbf{x_0}) + \mathbf{e_y} \tag{3.5}$$

leading to

$$\mathbf{y} = \mathbf{K}\mathbf{x} + \mathbf{e_y} \tag{3.6}$$

with $\mathbf{y} = \mathbf{y}_{\mathrm{meas}} - \mathbf{F}(\mathbf{x_0}) + \mathbf{K}\mathbf{x_0}$ and the m × n Jacobian or weighting function matrix (also called kernel matrix) $\mathbf{K} = \partial \mathbf{F}/\partial \mathbf{x}(\mathbf{x_0})$ in which each element represents the change of the observed quantity with respect to changes in the state vector $\mathbf{x}$. The measurement noise is described by an m × m error covariance matrix $\mathbf{S_e}$ with its diagonal elements containing the variances of each measurement value. The aim is to find a state vector $\tilde{\mathbf{x}}$, that makes the forward model $\mathbf{F}$ match the measurements $\mathbf{y}$ according to a matching criterion. A common choice for the latter is a least-squares minimization of a cost function. Since the forward model is non-linear in the state vector, the procedure requires iteration in step-wise linear approximation. Because the least-squares solution

$$\tilde{\mathbf{x}} = \min_{\mathrm{x}} ||\mathbf{S_e^{-1}}(\mathbf{K}\mathbf{x} - \mathbf{y})||_2^2 \tag{3.7}$$

with the L_2 norm $||\cdot||_2$, is not unique, the problem is often ill-posed due to the measurements providing partially redundant and erroneous information on the state.

Unrealistic oscillations in the inverted quantity may occur, leading to unrealistic, or nonphysical retrieval results. In order to avoid these solutions, the retrieval can be *regularized*. These methods use a-priori information which relies on more realistic ranges for

certain parameters. E.g. the methane concentration cannot be negative. Depending on how much influence the regularization is given, the finally retrieved solution does more or less resemble the a-priori. In this work, the Phillips-Tikhonov regularization (Phillips, 1962; Tikhonov, 1963; Twomey, 1963) is used to find a regularized solution $\tilde{\mathbf{x}}_{\mathrm{reg}}$ by minimizing the cost function

$$\tilde{\mathbf{x}}_{\mathrm{reg}} = \min_{\mathrm{x}}(\, ||\mathbf{S_e^{-1}}(\mathbf{Kx}-\mathbf{y})||_2^2 + \lambda^2||\mathbf{L}(\mathbf{x}-\mathbf{x}_{\mathrm{a}})||_2^2 \,) \tag{3.8}$$

with the regularization parameter λ and the regularization matrix $\mathbf{L}$ which weights the difference between the state vector $\mathbf{x}$ and the a-priori $\mathbf{x}_{\mathrm{a}}$. The regularization parameter λ balances the influence of the two cost function terms in Eq. 3.8. For $\lambda = 0$, the influence of the a-priori on the solution vanishes as the second term becomes zero. For large λ, the solution becomes the a-priori and all information from the measurement is lost. A common method to find an appropriate λ is the interpretation of the L-curve, which is discussed in section 6.4.

The technical implementation of the above discussed formulations necessary for this kind of spectral retrieval are split into two software blocks. The first one, CALPY (Klappenbach, 2016), filters the measured interferograms for quality by means of the unmodulated DC part. Insufficient or uneven detector illumination during the sampling process caused by passing clouds or disturbed sun-tracking, alter the DC part of the interferogram which is detected and respective measurements are removed (Klappenbach et al., 2015). If the DC fluctuation threshold of 1 % is exceeded the corresponding observation is discarded. CALPY further performs the Fourier transformation of the interferograms to calculate the spectra. It also generates the pressure-temperature profile for the different instrument locations consisting of individual in-situ surface pressure measurements and meteorological information gathered via the Goddard automailer (NASA, 2018). This is a free service of the NASA Goddard space flight center providing NCEP (National Center for Environmental Prediction) data (among others) via an automated e-mail system. Position and elevation a.s.l. are measured with GPS-receivers plugged into the measurement notebooks. This also ensures correct time signature of the measurements as the computer built-in time is updated with the GPS time and then written into the interferogram files as time of record. For the tasks connected to mobile FTS measurements, the CALPY-mobile (Klappenbach et al., 2015) version is used. In addition to CALPY, it incorporates the changing observational positions of the instrument. The software also pre-processes the data for use with the second software block PROFFIT (Hase et al., 2004) which retrieves the total column CH_4 from the measured spectra. This software is in routine use for trace gas retrievals from NIR direct-sun absorption spectra (e.g., Gisi et al., 2012; Frey et al., 2015; Klappenbach et al., 2015; Kiel et al., 2016; Butz et al., 2017; Frey et al., 2019; Luther et al., 2019). The package calculates every step from the spectrum to the column abundance of the chosen species according to the above mentioned mathematical and physical principles. In the following, the most critical technical aspects of the PROFFIT retrieval are summarized.

The most important measured species for this study are O_2 and CH_4. Their related spectral retrieval windows are 7765 to 8005 cm^{-1} and 5897 to 6145 cm^{-1} for O_2 and CH_4, respectively. Toon (2017) and Rothman et al. (2009) deliver the absorption line parameters. The vertical methane a-priori profile is extracted from an EMAC (ECHAM/MESSy Atmospheric Chemistry) simulation similar to the simulation described by Jöckel et al. (2016) and Nickl et al. (2020).

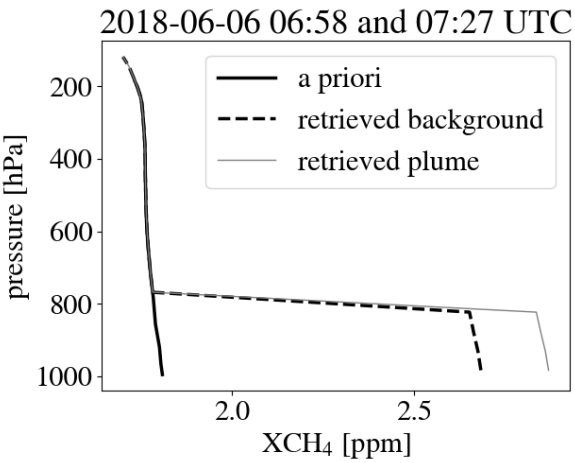

Figure 3.3: Comparison of a-priori and retrieved CH_4 profiles.

The vertical methane profile is assumed to more or less fit the a-priori above the PBL but is very much different inside the PBL as the methane emitted by sources close to the ground will generally distribute inside the PBL and the modeled profile is chosen from a background location outside the measurement area with no coal mining activities influencing it. Therefore, the PROFFIT retrieval only scales the lower part of the a-priori profile ($<$ 1700 m a.g.l) as depicted in Fig. 3.3. This step is necessary, because otherwise the retrieval would distribute the methane over the total column height, resulting in an overestimation of the retrieved CH_4 methane columns, given in units of molecules m^{-2}. This procedure is also presented in Butz et al. (2017) who only scaled the relevant plume layers of volcano Etna in Sicily. For the O_2 retrieval, the full a-priori profile is scaled. Finally, the retrieved column densities ($[O_2]$ and $[CH_4]$) are converted to the column-averaged dry-air mole fraction of methane (XCH_4) through

$$XCH_4 = \frac{[CH_4]}{[O_2]} \times 0.20942 \tag{3.9}$$

with the atmospheric O_2 mole fraction 0.20942. The XCH_4 measurements are now prepared for further processing to finally be used for emission estimation calculations.

One important assumption made in this thesis, is the uniform distribution of ventilated methane in the atmospheric boundary layer at a certain distance to the mining ventilation shafts. Although the measurement principle is sensitive to methane in the total column towards the sun, the dispersion of the relevant coal mine methane inside the boundary layer needs to be considered. The EM27/SUN measures direct sunlight and therefore, the viewing angle of the solar tracker depends on the zenith angle of the sun. The observed air column varies with latitude and time of day. This is accounted for by co-measuring the O_2 column and cancel out zenith angle and surface pressure (altitude) dependencies via Equ. 3.9. The detectable dependency for O_2 begins at solar zenith angles $\geq 80°$ (Frey et al., 2015), whereas solar zenith angles during the here reported cases did not exceed 56°.

3.4 WRF simulations

Emission estimations on regional scale require modeled wind information to drive particle dispersion in an approximately 100 km x 100 km target domain.

To this end, the Weather Research and Forecasting (WRF) model is set up. It is a widely used Eulerian numerical weather prediction system which is operated either in analysis or forecast mode. It integrates the compressible, nonhydrostatic Euler equations in flux-form which are closely related to the Navier-Stokes equations.

In this work, two different versions of WRF are used, WRF V3 (Skamarock et al., 2008) and WRF V4 (Skamarock et al., 2019). This has mainly the practical reason that WRF V4 was not yet released at the beginning of this work. The main difference between WRF V3 and WRF V4 is, that the vertical coordinate system is hybrid by default compared to terrain following in WRF V3. This generally leads to topographic effects vanishing faster with height in WRF V4 than in WRF V3. In addition WRF V4 includes e.g. optional parameterizations for radiation, cloud physics, and convection.

WRF is used in analysis mode with two different purposes:

1) WRF V3 (Skamarock et al., 2008) to directly simulate ground-based methane measurements: the built-in passive tracer option (see section 4.3) tracks user specified air parcels and disperses relative amounts of that air to neighboring grid cells according to the model's wind properties. The amounts of the initially released tracers are available for every grid cell depending on time and space. This allows to simulate measurements for each grid cell which are compared to actual observations.

2) WRF V4 (Skamarock et al., 2019) also models the local scale wind field but this time the wind fields are used as input for the Lagrangian trajectory model FLEXPART (FLEXible PARTicle dispersion model): Highly resolved wind field data computed with WRF drives the particle dispersion in FLEXPART which computes spatially highly resolved trajectories. The relevant WRF setup is explained in section 6.2.

In either way, the main purpose of WRF within this thesis is, to calculate spatially and temporally highly resolved wind information based on boundary conditions provided by the Global Forecast System (GFS) or by the European Center of Medium-Range Weather Forecasts (ECMWF), to study the evolution of methane plumes on their way from the source to the receptor measurements. GFS data is available at the NCAR/UCAR Research Data Archive at 3 hours time resolution gridded to 0.25° x 0.25°, based on NCEP GDAS/FNL Operational Global Analysis data (NCEP, 2017). The ECMWF data comprises operational analyses of the ECMWF Integrated Forecast System (IFS) with a horizontal resolution of about 16 km and a temporal resolution of 6 h (ECMWF, 2018).

To guarantee a smooth transition from the GFS (0.5° or roughly 28 km) or ECMWF (roughly 16 km) data input to temporally and spatially higher resolved domains, the grid cell size in WRF is changed step wise by a factor of 5 for each of the domains (which are also referred to as *nests*). An example of such a nested structure is depicted in the left panel of Fig. 4.5 in section 4.3. The nested domains are necessary to avoid numerical instabilities, which would occur when the discrete steps between different spatial or temporal scales do

not fit. As an example, to avoid these instabilities the Courant-Friedrichs-Lewy (CFL) condition must hold:

$$C = \frac{u\Delta t}{\Delta x} \leq C_{max} \tag{3.10}$$

With C the Courant number and C_{max} a constant depending on the problem to be solved (usually $C_{max} \approx 1$ (Holton, 1973)), the velocity norm u (windspeed), the length of the timestep that needs to be calculated, Δt, and the distance between two grid cells, Δx. It is apparent from equation 3.10 that stable numerical calculations are only possible if the timestep Δt for each calculation is reduced according to a smaller grid size (small Δx) or a faster mean flow (large u). Reducing the spatial scale generally involves a reduction of the temporal scale which makes small scale simulations time consuming.

3.5 FLEXPART simulations

FLEXPART (FLEXible PARTicle dispersion model) is a Lagrangian trajectory model that follows air parcel motion in time and space given background meteorological fields (Stohl, 1998). The trajectory of an infinitesimally small air parcel is defined by

$$\frac{d\mathbf{X}}{dt} = \dot{\mathbf{X}}[\mathbf{X}(t)] \tag{3.11}$$

with the time, t, the position vector, $\mathbf{X}$ and the wind velocity vector, $\dot{\mathbf{X}}$ (Stohl, 1998). Let the initial position be known as $\mathbf{X}_0$ at time t_0, equation 3.11 completely determines the parcel's path which leads to $\mathbf{X}(t) = \mathbf{X}(\mathbf{X}_0, t)$ (Stohl, 1998). The initial coordinates $\mathbf{X}_0$ at time t_0 are called Lagrangian coordinates and identify the parcel for all time. Initially neighboring particles will remain neighbors for all time. Trajectories also differ from streamlines which are often visualized on weather maps as the flow. A streamline gives the pure direction of the flow and although it can be parallel to some trajectories in the flow it can also differ: a streamline always adjusts to the flow whereas a trajectory might just be influenced by the flow but moving into another general direction (Stohl, 1998). This idealized concept is not fully applicable in the real atmosphere as a finite parcel may be distorted in a strongly divergent flow and separated from its neighbor. The software package FLEXPART-WRF 3.3.2 - further referred to as FLEXPART - is such a Lagrangian particle dispersion model which computes the trajectories of a large number of infinitesimally small air parcels (Brioude et al., 2013) which in this case represent methane molecules emitted by coal mine ventilation shafts. FLEXPART integrates the trajectory equation 3.11 by using the simple *zero acceleration* scheme $\mathbf{X}(t + \Delta t) = \mathbf{X}(t) + \dot{\mathbf{X}}(\mathbf{X}, t)\Delta t$ with the time increment Δt (Stohl et al., 2005).

Trajectories can be directly calculated from wind observations or, as described in section 6.2, from a numerical model output grid, in this case WRF. Highly resolved wind information from the Eulerian WRF simulations which include observational wind lidar data assimilation, drive the Lagrangian particle dispersion in FLEXPART.

Chapter 4

Pre survey CoMet0.5

The Carbon dioxide and Methane mission (CoMet) was initially planned for August 2017. The mission was postponed to May and June 2018 due to technical problems with one of the participating aircraft. However, our ground based team conducted a pre survey of the Upper Silesian Coal Basin (USCB), namely CoMet0.5, to explore different measurement procedures, identify challenges with regard to logistics and infrastructures and to asses typical methane emission scenarios. The deployment took place from 8 August to 29 August in Summer 2017. The following sections introduce the target region, the USCB (section 4.1), summarize the campaign deployment (section 4.2), explain the needs for dispersion modeling (section 4.4), and outline the lessons learned (section 4.5) with respect to the main mission CoMet (see Chapters 5 and 6).

4.1 The Upper Silesian Coal Basin

This section gives an overview of the USCB in terms of its geology and topography. Both are crucial to understand the significance of the USCB as a methane emitting source. In the south-west of Poland the USCB covers an area of roughly 7500 km^2 which makes it one of the largest coal basins in Europe. Thus, Poland is the largest hard coal producer in the EU with the USCB as the main part of it. This region lies in the western part of the sub-Carpathians subsidence between the Sudetens in the west, the Tatra in the south and the Silesian Triassic escarpments in the north-east. The USCB (Fig. 4.1) is connected to the Czech Republic via the Moravian gate in the south-west, connected to Lesser Poland with the Sandomierz Basin in the east, and opened to the north with the Silesian Lowlands. The rivers Vistula and Odra transverse the basin floor which usually lies at levels from 260 m to 290 m a.s.l. The Moravian Gate in the south-west influences the USCB climatically and biogeographically from that direction (Kondracki, 1956).

USCB coal deposits are mainly attributed to the Upper Carboniferous and attain a thickness of up to several kilometers. Recently, many mines in the USCB exceed 1000 m mining depth, which corresponds to the deep methane zone with particular high volumes of accumulated coal bed methane. Several mines (22 in 2016) extract hard coal from depths

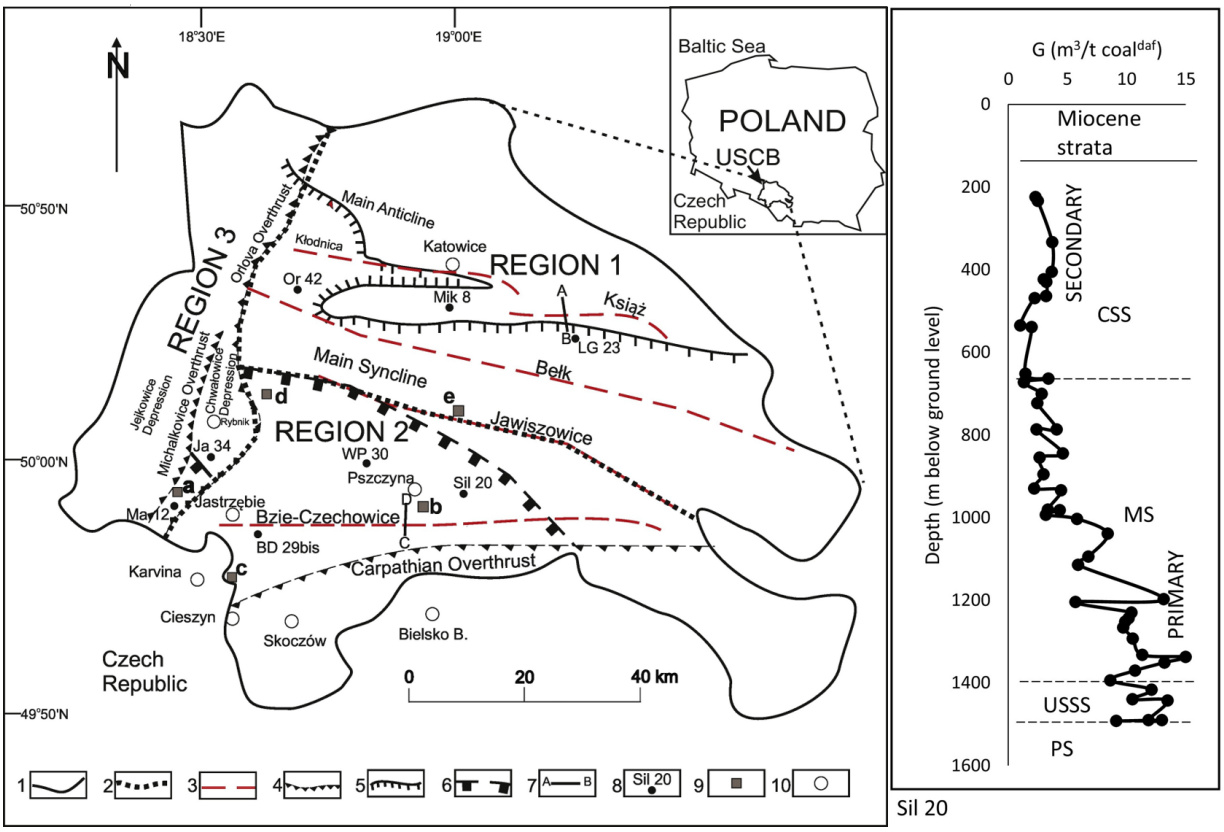

Figure 4.1: Geological map of the USCB taken from (Kędzior and Dreger, 2019). The USCB is divided into three regions with different geological settings. The measurement campaigns mainly focused on region 2 with expected highest specific emissions. The right panel displays a depth profile taken at the Silesia mine in the south-east of the USCB. It shows the rising methane content with increasing depth and clarifies, how Miocene clays (displayed as Miocene strata) may block the methane below, allowing accumulation. With increasing depth, the coal quality rises from secondary to primary coal reservoirs. Abbreviations in the right panel: CSS - Cracow Sandstone Series, MS - Mudstone Series, USSS - Upper Silesian Sandstone Series, PS - Paralic Series. Markers in the left panel: 1 - Polish USCB border, 2 - borders between the regions, 3 - fault zones, 4 - overthrusts, 5 - range of Miocene cover, 6 - range of secondary methane zone (zone with less methane content compared to primary methane zones), 7 - cross-section lines not discussed in this work, 8 - location of bore hole profiles as depicted as an example in the right hand panel, 9 - letters a to e give the location of free gas accumulations, 10 - important towns.

as low as 1300 m (Kędzior and Dreger, 2019). Methane trapped inside the coal bed is released in the course of the extraction process. In 2015 about 36 % of the total methane emissions from the USCB were captured and from that, roughly 60 % were utilized, with the remaining 40 % emitted to the atmosphere as so-called *discharge* (Kędzior and Dreger, 2019). The conditions in the mines need to be safe for workers and equipment, which is why the air is ventilated above ground through 72 exhaust shafts.

Figure 4.2 depicts such a coal mining ventilation facility. It is named "Pniowek V" and is one of three ventilation facilities of the Pniowek mine. The gases flow through the concrete corridors at the back of the building and are mixed with ambient air. In this particular case it is very likely, that the only active emitting shaft is the one in front as it also releases water vapor which condenses at the cooler air outside the mine. The condensate precipitates on the roof in the foreground of figure 4.2. Condensed water on the outlets hints towards the mining air being warmer and more humid than the ambient air. The other two chimneys seem to be inactive. As methane is invisible and odorless, the condensed water was an opportunity to visually track the plume at least for some tens of meters. The mixing process from the plume to the ground could also be observed as a methane peak measured directly on the ground with in-situ instruments as close as roughly ten meters downwind of the facility. It is assumed that the methane is also well mixed, when measuring in several kilometers distance.

Figure 4.2: Mining ventilation facility Pniowek V. Drone-footage from Kud (2017).

Figure 4.3 displays one day of CH_4 concentration measurements taken in the above pictured ventilation shaft of the Pniowek mine in the USCB. These measurements are provided by the facility operator (Swolkien, 2018) and carried out on a regular basis to quickly react and ensure safety for the miners. The accuracy of the CH_4 values is restricted to several tenths of a percent (in general methane gradients in the atmosphere are on the order of several ppb). During this particular day, the methane concentration in the vented air is not constant and may double or even quadruple within minutes. When using these data (total ventilating air flux of 14600 $m^3 min^{-1}$ and average CH_4 concentration within this air of 0.273 %) to project the measured emissions to an annual rate, it roughly reaches 1 kt a^{-1}. The E-PRTR inventory reports about 20 kt a^{-1} for this shaft. The daily, snapshot like observations, may deviate from the reported annual emissions. This is valid for operator conducted inside-shaft measurements, as well as for scientific measurements. The reliability of the comparison of observations with inventory data is an important question discussed within this thesis and summarized in Chapter 7.

Although coal production in Poland was reduced by about 50 % from 1994 to 2016, the

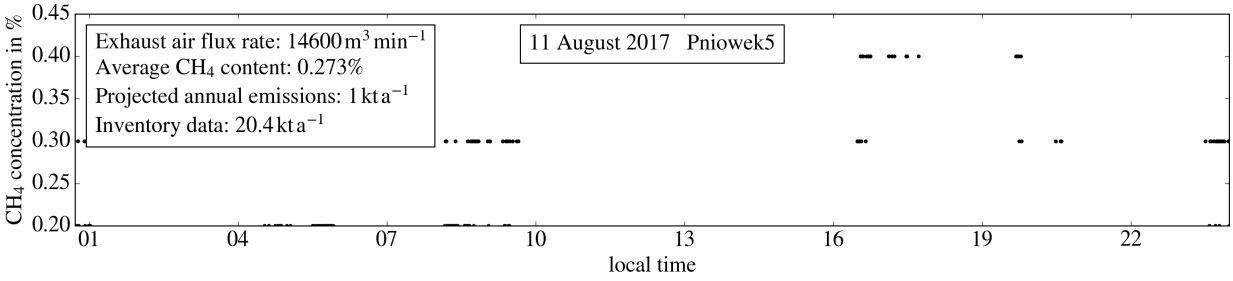

Figure 4.3: Pniowek V inside shaft methane concentration measurements for 11 August 2017. It is obvious that the data suffer from shortcomings such as too coarse digitization and intermittancy. It is hard to use them for verification of methane emissions. Data provided by Swolkien (2018).

methane emissions increased by roughly 25 % in the same period (Kędzior and Dreger, 2019; Dreger, 2020). This is generally related to deeper digging and exploitation of deep methane zones. Highly concentrated coal bed methane can be found below Miocene deposits which seal the methane preventing it from escaping into the atmosphere. Rock mass faults and relaxed zones also allow accumulation of gases. Highest total methane emissions are found in the northern part of the USCB (Region 1 in Figure 4.1). Highest specific emissions occur in the southern part (Region 2 in 4.1) where Miocene clays block the methane below. There also exists free methane under high pressure in Region 2 which is the cause for sudden methane and rock outbursts into the mines, resulting in high concentration fluctuations of the ventilated methane within minutes (Kędzior and Dreger, 2019) which influences emission estimation based on instantaneous rather than continuous observations.

4.2 Campaign deployment

CoMet0.5 focuses on one part of Region 2 in Figure 4.1. The bottom up inventory E-PRTR states the highest emissions for the mine Pniowek with three shafts in the center of Region 2 which is chosen to be the center of the measurement network. The E-PRTR lists the Pniowek CH_4 emissions with 61.8 kt a^{-1} ($\approx$ 15% of the total USCB methane emissions). The main focus is on this strong emitting sources. Figure 4.4 shows, how three stationary EM27/SUN are located in 2 – 5 km distance to the shafts in the north (Cyprianowka), south-east (Pustelnik), and south-west (Kallon). The northern instrument is placed on a farm-like Hotel surrounded by crops and forest. The south-eastern instrument (Pustelnik) is placed near a big lake next to the Vistula with low surface roughness and mainly crops in all other cardinal directions. The third instrument (Kallon) is located in a town in a dip marking the western end of the stationary measurement network.

In addition to the spectrometers, a ceilometer is installed at station Pustelnik. This 1064 nm laser based instrument of the type Lufft CHM15kx-System measures the height of the cloud base and enables the user to derive aerosol information. The initial purpose of the instrument was the detection of the planetary boundary layer height. The boundary

layer height identification was finally done visually by examining the provided ceilometer measurements. However, the data is not used for scientific applications regarding WRF modeling, but very well for general understandings of the atmospheric conditions in this area. A quicklook of the ceilometer data can be found in Appendix C.

The fourth instrument is placed on a pick-up truck for versatile applications: A) to test mobile functionality including the possibility of stop-and-go measurements, B) to act as a background or foreground sampling instrument for one of the stationary instruments under certain wind conditions. The main idea is, to measure the CH_4 total column enhancements resulting from subtracting the background methane (measured upwind) from the foreground methane (measured downwind of a mining facility). The three stationary instruments cover the north, south-east, and west-southwest of the target area. As stated in B) the mobile instrument is then moved according to the present wind direction to cover either the upwind or the downwind part of the required measurement pair.

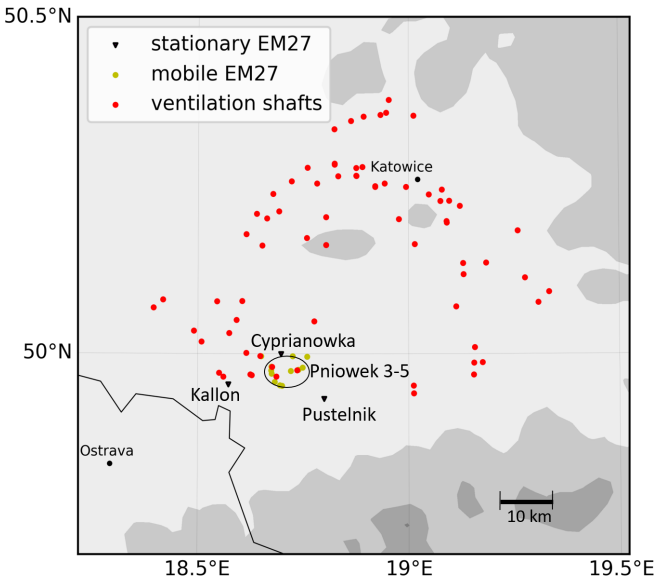

Figure 4.4: The CoMet0.5 deployment with the stationary FTS as black triangles, the ventilation shafts as red circles and the mobile instrument positions (yellow circles). Shaded areas represent elevation, e.g. the Tatra in the south ($>$ 2000m).

4.3 WRF with passive tracer

During the pre-survey mission CoMet0.5 in 2017 in the southern part of the USCB we used WRF to model wind fields and the respective methane plumes emitted by the coal mine ventilation shafts, since wind observations were not performed. WRF has a built-in method to model passive tracers which prescribes that the tracer is partly diffused into neighboring grid cells. Compared to the Lagrangian perspective (see section 3.5), which uses trajectories which are independent from grid cells, the Eulerian approach is strongly dependent on the grid cell size. One single grid cell in the Eulerian model is the smallest possible element a plume consists of. This needs to be accounted for, depending on the favored scale of the simulation. In our case, the shortest distance between a shaft and a measurement site is about 4 km when considering standard easterly or westerly wind conditions. This does not consider shafts in the north of the measurement sites as northerly winds are not expected. Thus, the spatial resolution of the model needs to be configured in a way, that the plumes are represented by more than one pixel over the distance of 4 km.

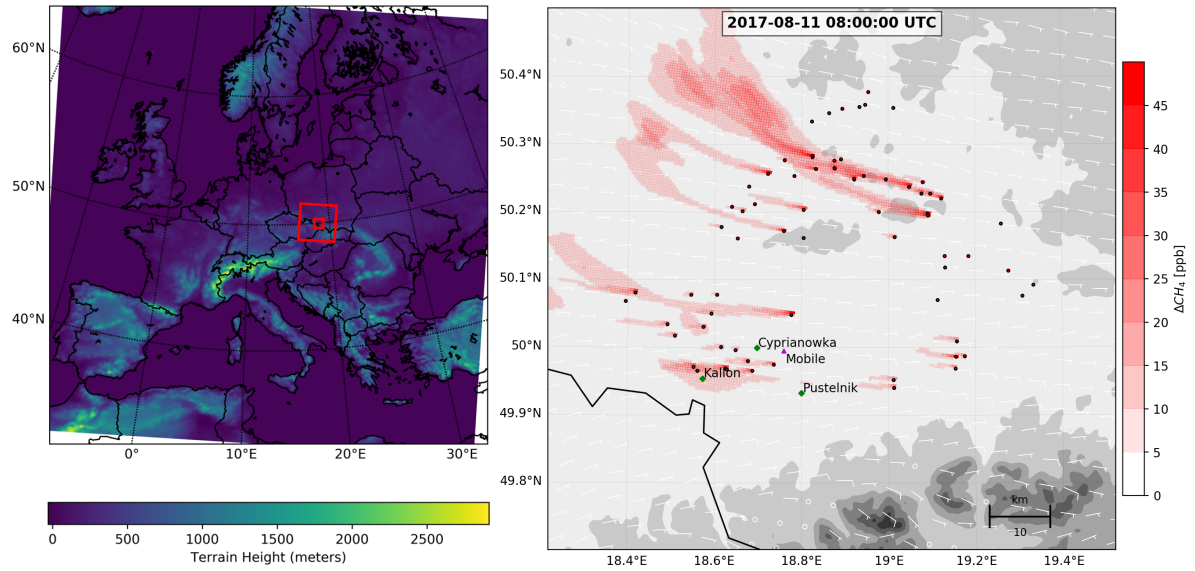

Figure 4.5: The three WRF domains with topographic information on the left panel. The colored part which nearly fills the whole figure marks the first domain with 10 km x 10 km resolution spanning from north Africa to northern Europe and from the coast of Portugal to Russia and Turkey. The bigger red square marks the second domain with 2 km x 2 km spatial resolution. It spans over southern Poland, east Czech Republic and the northern parts of Slovakia. The third domain with 400 m x 400 m resolution basically spans over the USCB including enough space towards the domain boundaries. The right panel is a passive tracer simulation snapshot showing the third domain, all emitting mining shafts as red dots with black edge, the four measurement instruments, deployed during the pre survey CoMet0.5, as green diamonds and purple triangle, and the simulated methane plumes. Grey shading ranging from roughly 300 m a.s.l. (light grey) to over 2000 m a.s.l. (darkest grey), represents terrain height with the Tatra mountain ridge on the southern edge of the domain.

In order to fulfill the CFL condition in every domain, the spatial resolution is reduced stepwise from GFS or ECMWF scales to 10 km × 10 km in the first domain, to 2 km × 2 km in the second domain, and to 400 m × 400 m in the third domain (Fig. 4.5). WRF has the option to automatically select the best fitting time step. Under numerically stable conditions, e.g. low wind shear and small wind direction changes over all domains, the time step is larger than if there is e.g. a lot of convection and high wind shear. The spatial resolution of each domain is one fifth of the overlying domain except for the first nest with 10 km × 10 km which takes over from the overlying global datasets GFS with roughly 28 km or ECMWF with roughly 16 km horizontal resolution.

The WRF passive tracer implementation follows Blaylock et al. (2017) and is described in detail in appendix A. It requires a few changes to the source code with subsequent recompilation. This option allows simulations of the methane plume originating from every shaft. Certain grid cells can act as sources and the air particles in these cells are

marked as 'plume' allowing the user to trace the plume throughout the simulation until it reaches the domain boundary (right panel in Fig. 4.5). It is not possible to account for certain species, so the simulated plumes just represent dry air. Methane depletion or methane buoyancy properties are not considered in this simulation.

From initial tests, it became obvious that the WRF passive tracer output on these small scales with open boundaries has poor mass conservation. This can happen if the result of a numerical calculation suggests a small negative mass for the next calculation step in order to preserve stability. The model then allows different dealing to solve the problem. It can be advised to just neglect negative masses and set them to zero which is called *positive definite* and is the default option. This can lead to a mass gain throughout the simulation. The amount of mass loss is calculated by letting the model simulate a certain amount of time and then sum up all released tracers. Every tracer releases a defined amount of mass at every time step. The sum over the runtime of modeled tracer should be n $\times$ tr with n the number of time steps simulated and tr the initialized amount of tracer released at every time step. This is only valid until the first bit of a tracer is transported out of the domain, which would result in a mass loss. Comparing n $\times$ tr and the actual tracer sum calculated from the model output reveals discrepancies on the order of up to 7% mass gain for the positive definite scheme.

Changing the `tracer_adv_opt` parameter in the WRF `namelist.input` file from positive definite (default) to 5 th-order weighted essentially non-oscillatory (WENO) finite difference scheme (Jiang and Shu, 1996) reduces the mass loss to 1 % to 2 % for the simulated cases. Several simulations were performed with different properties to check the sensitivity of the model to the tracer advection option, including the options *simple*, *positive definite*, *monotonic*, *5th-order WENO*, and *5th-order WENO with positive definite*. Finally, the 5 th-order WENO scheme was chosen as it showed the smallest mass loss. The WENO scheme is not so prone to mass loss as the others and especially as the positive definite schemes. Results of the WRF passive tracer simulations are documented in section 4.4.

4.4 Case study with WRF passive tracer

The emitted methane plumes vary with atmospheric conditions following eddies, and wind speed and direction changes. It is not possible to distinguish between methane emissions from different shafts by just investigating the total column measurements. Knowledge of where the plumes come from and which trajectories these plumes might have followed is important to finally be able to constrain the measured methane enhancements to certain shafts.

Compared to models, which consider the global methane distribution and also take methane depletion into account, the WRF passive tracer approach simulates the methane enhancements based on the E-PRTR emissions. Therefore the observations, which measure the total methane amount in the air column above, need to be separated from the background which is the methane the instrument would measure without coal mine influence.

The right panel in Figure 4.5 displays the simulated methane as it is transported through the USCB on 11 August 2017 at 8 UTC.

With easterly winds, most plumes are traveling westward delivering methane enhancements to the instrument network. The western station Kallon is the downwind station measuring the enhancement and the other three instruments may be used as background. In this particular case, the Pustelnik instrument is used as background station as it measured the lowest methane concentrations and was only little influenced by two upwind shafts in the east. The resulting methane enhancement used for comparisons with the model is the difference between foreground and background XCH_4.

Every WRF tracer represents a mining shaft in the USCB and is scaled with its respective E-PRTR emission value. All WRF grid cells containing tracer information above the location of each stationary instrument are summed up to receive the total column amount of all simulated tracers. As the E-PRTR reports the emissions in $\mathrm{kt\,a^{-1}}$ the simulated measurements are converted into ppm to match the XCH_4 measurements.

The WRF simulations depend on various atmospheric state variables and hence parameterizations. To better understand the model sensitivity of the WRF passive tracer option on atmospheric variability, an ensemble is set up, consisting of ten individual simulations, referred to as ensemble *members*. All WRF V3 passive tracer ensemble members are summarized in Table 4.1. By comparing the different simulation results, one can estimate which properties influence the results most and should be further investigated. Differing results are a measure for a possible error range and help to interpret the results. Although the `CONTROL` run pools the best guess information of all parameters it can suffer from a difference between the input data (e.g. wind information) and real wind conditions. In order to take possible errors into account, four different model runs `NE`, `SE`, `SW`, `NW` simulate the same situation with identical physical properties, except the shafts are displaced for one pixel (400 m) to the respective cardinal direction.

As the boundary layer plays an important role for the transport of the methane plumes, two runs with different boundary layer regimes are simulated. This pertains the dynamics options `diff_opt` controlling turbulence and mixing, and `km_opt` which chooses the eddy coefficient in the WRF `namelist.input` file. Except for the two runs `PBL1` and `PBL2` with altered PBL parameterization, the options `diff_opt` and `km_opt` are both set to 2 for the third (the innermost) domain, which evaluates mixing terms in the physical space (`diff_opt` = 2) and corresponds to a 1.5 order turbulent kinetic energy (TKE) closure (`km_opt` = 2). TKE is the kinetic energy of eddies in a turbulent flow. These are the recommended options for this kind of scale simulations (Skamarock et al., 2008). The WRF ensemble member `PBL1` has a slightly reduced diffusion and turbulence complexity. The parameter `diff_opt` is set to 1 for the third domain which evaluates a second order diffusion term on the coordinate surfaces. It is recommended to use this option together with `km_opt` = 1 which lets the user choose a constant eddy coefficient which is chosen as zero for both, horizontal and vertical diffusion.

Regime `PBL2` simulates the tracer with no turbulence or explicit spatial numerical filters which completely ignores `km_opt` and thus, the eddy coefficient. With this option the tracer propagation only relies on grid cell to grid cell diffusion and ignores turbulent mixing which

Ensemble member	Properties
CONTROL	"best guess"
PBL1	simple diffusion: gradients are taken along coordinate surfaces
PBL2	no diffusion, no turbulence or explicit spatial numerical filters
NE/SE/SW/NW	location of shafts moved 1 pixel (400 m) to north-east, south-east, south-west, north-west
SP_N	location of modeled measurement moved 1 pixel north
CONZ	Emissions increased fivefold
ECMWF	Run with ECMWF data

Table 4.1: WRF ensemble member description. The ensemble represents atmospheric variability with respect to basic meteorological parameters concerning the transport of the simulated tracers.

reduces the overall diffusion significantly.

Similar to the NE/SE/SW/NW options there is also the ensemble member SP_N which moves the location of the physical measurement instrument in the simulations one pixel to the north. This helps to distinguish between single plumes, which are either fully represented in the simulated measurement or which just *scratch* the pixel of interest. The underlying assumption is that position changes of the sources may not have the same effect as position changes of the receiving pixels.

The ensemble member CONZ is the same as the CONTROL run except for quintupled methane emissions, which will give an impression on source strength sensitivity.

The last ensemble member (ECMWF) uses the ECMWF data input for the first domain instead of the GFS input. This is a major change as the whole model uses different boundary conditions. The spatial resolution of the ECMWF data is higher than the GFS data, however in this case, the temporal resolution of the underlying ECMWF data is only 6 hourly data instead of 3 hourly data for the GFS.

Figure 4.6 displays the XCH_4 enhancements measured at location Kallon on 11 August 2017 as black dots. Colored lines represent the simulated measurements of the different ensemble runs. The CONTROL run, the NE/SE/SW/NW runs, and the PBL1 run show similar results with one peak around 8 UTC and a second peak around noon. These runs roughly agree on that features of the modeled emissions. The PBL2 run (orange line), with neglected turbulence as transport mechanism simulates enhanced methane around 10 UTC and 13 UTC when all other ensemble members do not show any methane peaks. It is apparent that turbulence, parameterized as diffusion as the only transport mechanism is not a reasonable parameterization for processes highly influenced by turbulence and so these results are expected to fit the observations the least. The ECMWF run (black line)

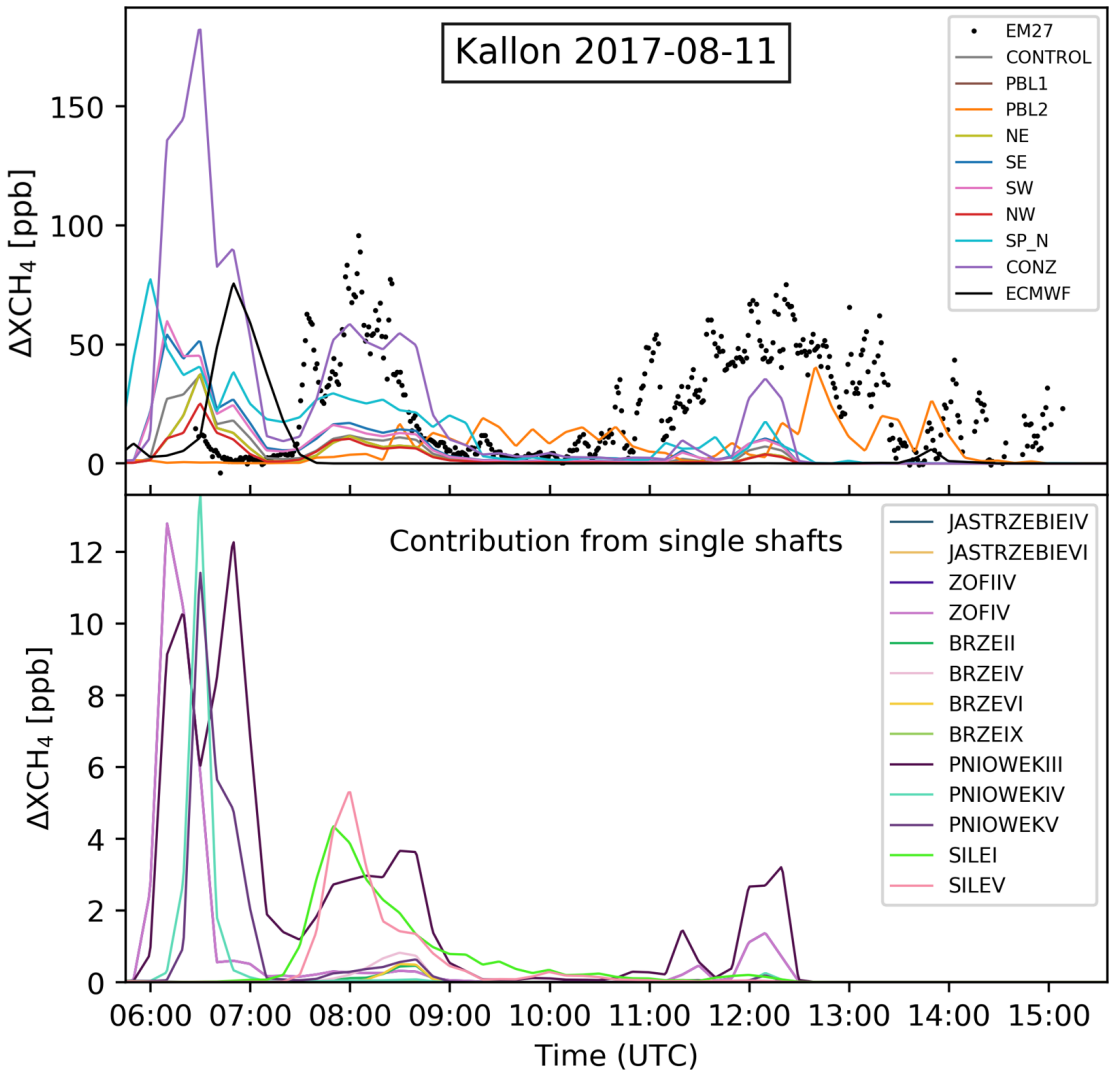

Figure 4.6: WRF ensemble runs compared to the XCH_4 observations (black dots) above and the individual shaft contributions for the `CONTROL` run below. The legend in the bottom panel lists the contributing mining shafts: Jastrzebie IV and VI, Zofiovka IV and V, Brzeszcze II, IV, VI, and IX, Pniowek IV and V, and Silesia I and V. During the morning hours before 7 UTC the model simulates high methane enhancements which might be related to uncertainties in the PBL height. For the rest of the modeled period, the simulated measurements are lower and mainly composed of contributions from the two Silesia shafts and the Pniowek III shaft.

simulates a peak of similar magnitude as the observations but roughly 1 hour earlier than the observed peak. Six hourly wind information seems to be inferior compared to three hourly wind information even if the spatial resolution of the input data is nearly twice as high.

Moving the simulated measurement position one pixel to the north as simulated with the `SP_N` run (cyan line), indicates a general wind direction mismatch of the model and the reality. Moving the station Kallon one pixel to the north significantly influences the simulation results and the magnitude of the enhancement. This indicates, that the plume might have been missed in the simulations and transects slightly north of the station. However, moving the virtual station further to the north does not improve the model. The best match between simulations and observations is achieved by the `CONZ` run with quintupled emissions. The first peak seems to be simulated at nearly the same time and of similar magnitude as the observed peak. The second peak, observed in the afternoon, occurs for somewhat shorter time than the observed peak. All these different ensemble members immediately suggest the need for reasonable wind information. Not only do the modeled wind fields need improvement, but also additional wind measurements can help to validate the model or to use them directly for the emission estimation.

The lower panel in Figure 4.6 adds the information of the origin of each tracer. The contributing shafts for the simulations above are mainly the three Pniowek shafts and the two shafts from the Silesia mine located directly in the east of the Pustelnik instrument.

It has become clear, that knowledge of the wind situation is critical to model the methane field with WRF. The consequences derived from this experience are discussed in the next section.

4.5 Lessons learned

This section addresses four major improvements in different fields of work which are based on the experience gathered during CoMet0.5. The following *lessons* helped to make emission estimation possible on both, facility and regional scale for the actual CoMet mission in 2018.

Technical progress of the mobile FTS

To reach the goal of stop-and-go measurements with an EM27/SUN mounted on a truck, the instrument's sun tracking software emerged as bottle neck. Sufficient for stationary use, the sun tracker speed needs to be improved for mobile applications. Another issue is quick re-pointing towards the sun once the position of the instrument is changed. A fish-eye camera mounted to the instrument quickly sees the rough position of the sun and directs the mirrors towards it. In addition, the measurement process is automatized and can be controlled from inside the observational truck without the need to manually adjust the instrument. As a final result, the possible sampling speed needs to be increased to make stop-and-go measurements possible. From a maximum of three stops during CoMet0.5,

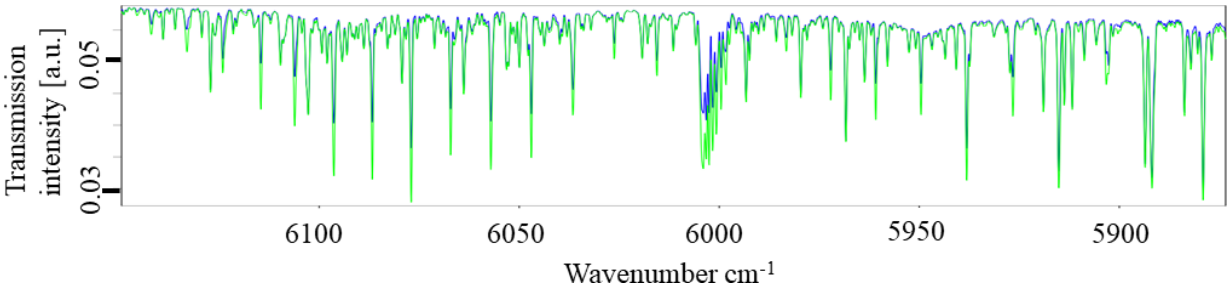

Figure 4.8: Comparison of two spectra recorded on 15 August 2017 on 8:20 UTC (blue) and 8:23 UTC (green). The instrument was located roughly 50 m downwind of a coal mining ventilation shaft (Fig. 4.7). The difference between the green and blue spectrum is caused by a methane eddy getting transported through the instruments line of sight and results in a difference in XCH_4 of roughly 2 ppm. The strong methane absorption is visible with the naked eye.

the team enabled a maximum of over 100 stops for one measurement day during CoMet in 2018. Hard- and software improvements are summarized in section 5.2. The technical developments (Kleinschek et al., 2020) led to a shipborne campaign (Knapp et al., 2021).

Measurement strategy

Measuring close to the mining shafts, i.e. below 1 km distance, comes with a few difficulties: Depending on atmospheric turbulence, the measured CH_4 columns can vary from mid-plume to background level values within minutes or even seconds. During CoMet0.5 the mobile instrument measured on 15 August 2017 in roughly 50 m distance to an active mining shaft (Fig. 4.7) and pointed towards the sun directly in line of sight above the ventilation shaft. The observed spectra would vary from measurement to measurement and let the observer visually see the difference in the absorption features. Figure 4.8 gives an impression on the effect of an eddy transporting high methane air over the instrument around 8:23 UTC (green line), while three minutes earlier at 8:20 UTC the spectrum is indicative of background methane (blue line). The corresponding total column concentrations are 3.825 ppm (green line) and 1.852 ppm (blue line). The wavenumber range on the abscissa matches the spectral retrieval window for methane used in the analysis software PROFFIT (Hase et al., 2004), which is discussed in section 3.3.

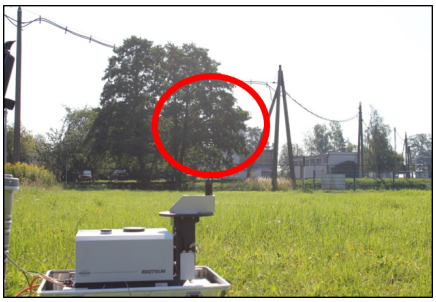

Figure 4.7: EM27/SUN measurement location roughly 50 m downwind of a coal mine ventilation shaft (red circle).

Figure 4.9 summarizes the observations of all four instruments for 15 August 2017, with the high methane concentrations in vicinity to the mining shaft of the mobile instrument in the morning (left panel) and the standard USCB methane variability of all four instruments during the day (right panel). At this time, the mobile spectrometer was moved to another

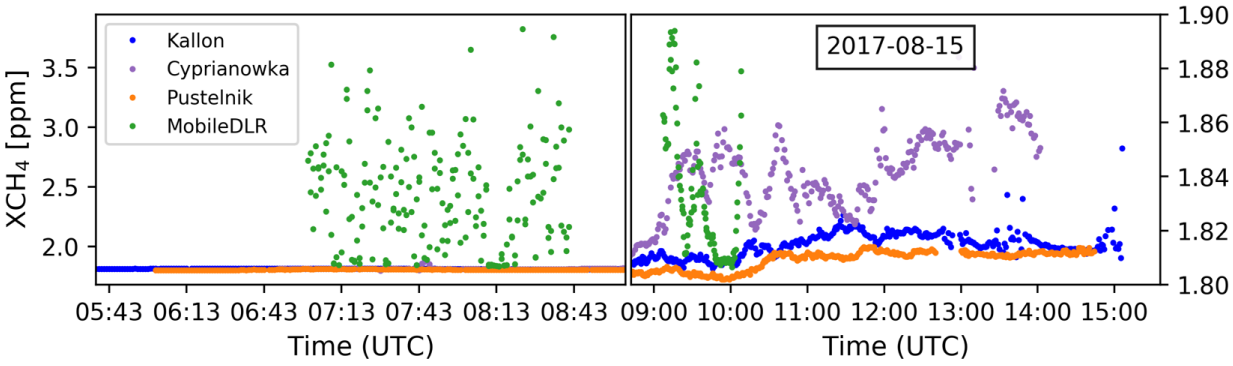

Figure 4.9: XCH_4 measurements of all four deployed instruments. The left panel is dominated by high enhancement signals of the mobile instrument. Moving the instrument away from the plume, shows the typical methane variability observed inside the USCB (right panel).

position in about one kilometer distance to any other methane source. The variability in the right panel illustrates the influence of different shafts or eddies. Unknown wind direction makes it difficult to assign certain enhancements to their underlying origin which had two major implications for the following CoMet mission in 2018: 1) the need for detailed wind information either in form of measurements or models. 2) an in-situ instrument on-board the mobile observatory would be helpful to instantaneously detect methane enhancements and be able to estimate the width of the plume.

The pre-survey also showed, that it is difficult to gain information from measurements taken too close to the shafts ($< 1\,\mathrm{km}$). Background methane measurements with the stationary sensors suffer from influence of different, indistinguishable sources if the instruments are located inside the USCB. This resulted in placing the stationary network during CoMet outside the USCB to be able to estimate a total basin enhancement rather than single facility enhancements. This is an important lesson, as facility scale emissions are estimated with the mobile instrument operating in stop-and-go mode (Chapter 5) and regional emissions are estimated with the stationary network placed around the USCB (Chapter 6), which is hard to realize vice versa.

Wind information

Wind information is crucial when estimating emissions. Wind measurements were not available during CoMet0.5. This makes source attribution difficult and hinders reasonable localization of possible up- or downwind measurement positions and hence background methane identification. During CoMet, in-field wind measurements are enabled by three wind lidars positioned at different locations in the southern part of the USCB. This ensures on the fly wind information for the mobile team and is a key component for the two emission estimation methods discussed in the course of this thesis.

Modeling set up

Turbulent eddies cause the ventilated methane plumes to vary in time and space when measuring close to the shafts ($< 1\,\mathrm{km}$). That applies for stationary as well as mobile instruments. Modeling on such small scales is cost intensive and, in case of e.g. computational fluid dynamics models, requires accurate knowledge of the terrain and objects like trees or buildings and, in the end, instantaneous eddies cannot be reproduced by definition since turbulence is a stochastic phenomenon. These issues are bypassed, by increasing the distance of the stationary instruments to the next mining ventilation facility and encompass the whole USCB with the FTS network, since at greater distances from the sources the multiple larger and smaller eddies have mixed to a large extend producing a composite average plume. The goal is to estimate the emissions of the USCB as a whole or to merge certain groups of shafts to sub-regional emitters which are not so dependent on the variability of single exhaust shafts.

The WRF passive tracer option has two major disadvantages: 1) the dispersion follows the grid of the Eulerian model and is dependent on pixel size. The smallest plume increment is the size of a pixel. 2) the passive tracer option shows poor mass conservation. Both issues are addressed by introducing the Lagrangian dispersion model FLEXPART (Section 3.5) which is driven by WRF wind information.

Chapter 5

Emission estimation on facility scale

The mobile FTS observatory and the cross-sectional flux method form the basis to estimate the emissions from coal mine ventilation shafts on facility scale. A facility in the sense of this work generally consists of one shaft or a small group of shafts. However in one discussed case, the number of possible contributing point sources cannot be determined exactly. This chapter has been published in Luther et al. (2019).

5.1 Campaign deployment

The deployment region, the USCB, is pictured in Figure 5.1. It shows the general location of all known coal mine ventilation shafts (gray triangles), the stationary EM27/SUN positions (red triangles), the wind lidars (red stars), and the colored tracks of the five mobile observatory transects discussed here. The USCB coal mining area groups into a northern part in the vicinity of the city of Katowice and a southern part close to the borders of the Czech Republic and Slovakia (beyond the Tatra mountains). The shafts in the south are not as densely located as in the northern part, which helps to attribute the plumes to the sources and avoids mixing of different sources for most wind directions. Additionally, the E-PRTR inventory lists the largest emitters in the southern part, hence, the mobile FTS operations are restricted to this part of the USCB. Due to mainly easterly winds throughout the campaign deployment period, the south-eastern part of the USCB is in particular favored as the methane concentration upwind of the shafts is expected to be not influenced by coal mining activities, leading to a clear distinction between background methane and enhancements. The mobile observatory's base was located together with the southern stationary FTS and the southern wind lidar (DLR89). The driving time to reach the target facilities varied between 20 min and 40 min.

In addition to the mobile FTS, a network of four stationary FTS is deployed, with the aim to estimate regional emissions (see Chapter 6). Furthermore, other groups were

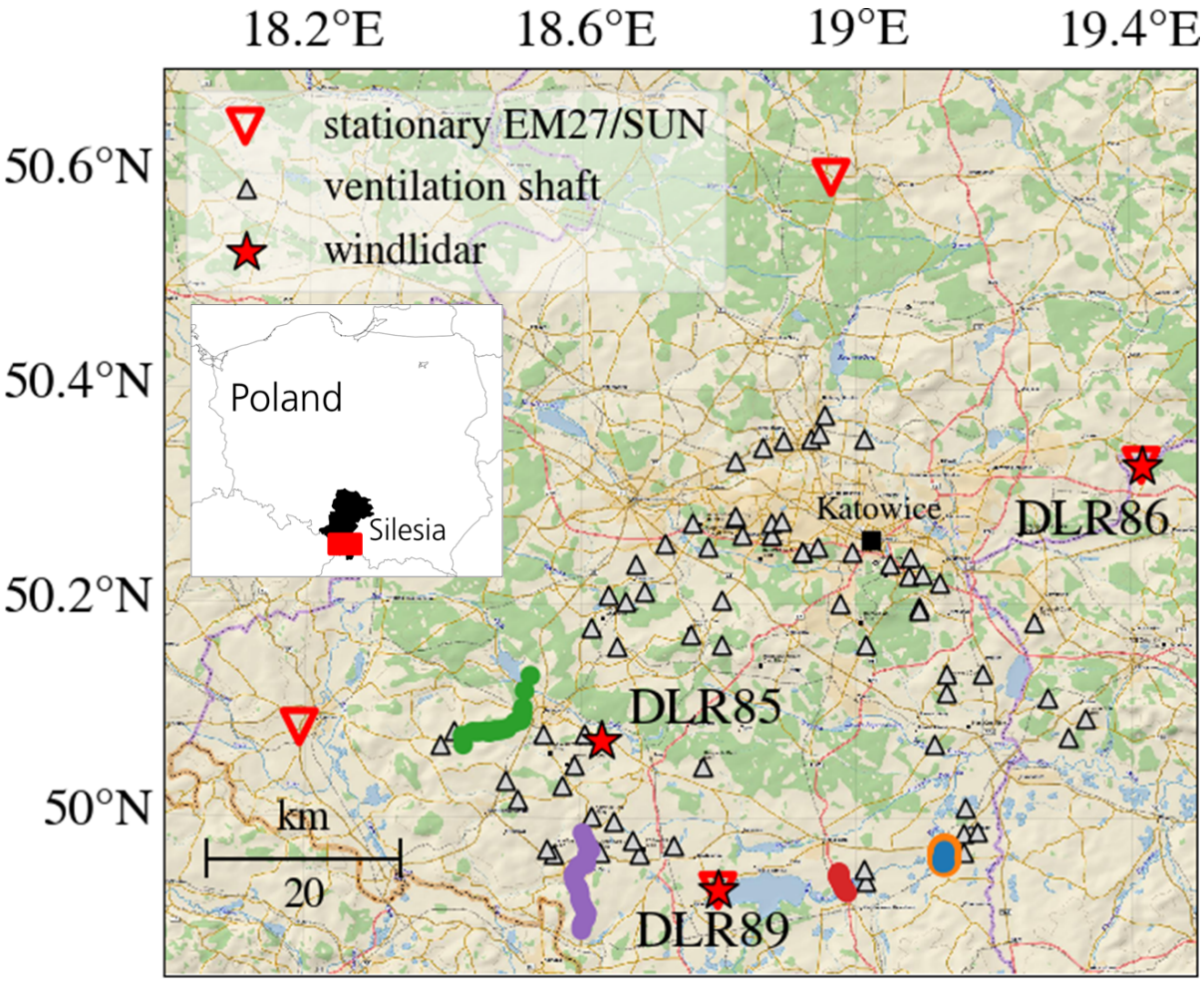

Figure 5.1: Map of the USCB in southern Poland (see small inset on the left with the black outline of the region of Silesia and red depicting the map excerpt of the USCB). Ventilation shafts are displayed as gray triangles. Colored dots depict five plume transects measured with the mobile FTS on 24 May at around 7-8 am (orange), on 24 May around noon (blue), on 1 June (green), on 6 June during morning hours (red), and on 6 June around noon (purple). The most active CH_4 emitters are assumed to be located in the southern part of the USCB, which is why mobile FTS measurements are focused on this area. Stationary EM27/SUN locations are marked as red triangles; the three wind lidars DLR85, DLR86, and DLR89 are marked as red stars. Eastern and southern wind lidars are placed at the same locations as the respective EM27/SUNs. Background map from ESRI (2019). Figure adapted from Luther et al. (2019)

involved in the CoMet measurement campaign: in-situ sensors deployed in cars by different groups from the AGH University of Krakow, the University of Heidelberg, and the University of Utrecht, sampled across and around the region. Aircraft supported in-situ (Kostinek et al., 2019; Fiehn et al., 2020) and remote sensing instruments (Gerilowski et al., 2011; Krautwurst et al., 2021) were operated out of Katowice airport. The *High Altitude and Long Range Research Aircraft* 'HALO', carrying – among others – CHARM-F, the airborne demonstrator for MERLIN, an upcoming, methane measuring space lidar (Amediek et al., 2017) visited the USCB operating out of the special-airport at Oberpfaffenhofen close to Munich, Germany.

The FTS activities are carried out from 22 May 2018 until 12 June 2018. The mobile FTS measurements (section 5.2) and the wind lidar data (section 5.3) are combined with the cross-sectional flux method (section 5.4) to estimate coal mine CH_4 emissions presented in section 5.5 together with the error analysis in section 5.6.

5.2 Mobile FTS observatory

In order to conduct mobile measurements with the standard EM27/SUN, some modifications are implemented (Klappenbach et al., 2015; Butz et al., 2017; Kleinschek et al., 2020; Knapp et al., 2021). Considering a preferably short period of stay at every measurement position to increase the amount of stops and therefore the number of possible plume sampling points, the whole sun-tracking mechanism is accelerated. The software and hardware components needed for this task are designed by Kleinschek et al. (2020) and explained in the following. Two main delaying factors are noticed with the standard setup: 1) at each start up (i.e. each stop) the standard instrument needs to be aligned manually in roughly southern direction and the projected sun disc needs to be tracked with the build in camera via fine tuning inside the CamTracker software. Once the sun disc is detected the tracking is stable and does not require further manual interference except for tracking interruptions by e.g. clouds (Klappenbach et al., 2015). 2) the servo motor drivers of the two axes setup, steering the mirrors are quite slow. Delaying factor 1) is addressed by installing a fish-eye camera on top of the spectrometer housing and adding a two-stage tracking control mechanism. In the first stage of sun-tracking, the upward looking fish-eye camera detects the relative position of the Sun in the hemisphere and the software steers the mirrors to coarsely point into the Sun's direction. In the second stage, the fine tracking system developed by Gisi et al. (2011) takes over to follow the Sun's relative position. Fine tracking errors amount to roughly 10 arc s with an overall accuracy of 0.05°. The second delaying factor 2) is addressed by simply speeding up the servo motor movement. The response time of the system is with 10 Hz sufficiently fast.

Fig. 5.2 depicts the mobile EM27/SUN mounted on the measurement truck. The system, including the instrument, the control PC, and the measurement notebook inside the truck, is powered by a 12 V car battery, also mounted on the bed. The system is steered from inside the truck and the operators can stay inside the car, except for opening and closing the cover. A suspension plate with rubber bearings protects the instrument from

dull impacts caused by e.g. bumpy roads.

Inspired by Butz et al. (2017), the custom-built solar tracker enables efficient stop-and-go patterns. The system supports start-up and repointing to the Sun within a few seconds once the solar-tracking is interrupted. During the sun-tracking test phase, the instrument was mounted to a car and spectra were recorded while driving. However, high frequency mechanical disturbances caused by small road irregularities and the car's suspension were not compensated. This restricts the use for this particular system to stop-and-go measurements. The standard measurement procedure consists of ten double-sided interferograms per stop which results in typical dwell times of 2 min 30 s per stop. An increased sampling rate to 40 kHz, as demonstrated for the days from June 06 on, resulted in average dwell times of 60 s.

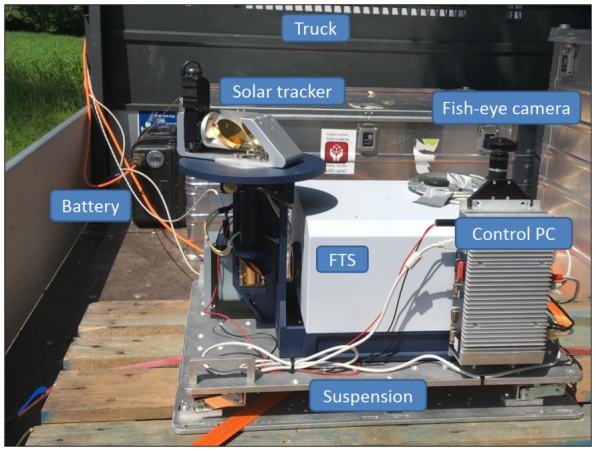

Figure 5.2: Mobile FTS (EM27/SUN) mounted on a truck.

In general, ten spectra per stop are recorded and the retrieved XCH_4 values are averaged for every stop location. For all measurements recorded at every stop, the standard deviations range from 0.12 % (roughly 2 ppb) on 6 June, when most observations were taken far (>40 km, stops every 500 m) from any source to 0.26 % (roughly 4 ppb) on 24 May, when the plume is sampled within 2 km of the source, stopping approximately every 70 m. The stop-wise standard deviations serve as metric for the measurement error that propagates into the emission estimates. Regarding the fact, that parts of the standard deviations may also be caused by atmospheric variability as air masses or eddies with different methane content may have passed the line of sight of the mobile instrument, the choice of these standard deviations for the error propagation of the mobile approach is conservative. For the stationary FTS network, a noise signal of 0.6 ppb is evaluated as the standard deviation of the averaged background measurements of two stationary instruments (The Glade and Za Miastem) from 7 UTC to 10 UTC on 28 May 2018 (see right panel in Fig. 6.9).

The methane plumes emitted from the ventilation shafts are not visible and odorless, and the FTS methane analysis as discussed here does not deliver real-time results. In order to find the plumes, the operators of the mobile instrument have to look through weather and wind direction forecasts and then guess the rough direction of the plume by reference to the shaft locations. In the field, the observed shafts are mostly not visible since they are too far away and thus, the rough plume location and extend need to be assumed by means of maps and actual wind direction measurements. This procedure contains many weak spots and it is likely that the plume is missed or sampled incompletely. Time is a crucial factor when measuring with mobile instruments, because the atmospheric state should be as stable as possible for the transects and the plume needs to be entirely crossed to record

background methane signals before and after crossing the plume. For that reason, two different in-situ instruments are installed in the truck sucking in ambient air and quickly analyzing the results with near real time atmospheric methane content information. Two different instruments are used for practical reasons, as only instruments could be used which were not occupied by other campaign teams. From 6 June on, first, a Picarro CRDS (Cavity Ring-Down Spectroscopy) analyzer was installed measuring in-situ CO, CO_2, CH_4, H_2O. The instrument is powered by big, and heavy battery packs occupying a lot of space inside the measurement truck. After four days, the Picarro instrument is exchanged for a Los Gatos Research Ultraportable Greenhouse Gas Analyzer. This instrument is smaller than the Picarro and can be powered via the 12 V cigarette lighter adapter in the car. No deeper or scientific comparison between these two instruments is provided here, as the only purpose for these instruments was to help the mobile operators find the plume. Therefore, the precision and accuracy of these instruments is not important, as long as a significant methane enhancement can be detected and temporally assigned with a plume. However, the data still was recorded and might be used for other research questions. The in-situ instruments improved the ability to quickly track down single plumes and increased the overall measurement efficiency.

5.3 Wind measurements during CoMet

Throughout this thesis, wind information plays an important role. The movement and the structure of the methane plumes is dependent on the wind direction and the wind speed, since every emission estimation method needs at least basic wind information. This work basically covers two different spatial scales - facility scale and regional scale. This is, in a similar way, also valid for the used wind information: for the estimation of the facility scale emissions, wind measurements of three Leosphere Windcube 200S Doppler wind lidars (Vasiljević et al., 2016; Wildmann et al., 2018) are used directly for the emission estimates. For the regional scale, wind measurements from the lidars are assimilated into the WRF model as explained in section 6.2.

As part of the CoMet measurement campaign the three instruments were distributed to the east, south, and mid-west of the USCB (Fig. 5.1). The exact locations are listed in Tab. 5.1.

Instr.	Site	Lat. (°N)	Lon. (°E)	m a.s.l
DLR85	Rybnik (W)	50.0725	18.6298	253
DLR86	The Glade (E)	50.3292	19.4155	303
DLR89	Pustelnik (S)	49.9326	18.7998	266

Table 5.1: Locations of wind lidars deployed during CoMet. The second column lists the site names with their respective cardinal directions relative to the USCB in brackets. (adapted from Luther et al. (2019)).

Although the USCB locates in a plain, flanked by the Tatra mountains in the south and a lower ridge of hills to the east, to some extent, the land surface and vegetation varies across the region. In the west of the USCB, DLR85 is deployed next to a private airfield, mostly used for parachuting activities and flight training schools. The land is flat towards south-westerly directions. However, the airfield is located close to a forest in the north-west of the wind-lidar. *The Glade* (DLR86) is placed roughly 60 km to the north-east from DLR85. The instrument operates in a dip in an otherwise forested area. The southern instrument DLR89 at station Pustelnik, is deployed in the vicinity of the barrier lake Goczalkowickie. The linear distance between the instrument and the bank is roughly 500 m. The lake is likely influencing the wind profiles measured at this station. The flat surface of the lake has a lower surface roughness as the forests close to the other instruments. This is likely causing the PBL being lower at this station, as the influence of the surface on the wind profile vanishes already at lower levels.

The Doppler wind lidars perform velocity azimuth display (VAD) scans continuously, as programmed for this particular purpose. Vertical profiles of wind and turbulence are retrieved, which requires two different elevation angles of the VAD scans. The general measurement procedure comprises 24 VAD scans with an elevation angle of 75°, followed by six scans with an elevation angle of 35.3°. Mean wind speed and direction profiles are retrieved from the 75° scans with a small cone angle, covering at least the whole PBL. According to Smalikho (2003), wind speed and wind direction are calculated from filtered sine-wave fitting (FSWF) of the line-of-sight velocities. The 75°-scans are also used to retrieve turbulent kinetic energy dissipation rate. The 35.3° elevation angle is necessary to derive turbulent kinetic energy (TKE), integral length scale and momentum fluxes according to Smalikho and Banakh (2017). The turbulent kinetic energy dissipation rate is of special interest for this work, as it is a measure for the PBL height (Stephan et al., 2018b). We assume that the relevant coal mine methane emissions are not significantly mixed out of the PBL. This confines the wind information discussion to levels up to the PBL height but not above.

In general, turbulent eddies (associated with vortex twisting and stretching) cause turbulent energy to flow toward the smallest scales (Holton, 1973). TKE production is dominated by large eddies with length scales of 100 m and more, which gradually decay into smaller and smaller eddies until the length scales are small enough, that the energy is dissipated into heat by viscous diffusion on the millimeter scale (Holton, 1973; O'Connor et al., 2010). The dissipation rate (referred to as eddy dissipation rate or EDR), can be used as turbulence intensity indicator (Yang et al., 2020). High values indicate the presence of strong turbulence and vice versa. Smalikho (2003) describes one approach to retrieve EDR from lidar observations. In the free atmosphere directly above the PBL, only weak turbulence is expected leading to eddy dissipation rates, which are generally a few orders of magnitude smaller than inside the PBL where e.g. strong convection can occur. Stephan et al. (2018b) describes, how the PBL height can be estimated through detection of the height at which the EDR drops below $10^{-4}\,\mathrm{m^2 s^{-3}}$. Calculated PBL heights are depicted in Fig. 5.3. The signal-to-noise ratio of line-of-sight velocity measurements determines the uncertainty of the wind speed retrievals with the FSWF-method (Stephan et al., 2018a).

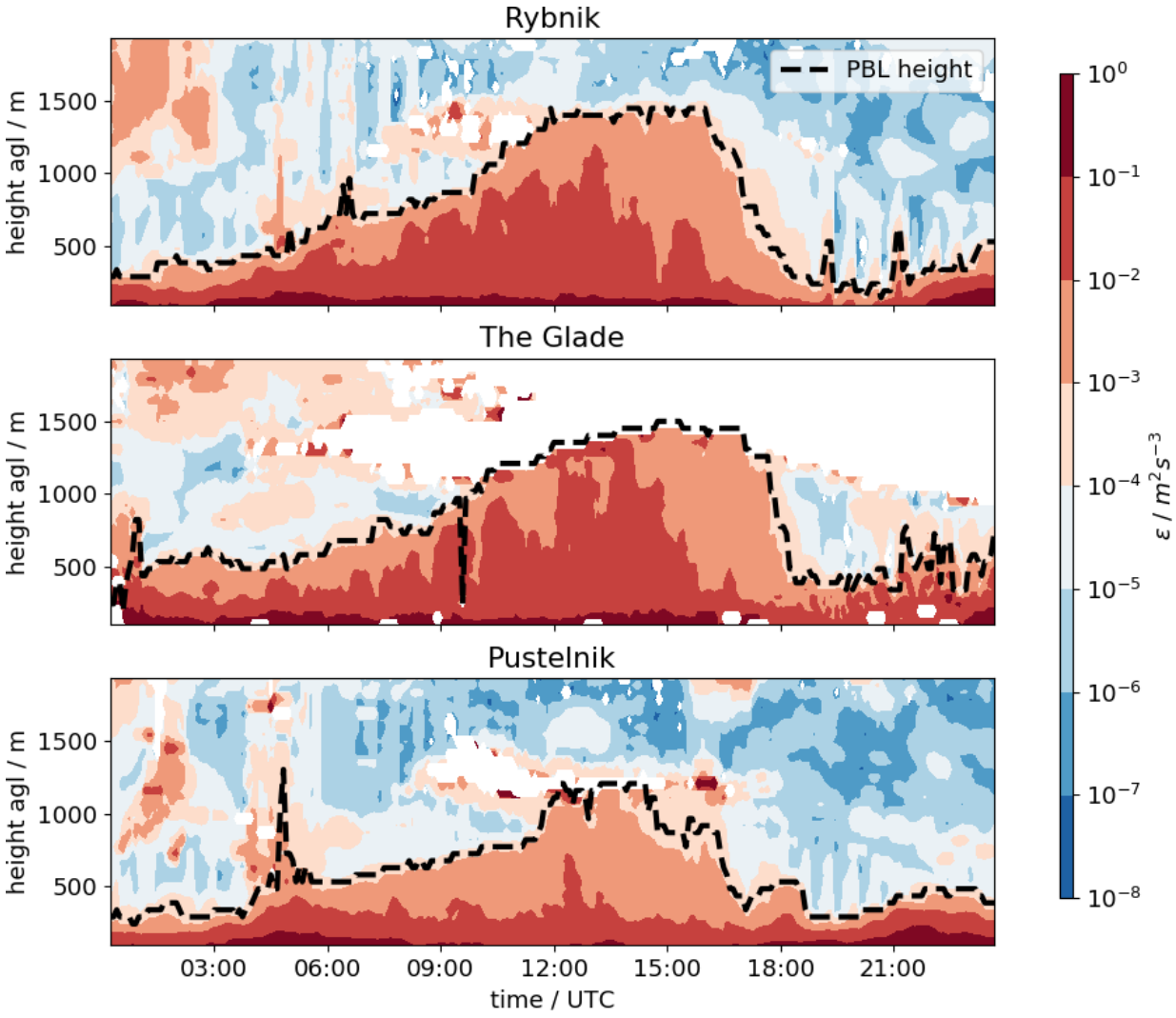

Figure 5.3: Wind lidar profiles of eddy dissipation rate (EDR) on 6 June at the three locations Rybnik/DLR85 (top), The Glade/DLR86 (middle), Pustelnik/DLR89 (bottom). Dashed black lines represent the respective PBL heights. EDR greater than $10^{-4}\,\mathrm{m^2 s^{-3}}$ corresponds to PBL values. Note, that the PBL height at station Pustelnik/DLR89 is lower compared to the other two stations. This is a general feature, observed throughout the measurement campaign which could be related to a nearby lake with generally lower surface roughness (adapted from Luther et al. (2019)).

Further, an uncertainty of 0.2 $\mathrm{m\,s^{-1}}$ is considered, which is particularly striking under low wind speed conditions.

Fig. 5.3 depicts the Doppler wind lidar 75°-scans of all three instruments for the generally cloudless day, 6 June 2018. Similar to the schematic drawing of a standardized PBL in the right panel in Fig. 2.1 in Chapter 2, the EDR scans show a distinct PBL structure as it is associated with a mid-latitude, convective summer situation. The daily PBL cycle from left to right in Fig. 5.3 is generally similar for all three stations. During the night and early morning hours, the PBL is generally below 500 m a.g.l.. With sunrise and slowly starting convection the PBL hight increases until it sharply drops around sunset. During the afternoon, at some parts of the sky, smaller cumulus congestus clouds are observed connected to the ongoing convection. The influence of the aforementioned flat lake surface may have led to a generally lower PBL height at the southern station Pustelnik (bottom panel in Fig. 5.3). PBL height measurements of such detail are very useful for emission estimation analyses and an overall understanding of the ongoing atmospheric processes relevant for the layers important for plume dispersion. The PBL heights measured by the EDR scans are the reference for all mentioned PBL averages of wind speed and direction throughout this thesis. Measured PBL height and wind profile information greatly improves the discussed emission estimation methods.

5.4 Cross-sectional flux method

The mobile FTS observatory mounted on a truck is specialized to drive through point source emission plumes with the aim to sample the background before and after crossing the plume as well as the plume enhancements (see Fig. 5.4). These CH_4 measurements together with the wind information from the wind lidars are fed into the cross-sectional flux method outlined by Varon et al. (2018) to estimate the instantaneous emissions. The cross-sectional flux method is typically combined with airborne in-situ measurements (White et al., 1976; Mays et al., 2009; Cambaliza et al., 2014, 2015; Conley et al., 2016). Another application possibility is airborne CH_4 (partial) column measurements (Krings et al., 2011, 2013; Tratt et al., 2011, 2014; Amediek et al., 2017). The method is based on the mass balance assumption, assuming, that the emitted amount of the target substance is the difference between what is present downwind of the source and the amount which was present upwind of the source. This is realized by integrating the product of CH_4 concentration enhancements and wind speed along a plume cross-section. In our case, the cross sections are sampled by stop-and-go of the measurement truck. The sampling process is not continuous and relies on the amount of stops for the transect duration. Therefore, the integral is approximated by a sum over all cross-plume measurements i. This leads to the source strength Q in units $[\mathrm{kg\,s^{-1}}]$

$$Q = \sum_i \Delta\Omega(x_i, y_i)\, U_{\mathrm{eff}}(x_i, y_i)\, \Delta y_i \tag{5.1}$$

with the horizontal coordinates x_i and y_i along and across the plume's direction, respec-

tively. The methane enhancements ΔXCH_4 [ppm], calculated from the difference between inside- and outside-plume measurements, yields the plume enhancement $\Delta\Omega$ [kg m^{-2}] by

$$\Delta\Omega = \Delta XCH_4 \frac{[O_2]}{0.20942\,N_a}\,10^3\,M_{CH_4} \tag{5.2}$$

with the molar mass, M_{CH_4}, the total column O_2 measurement, $[O_2]$, and the Avogadro constant N_a. The effective wind speed $U_{eff}(x_i, y_i)$ represents the plume dispersion. The cross-plume segment Δy_i represents the distance between two stops, valid for the $\Delta\Omega(x_i, y_i)$ enhancement. The measurements i denote individual stops of the stop-and-go patterns i.e., quantities are averaged over individual stops. Wind speed and wind direction are estimated by distance-weighted averages of all three wind lidar profiles, which are interpolated to the time of observation. Averaging the vertical profiles of wind speed (wind direction) over the PBL gives U_{eff} (x_i, y_i) in Eq. (5.1).

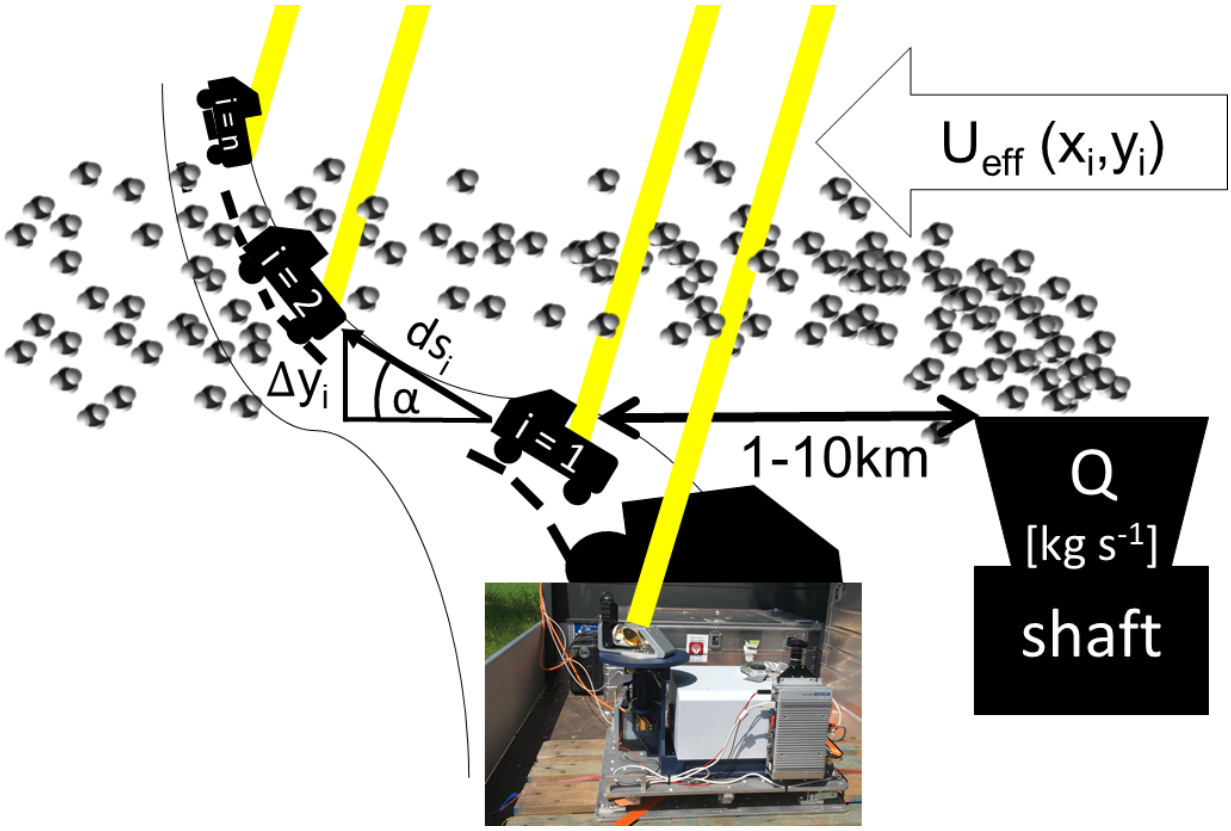

Figure 5.4: Schematic measurement pattern of the cross-sectional flux method as introduced in Equ. 5.1. Methane emissions from a coal mine ventilation shaft with the source strength Q are transported by the wind $U_{eff}(x_i, y_i)$. The mobile FTS stop-and-go measures the direct sunlight absorption spectra before, during, and after crossing the plume at n locations i.

Several caveats and sources of error arise with this method. (1) The measurement

vehicle is bound to public roads, which are generally not perpendicular to the direction of the plume's propagation. Therefore, the cross-plume segment Δy_i is defined as

$$\Delta y_i = ds_i \sin(\alpha_i) \tag{5.3}$$

where ds_i denotes the driven distance between two consecutive stops of the stop-and-go pattern and α_i is the relative angle between the driving direction and the PBL-averaged wind direction. (2) A well-defined XCH_4 background removal is key to reliably calculate ΔXCH_4. This leads to operational requirements to sample background air on both sides of the plume. (3) The method requires a generally constant wind direction over the sampling duration of typically 1 to 1.5 hours. (4) U_{eff} must be accurate and representative for the observed plume enhancement ΔXCH_4. From Equ. 5.2 it is evident that relative errors in effective wind speed equal relative errors in estimated emissions. This is particularly striking under low wind speed conditions, where relative errors in the wind speed measurements become large. These caveats are discussed with the data and errors in sections 5.5 and 5.6.

5.5 Mobile FTS based emission estimation

Five transects will be discussed in the following, depicted in Figures 5.5 to 5.9: one morning and one noon transect on 24 May, one transect on 1 June, and again one morning and one noon transect on 6 June covering different mines and facilities in the USCB. Left hand side panels illustrate the locations of the mobile observatory relative to the nearest mining ventilation shafts with additional color coded XCH_4 defined through Equ. 3.9. Wind speed and direction are symbolized by small wind barbs. For 1 June, the wind speed was particularly low (below 5 kn i.e., always below 2.5 ms^{-1}) and therefore wind barbs are not displayed. However, the wind lidars' weighted and PBL averaged direction measurements reveal a general south-easterly wind direction. The panels on the right-hand side depict the timeline of all measurements of the mobile EM27/SUN as gray dots together with their respective local stop-wise averages as black crosses. In order to calculate reasonable methane enhancements, there is the need to also measure the background methane, which is the methane column free of the influence of nearby coal mine related sources. When measuring inside the USCB, a contamination of the measured plume with methane emitted by different upwind sources is very likely. However, if the distance to the disturbing upwind shafts is large enough, the methane will be dispersed inside the PBL once it reaches the location of interest. Then the FTS will measure a rather constant, but compared to outer-USCB values, higher total methane column as background. Once the instrument is set up in a way, that the background methane can be clearly distinguished from methane plumes on either side of the plumes, it is possible to use the cross-sectional flux method to estimate the emissions.

The background XCH_4 total column values (dashed black lines in right panels in Figures 5.5 to 5.9) are linear least squares-fitted (in time) between the measurements before and after the plume transect. This balances possible influences of upwind shafts on one of the

sides of the plume. All cases are selected for which (1) a clear background signal before and after crossing the plume can be determined, (2) the wind direction measured by the wind lidars is roughly constant, and (3) the overall transect duration does not exceed the maximum of 1.5 hours. This section lists details (summarized in Table 5.2) about all transects and their best-estimate emissions calculated with the baseline wind scenario. For the discussion of the error analysis see section 5.6.

24 May 2018 morning transect

In the morning of 24 May (Fig. 5.5), the stop-and-go patterns are conducted about 2 km west of a ventilation shaft, with stops roughly every 100 m. The target shaft is the most southern shaft of the Brzeszcze mine, which is connected with four shafts in total. With the next closest ventilation shaft located about 2 km to the north, no other known shafts were located upwind. Plume enhancements ΔXCH_4 are measured with up to 15 ppb with a maximum around 7 am. The best-estimate emissions Q (calculated according to Equ. 5.1) amount to 6 ± 1 kt/a.

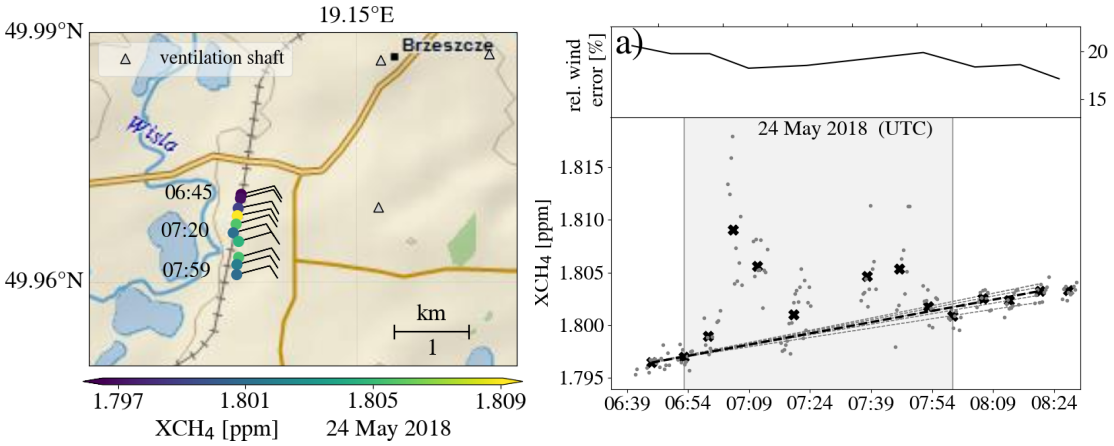

Figure 5.5: XCH_4 measured on 24 May 2018 downwind of a coal mine ventilation shaft in the USCB. The left panel displays the driven path and the locations of each observation. Wind barbs indicate the wind direction. The right hand panel displays measured XCH_4 as gray dots and respective local stop-wise averages as black crosses. The best-estimate background XCH_4 is indicated as dashed black line. Gray areas represent the measurments identified as intra-plume. The black line on top of the right hand side panel displays the combined, relative wind error for each measurement calculated as the square root of the averaged variances of both, the mean PBL wind speed and wind direction. Dashed gray lines in panel a) illustrate all background options contributing to the background related error. Geographic map from ESRI (2019). Figure adapted from Luther et al. (2019).

24 May 2018 noon transect

Fig. 5.6 displays the observations of the same ventilation shaft but now driving the stop-and-go patterns in the other direction from south to north. Due to technical issues, the transect was interrupted for nearly half an hour from 11:15 to 11:41 UTC. We made the unsuccessful attempt to launch low-cost wind sondes. Maximum enhancements ΔXCH_4 reached roughly 30 ppb around 11:45 am. The emissions are estimated with $Q = 10 \pm 1$ kt/a, which is nearly 70 % higher than for the morning transect. This may have different possible reasons: As visible in panel b) in Fig. 5.6, the background CH_4 exhibits a south to north gradient. This indicates possible methane inflow from unknown sources further upwind. The wind lidars also measured a low-level jet during the morning hours which also might have influenced the morning transect. Other, likely explanations for the difference are atmospheric and mining processing variability. During the morning hours, the still shallow PBL is dominated by turbulence which causes the PBL to rise. Single methane blobs may have influenced the measurements. In addition, the mining process is not constant and can lead to spontaneous emission increases. Throughout the observations of 24 May, the XCH_4 background south of the plume is generally 4 to 5 ppb higher compared to the north.

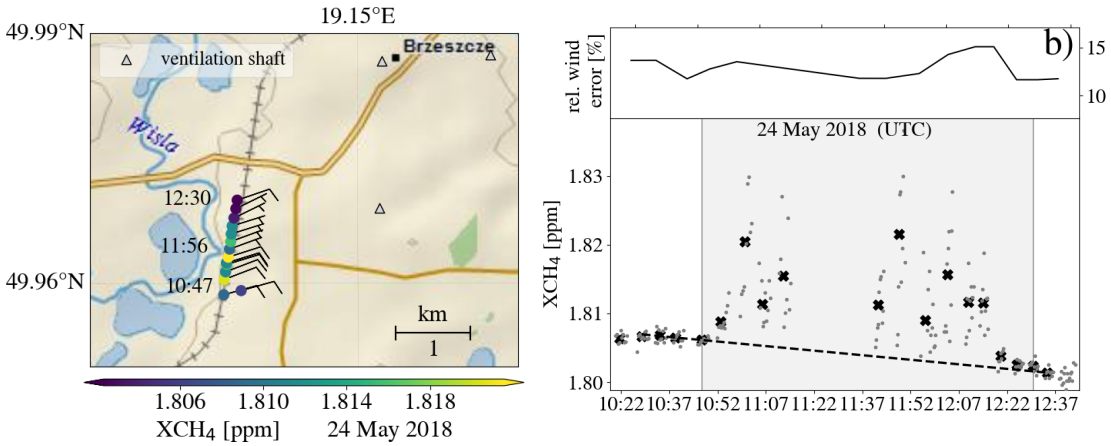

Figure 5.6: XCH_4 measured on noon of 24 May 2018. See caption Fig. 5.5 for detailed explanation. Geographic map from ESRI (2019). Figure adapted from Luther et al. (2019).

1 June 2018

1 June is depicted in Fig. 5.7). On this day the observational team aimed for the western border of the USCB (green dots in Fig. 5.1). Particularly low wind speeds ($<2.5\,ms^{-1}$) are observed from the nearby wind lidar DLR85 (11 km distance to the observations). A group of several upwind shafts deteriorates the source attribution to individual ventilation shafts and influences the background measurements. But since the methane observations on

either side of the plume are nearly the same, the background is considered as homogeneous. ΔXCH_4 values peak at about 60 ppb around 9:30 UTC just before the end of the 1.5 h north to south transect. The distance of our observatory to the closest mining shaft was never less than 4 km. The CH_4 emission for this particular group of shafts is estimated with 109 ± 33 kt/a.

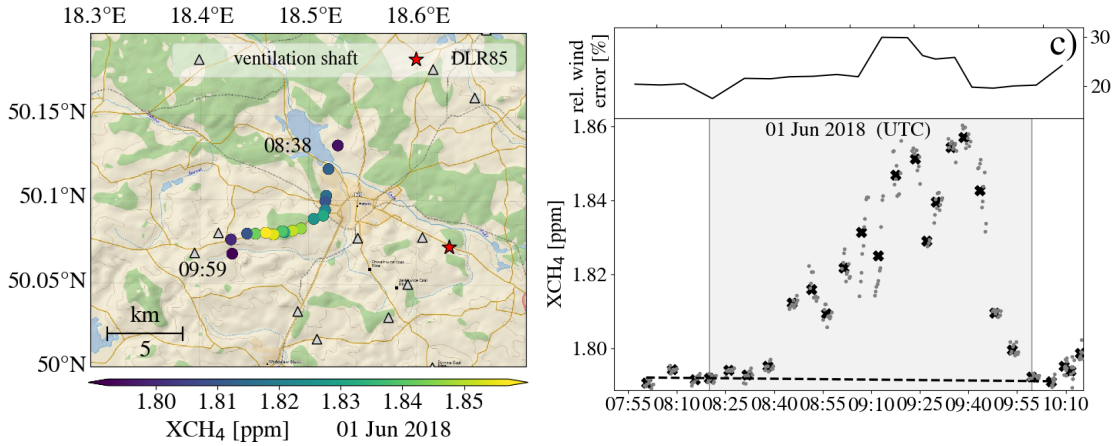

Figure 5.7: XCH_4 measured on noon of 1 June 2018. Note, that the wind speed was very low ($<2.5\,ms^{-1}$) and the wind barbs are not resolved. However, the general wind direction was south-east. See caption Fig. 5.5 for detailed explanation. Geographic map from ESRI (2019). Figure adapted from Luther et al. (2019).

6 June 2018 morning transect

Clear sky conditions on the 6 June 2018 enabled the mobile observatory to observe two targets on one day. During the morning hours around 7 am UTC, the observations begin with the Silesia mine located east of Pustelnik with two shafts at the south-east border of the USCB (red dots in Fig. 5.1). Under east-northeast wind conditions, the plume is sampled 1 to 2 km west of the shafts (Fig. 5.8). With the in-situ methane analyzer on board, the rough position of the plume is assessed on the fly while moving the truck. Once background CH_4 levels are perceived in the south, the FTS started sampling while stop-and-go moving northward with an average step size of 100 m. Maximum enhancements ΔXCH_4 with roughly 35 ppb are observed around 7:30 am. Emissions Q are estimated with 17 ± 3 kt/a. The difference between southern and northern background amounts to roughly +4 ppb.

6 June 2018 noon transect

The noon transect on 6 June (purple dots in Fig. 5.1 and depicted in Fig. 5.9) is influenced by winds of north-easterly direction. The distance between the individual sampling stops is roughly 500 m, resulting in a total distance of more than 10 km. With the goal to measure

a cross section through the southern part of the USCB, the observational truck moved from south to north, looking for the background methane recorded by the in-situ instrument on board. About 1 to 2 km downwind of a group of four shafts close to the planned track, XCH_4 enhancements exceeding 30 ppb are measured. The total emissions Q for this part of the USCB are calculated as 81 ± 13 kt/a.

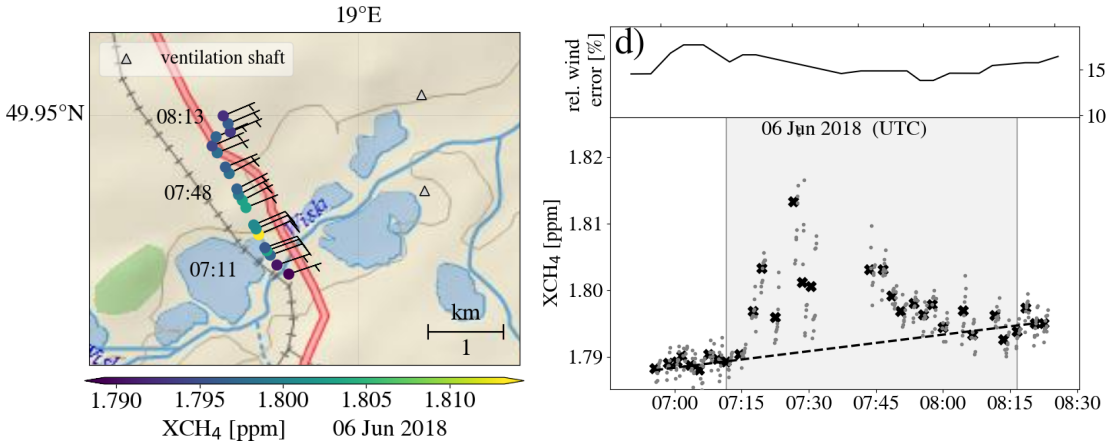

Figure 5.8: XCH_4 measured on 6 June 2018 during the morning hours. See caption Fig. 5.5 for detailed explanation. Geographic map from ESRI (2019). Figure adapted from Luther et al. (2019).

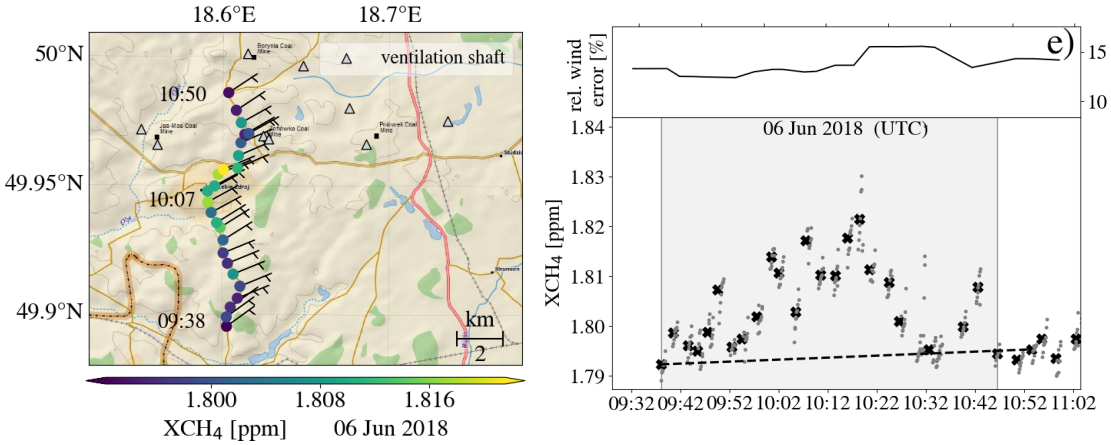

Figure 5.9: XCH_4 measured on noon of 6 June 2018. See caption Fig. 5.5 for detailed explanation. Geographic map from ESRI (2019). Figure adapted from Luther et al. (2019).

Date and time	Estimated emissions ($kt\,a^{-1}$)	Comb. σ ($kt\,a^{-1}$)	Comb. σ %	E-PRTR 2014 ($kt\,a^{-1}$)	Relative standard deviation (1σ) due to averaging of: FTS obs. [ppb] XCH_4	FTS obs. [ppb] backgr.	wind speed (U_{eff}) [%] vert.	wind speed (U_{eff}) [%] horz.	wind speed (U_{eff}) [%] time	wind dir (Δy_i) [%] vert.	wind dir (Δy_i) [%] horz.	wind dir (Δy_i) [%] time
24 May 7 to 8 am	**6**	**1**	19	**9.63**	2	0.2	13	10	8	2	3	2
24 May noon	**10**	**1**	15	**9.63**	4	0.3	8	10	3	5	3	3
01 June 8 to 10 am	**109**	**33**	30	-	3	0.6	18	10	9	14	3	12
06 June 7 to 8 am	**17**	**3**	16	**24.3**	2	0.3	10	10	6	2	3	2
06 June noon	**81**	**13**	16	$\sim$ **80**	2	0.4	8	10	4	4	3	2

Table 5.2: Overview of successful plume transects along with relative standard deviations of the primary sources of uncertainty. Error estimation procedures are explained in the main text. Bold numbers represent estimated emissions and errors together with the respective E-PRTR 2014 entries in the fifth column, which are the mine-wise reported values distributed evenly to every single listed shaft of each mine. Several upwind sources do not allow accurate source attribution on 1 June, hence no E-PRTR estimate is reported. E-PRTR CH_4 sources contributing to the observations of the noon transect on 6 June amount to roughly 80 kt/a, if only considering mining ventilation shafts in the near surroundings (20 km radius). However, far upwind (60 km) ventilation shafts can influence the measurements although all mines located in direct wind direction are listed with 0 kt/a and reach 13 kt/a somewhat north of the mean wind direction. Table adapted from Luther et al. (2019)

5.6 Error analysis

According to Equ. 5.1, several terms contribute to the errors in the emission estimates Q in section 5.5: errors in $\Delta\Omega$, which partition into the error for background removal and the measurement error; errors associated with the effective wind speed U_{eff}, which partition into errors related to horizontal, vertical, and temporal averaging of the wind-lidar observations; and the errors in Δy_i, which are dominated by the errors in the relative angle between wind directions and driving directions and hence, are dependent on wind direction accuracy.

The measurement error attributed to XCH_4, is composed of the standard deviations among all measurements sampled during an individual stop of the stop-and-go pattern. For the noon transect on 24 May, these standard deviations reach a maximum of 4 ppb. Wind speeds of roughly 6 ms^{-1} and short distances to the mining shaft imply large variability in the CH_4 column above the FTS caused by atmospheric turbulence. For the morning transect of the same day, the relative CH_4 standard deviations for the first transect at the same shaft are lower (2 ppb). The actual FTS instrument precision for XCH_4 measurements is on the order of roughly 0.3 ppb, i.e. 0.02 % (Chen et al., 2016). Thus, the major part of the combined error estimate is driven by atmospheric variability with a very small part caused by the measurement noise.

The standard deviation of all possible combinations of non-plume signals observed before and after crossing the plume compose the error associated with XCH_4 background removal. During the generally 1 to 1.5 h long transects, an observation is defined as intra-

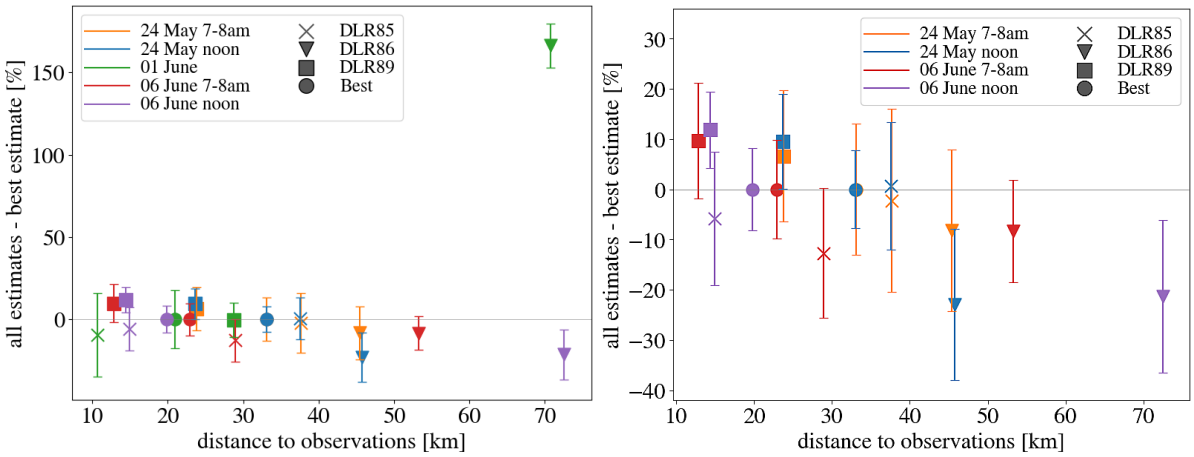

Figure 5.10: Relative differences between the best-estimate (weighted averaged) wind speed and sensitivity calculations using wind speed from individual wind lidars. Different colors represent different transects. Individual symbols refer to the wind information source used. The right panel is a zoom of the left panel, but it omits data from 1 June. Figure adapted from Luther et al. (2019).

plume if the absolute difference between two consecutive measurements is at least 0.5 ppb greater than the average standard deviation of all measurements. As illustrated by gray dashed lines in panel a) of Fig. 5.5, all possible background estimates are linearly fitted. The best estimate background is determined as the average of all possible background options. The standard deviation calculated from all these options is considered in the final error budget. The final plume enhancements ΔXCH_4 are calculated as the difference of the best-estimate XCH_4 background and the XCH_4 values observed while crossing the plume. The standard deviation caused by the background uncertainties is always below 0.6 ppb. Therefore, their influence on the estimated emission values is considered to be small compared to, e.g. wind induced errors. On 6 June, the onboard in-situ measurements aided to locate the start and end point of the plume. The in-situ concentrations, measured on the fly guided the mobile FTS towards the south until the observed CH_4 concentrations were constantly low.

Errors related to the effective wind speed U_{eff} generally dominate the error budget. The baseline wind scenario averages all wind speed measurements throughout the PBL. It considers the errors arising from temporal wind speed variability during one plume transect as well as from distance-weighted averaging between the three wind lidars. The standard deviations among all wind speed measurements inside the PBL represent the error related to vertical averaging. The respective error estimates range from 8 % to 18 %, with the largest errors observed under low wind speed conditions as measured on 1 June ($U_{eff} < 2.5\,ms^{-1}$). The error due to temporal averaging of wind speed is represented by the respective standard deviations of wind speed during the averaging period. These errors range from 3 % to 9 %.

Three co-deployed wind lidars in the USCB deliver the advantage to assess U_{eff} errors

related to horizontal variability of wind speeds throughout the USCB. To this end, a sensitivity study calculates the emissions Q with wind information from each single wind lidar instrument, instead of using a horizontal average that is weighted by the distance between lidar and FTS as in our baseline scenario. Distances between wind measurements and XCH_4 observations range between 11 km and 72 km. Relative differences of calculated wind speeds U_{eff} are summarized in Figure 5.10 for all sensitivity runs with respect to the best estimate baseline scenario (reported in section 5.5).

With increasing distance between the FTS and the wind lidar locations, the differences between the wind speeds also generally increase. Except for distances exceeding 40 km and for low wind speed conditions such as encountered on 1 June, the differences range between 1 % and 13 %. For low wind speed conditions as on 1 June with $U_{eff} < 2.5\,ms^{-1}$, relative wind speed differences differ significantly, if wind information is taken from measurements more than a few ten kilometers away. Figure 5.10 also reveals, that using wind information from DLR89 tends to cause emission estimates that are generally higher than if other wind information sources are considered. The southern wind lidar DLR89 is likely influenced by the nearby lake, especially during the prevailing easterly winds. Low surface roughness and therefore low friction above the lake surface could cause the wind speeds – and with that the emission estimates – to be higher already in lower levels compared to the other sites located close to forests. For the discussed cases, the distance of the FTS to the closest wind lidar never exceeded 33 km and since distance-weighted averages of the wind measurements are considered, the error due to horizontal wind speed averaging is estimated with 10 %.

Wind direction uncertainties translate into errors of the cross-plume segment Δy_i. Similar to the error estimation procedures for wind speed, wind direction errors are estimated by means of vertical, temporal and horizontal averaging. These errors are generally smaller compared to wind speed errors. Except for the low wind speed day 1 June (14 %), vertical averaging yields a standard deviation of 2 % to 5 %. Temporal averaging induces errors ranging between 2 % and 3 % again except for low wind speed day 1 June with 12 %. The error due to horizontal wind direction averaging is stated with 3 % according to the procedure explained to estimate the horizontal wind speed averaging error.

Generally, the above mentioned individual error contributions are propagated into the reported emission errors for Q by Gaussian error propagation. The error budget is dominated by error contributions from estimating the effective wind-speed U_{eff}. Figure 5.11 depicts an overview of all wind situations for all transects. Every measurement during the transects is represented by a single circle referring to a certain time during the transect and the circle size indicates the total relative U_{eff} error (calculated through Gaussian error propagation from the individual contributions summarized in Table 5.2). Solid circles mark the wind information considered to be the best guess estimate. Transparent circles indicate data from the sensitivity study, which is based on the individual wind lidar observations. The transects reported in this study are generally observed during easterly wind conditions. The wind speeds varied between $4\,ms^{-1}$ and $8\,ms^{-1}$ for all cases except for 1 June, which suffered from generally low wind speeds which translates into a challenging emission estimation.

Summarized, we demonstrated passive, ground-based, direct sunlight remote sensing

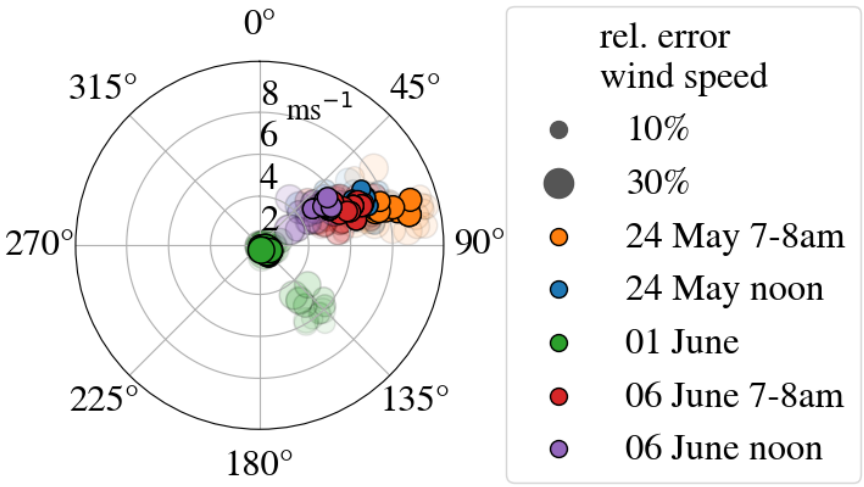

Figure 5.11: The wind rose indicates wind direction and wind speed as occurred during the transects. Different colors mark different days. Size of the circles corresponds to the relative standard deviation in % resulting from averaging wind speed horizontally, within the PBL, and over time. Solid circles mark the best-estimate wind information whereas transparent circles mark wind information that stems from the individual wind lidars directly. During the measurement periods, easterly winds prevailed. Note that for 1 June wind speeds are exceptionally low. Figure adapted from Luther et al. (2019).

of XCH_4 enhancements in the plumes of hard coal mining ventilation facilities several kilometers downwind of the sources. The plumes were crossed in stop-and-go patterns, with transect periods of 1 to 1.5 h. Combined with the observations of 3 co-deployed wind lidars we estimated the emissions for five transects on three days. The approach enables the emission estimation of CH_4 with good confidence (15 to 30 %). The resulting emission estimates range between 6 ± 1 kt/a for a single shaft and up to 109 ± 33 kt/a for a subregion of the USCB. These estimates are in broad agreement with the E-PRTR reports. However, the method is restricted to stable wind conditions and direct sunlight. Together with on-board in-situ CH_4 measurements and detailed wind information, a modified mobile FTS is a flexible, fast (1 to 1.5 h), and accurate (combined relative error of 15 to 30 %) possibility to estimate hard coal mining CH_4 emissions reliably.

Chapter 6

Emission estimation on regional scale

Chapter 5 dicussed the mobile FTS measurements and how methane emission estimates are obtained on facility scales. This Chapter combines observations of a FTS network with wind and methane dispersion information from models, and will finally estimate the methane emissions on regional scales, i.e. not single shafts but larger groups of ventilation shafts.

6.1 Campaign deployment and XCH_4 measurements

The USCB (section 4.1) is the area of interest for the CoMet measurement campaign. In contrast to CoMet0.5, the stationary FTS network now focuses on the whole area and not on a single part of the USCB. The reasons for that change in scale are discussed in section 4.5. The red triangles in Figure 6.1 mark the positions of the four EM27/SUN in the north, east, south, and west of the USCB mining shafts. The choice of suitable locations is limited by criteria such as: the location should be outside or at the edge of the USCB, have a wide field of view towards the Sun (south), have access to electricity at the instrument location, and provide accommodation for the instrument operators. The idea is to always have at least one instrument upwind of the USCB to serve as background instrument to calculate the methane enhancement produced by the activities in the USCB. The cases discussed in this study are limited to easterly wind conditions which always leads to the use of the eastern instrument ("The Glade") for background methane information. Thus, this work focuses on the downwind measurements of the instruments "Pustelnik" (southern station) and "Raciborz" (western station).

In addition, the instrument locations should generally allow for the comparison of the ground-based measurements with satellite data. In particular, the observations are intended to be compared against measurements from the spectrometer *TROPOMI* aboard Sentinel-5 Precursor launched in October 2017 (Hu et al., 2018; Lorente et al., 2021).

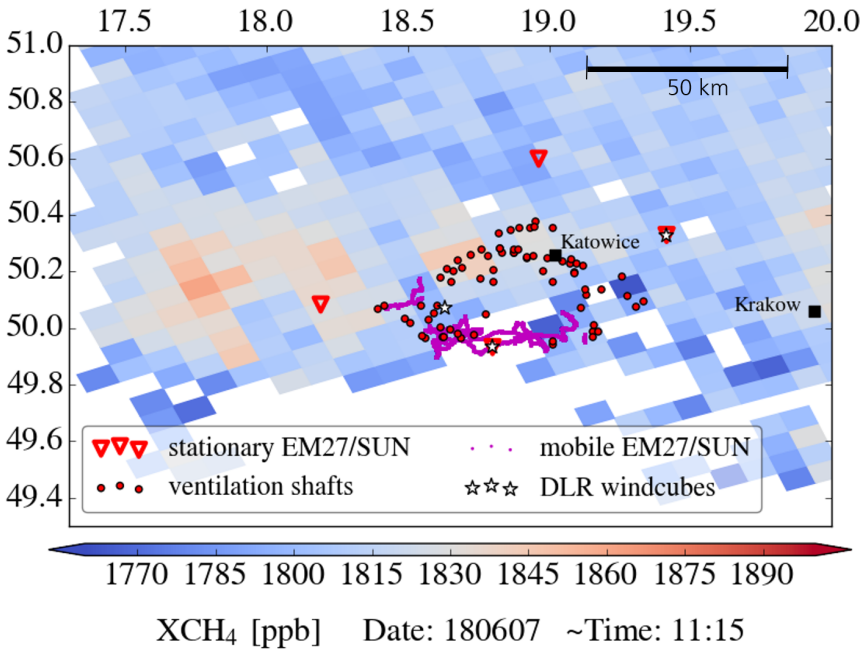

Figure 6.1: The USCB with the 4 stationary EM27/SUN as red triangles, red dots as mining shafts, white stars as wind lidars, and purple dots as mobile EM27/SUN tracks. TROPOMI XCH_4 data from a single Sentinel-5 Precursor overfly is displayed as colored background. The red tiles in the west of the mining shafts might be related to the USCB methane outflow during easterly winds.

TROPOMI's spatial resolution in kilometer is 3.5×7. Thus, to measure the methane outflow of the USCB where it is already mixed, one would look at a pixel at least 7 km away from the next mining shaft in wind direction. With the aim to validate the satellite data, the ground-based instruments are placed roughly 20 km outside the USCB except for the southern station which is located closer to the shafts due to a big lake in the south. The distance to the mining shafts allows the different methane plumes to merge and mix inside the planetary boundary layer to homogeneously fill a TROPOMI pixel. Due to sparse data coverage of the USCB during the campaign period, a comprehensive comparison of ground-based and satellite measured XCH_4 is not possible. For illustration purposes, the TROPOMI data are shown in Fig. 6.1 in the background. In the future, with longer deployments of the ground-based FTS, one would aim at detecting and validating the plumes in TROPOMI measurements. All available TROPOMI XCH_4 data observed during the FTS deployment are discussed in appendix B.

Each instrument has its own optical alignment and a specific ILS resulting in slightly different XCH_4 values even when measuring the same air mass. An effective method to calibrate these differences is to measure side-by-side at the same location and at the same time with all instruments and calculate scaling factors between them (Frey et al., 2015).

For the side-by-side procedure, four of the five instruments (including the mobile EM27/SUN) were placed at the southern station Pustelnik. Due to shipping complica-

tions the eastern instrument did not participate at the initial side-by-side deployment. This was repeated on 26 May 2018 at station Pustelnik but just with two instruments as the others already operated in their respective campaign locations.

Calibrating the measurements assures comparability and correct XCH_4 gradients. Fig. 6.2 displays XCH_4 observations before and after scaling at the beginning of the CoMet1.0 measurement campaign. We evaluated the calibration factors following Frey et al. (2015) via a least-squares fit. All four stationary instruments are calibrated against the mobile EM27/SUN. To calibrate all the field measurements with respect to TCCON, all five instruments are also calibrated towards the KIT TCCON station based on side-by-side measurements performed on 13 July 2017 with the mobile EM27/SUN. Table 6.1 lists the final scaling factors towards TCCON which includes the scaling towards the mobile EM27/SUN.

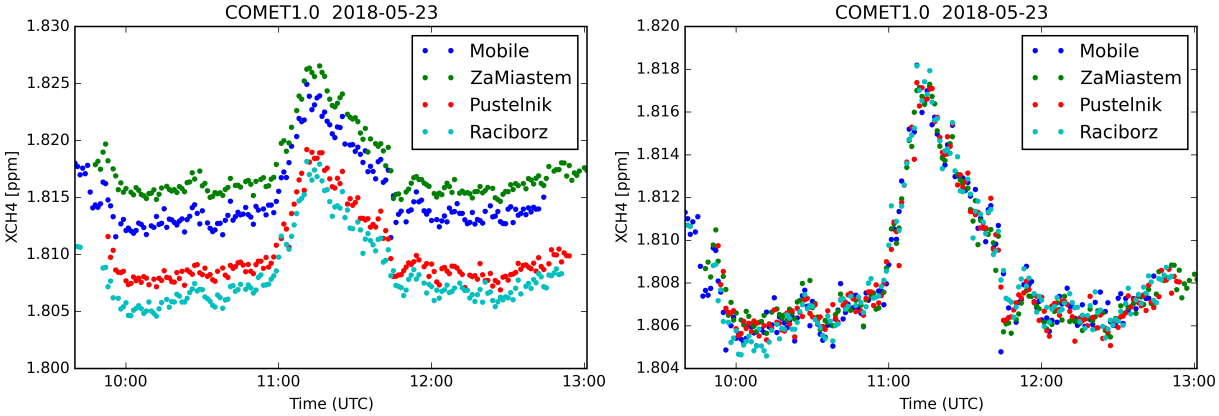

Figure 6.2: Side-by-side measurements at station Pustelnik on 23 May 2018 on the first day of the deployment. The left panel displays unscaled data with an average instrument-to-instrument difference of 5 ppb. The right panel shows measured XCH_4 after scaling with about 1 ppb instrument-to-instrument difference. Note, that the instruments detected a plume like structure at the beginning of the measurements and around 11:20 UTC.

Site	Lat. (°N)	Lon. (°E)	m a.s.l	XCH_4 scal.	O_2 scal.
Mobile	-	-	-	0.9961	1.0022
Za Miastem (N)	50.5989	18.9630	305	0.9999	1.0033
The Glade (E)	50.3292	19.4155	303	1.0003	0.9967
Pustelnik (S)	49.9326	18.7998	266	1.0011	0.9942
Raciborz (W)	50.0831	18.1917	223	0.9974	1.0063

Table 6.1: Scaling factors towards the Karlsruhe TCCON station for each instrument and species.

6.2 WRF as input for FLEXPART

This section covers the usage of WRF to generate input for the Lagrangian particle dispersion model FLEXPART which simulates the methane trajectories by using WRF output data, most importantly the 3-D horizontal and vertical wind fields. For this purpose, WRF V4 (Skamarock et al., 2019) is chosen. Figure 6.3 depicts the model set up, which is driven by GFS data (NCEP, 2017), in two domains.

The outer domain is focused on central Europe whereas the inner domain is centered on the USCB. Note, that the Tatra mountain ridge is completely enclosed by the inner domain to better represent mountainous modeling effects as e.g. outflow of the region towards the Czech Republic via the Moravian gate on the western boundary of the mountain ridge. The internal time step varies automatically according to the internal numerical situation. The output time step is set to write new data to the output file every five simulated minutes.

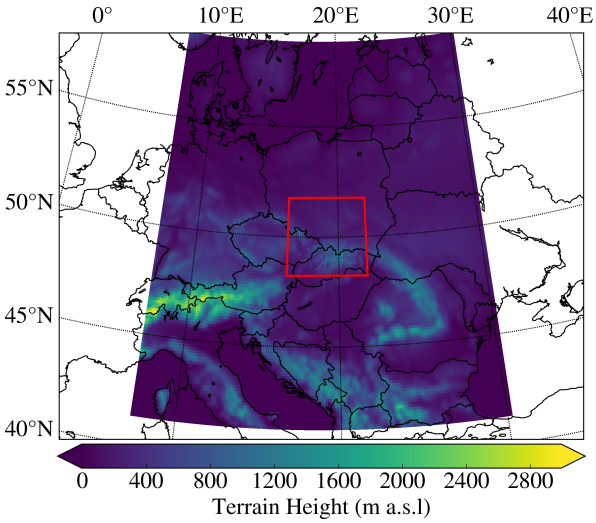

Figure 6.3: The two WRF V4 domains as set up to generate the FLEXPART input. The first domain (colored shape) has a spatial resolution of $\sim$ 15 km. The inner domain (red rectangle) has a spatial resolution of $\sim$ 3 km. The Tatra mountain ridge in the southern part of the second domain is fully enclosed by the inner domain.

WRF comes with the possibility to use observational data as input via the Four Dimensional Data Assimilation (FDDA). During the CoMet measurement campaign, three Doppler-wind lidars Leosphere windcube (see section 5.3) were deployed in the target area. These deliver ten minute resolved wind profiles throughout the campaign period and reach up to roughly 4 km if no clouds disturb the laser beam.

The FDDA option makes it possible to let WRF adapt its computations to these observations. The level of adaptation can be adjusted with different parameters, e.g. radius of influence r_{xy}, time window Δt and horizontal wind coefficient c_{uv}. The selection of parameter settings to obtain the best possible results is demonstrated in Kostinek et al. (2020) for the same region and during the same time period. Further details including ensemble runs to find the best parameter synergy can be found in above mentioned study and are not further explained here. Instead, a direct comparison between the WRF results and the wind lidar observations is presented.

Figure 6.4 displays a comprehensive overview of the wind situation for three case studies discussed within this thesis, 28 May, 6 June, and 7 June 2018. The two panels compare wind speed (left) and wind direction (right) extracted from the WRF model, with wind

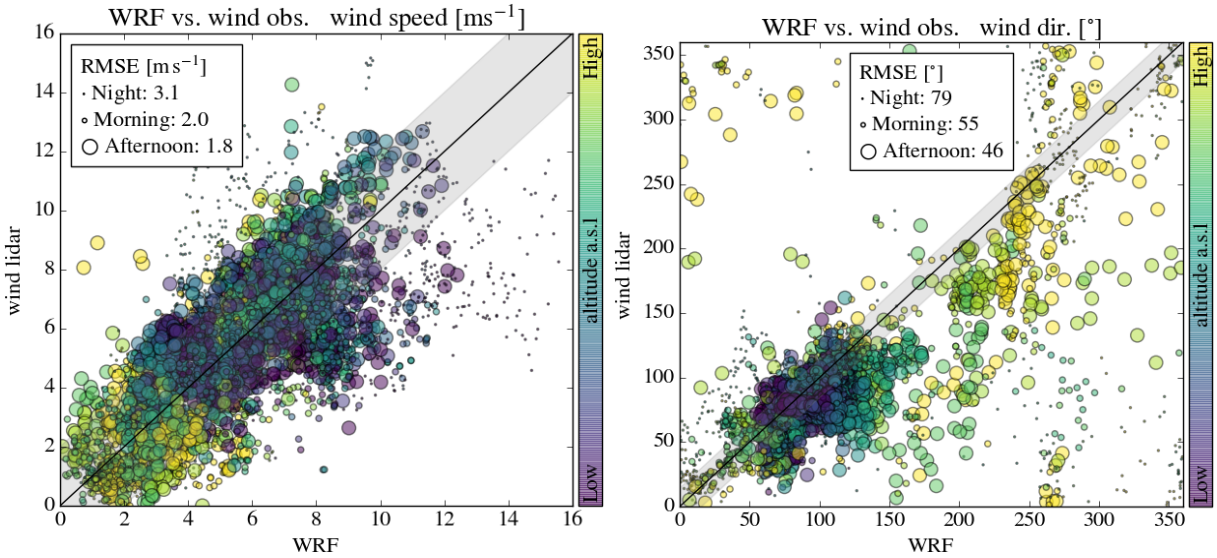

Figure 6.4: Comparison of WRF wind estimates and wind lidar observations at the three actual lidar positions. The data includes measurements from 00UTC to 18UTC of each of the three measurement days discussed here. Dots represent night values (00 to 6UTC), small circles represent morning values (6 to 12 UTC), and big circles represent afternoon values (12 to 18UTC). Shaded areas include roughly 80 % of the data points for $\pm 2\,\mathrm{ms}^{-1}$ for wind speed in the left panel and include roughly 50 % of wind direction measurements in a $\pm 15°$ range in the right panel. The height is indicated in arbitrary units as the boundary layer during night time is lower than during daytime and possible cloud cover interferes with the lidar range. This may lead to wrong interpretation of the wind situation in upper layers, if wind information is tied to actual height information.

lidar observations. The data sets include observations from 00UTC to 18UTC of each day and split into night, morning, and afternoon visible as marker size ranging from small dots, circles, to big circles respectively. The altitude of each sample pair is color coded in arbitrary units. Yellow colors correspond to the upper most levels of the observations. The lidar range limits the comparison to a maximum of about 4 km above the instrument if no clouds are blocking the laser beam, whereas WRF wind information is available up to roughly 12 km a.s.l.. As clouds can interfere with the wind lidar's laser beam the top lidar measurement level varies strongly with the bottom level of the clouds, which is strongly related to the boundary layer height. Different cloud types can form at the top of the boundary layer which may disturb the lidar. The boundary layer height varies during the day starting from a few hundred meters above the ground during the night and morning hours and ranging up to 1500 m during the afternoon, when there is maximum convection (see also Figure 5.3). As the boundary layer height varies, so does the cloud bottom height vary and the lidar reaches to different height levels during the day. Especially in the afternoon with mostly cumulus humilis clouds the height of the boundary layer drops during a few hours to the minimum height. Labeling the level of each measurement with its

exact altitude information is misleading as low observation levels can already be outside the boundary layer during night or morning time or could be blocked by clouds in the afternoon. This is the reason, why height information is displayed in arbitrary units in Figure 6.4 and the highest (yellow) value always represents the top observation limit which may vary with cloud cover or represent different atmospheric layers, with different wind properties. The yellow coded markers always refer to levels close or above the boundary layer. The lowest altitude levels always refer to the lowest possible comparison possibility which is always roughly 100 m above ground.

Wind lidar observation levels do not match the WRF grid levels exactly. To assure a reasonable amount of comparable data, a match between modeled and observed data is granted if the WRF wind level is within the range of ± 25 m around the level of observation. This represents all of the possible WRF wind levels but dismisses some of the wind lidar levels as the lidar data has a finer vertical resolution.

Both panels in Figure 6.4 display an identity line with a shaded $\pm 2\,\mathrm{ms}^{-1}$ shape for wind speed in the left panel and a shaded $\pm 15°$ shape for wind direction in the right panel. For wind speed, about 80% of the data points are within the shaded range. For wind direction, it is roughly 50%. Wind speed modeling shows biggest discrepancies during night times which also appears as maximum root mean square error (RMSE) of $3.1\,\mathrm{ms}^{-1}$. Wind direction modeling shows lowest discrepancies during the afternoon and highest during the night. Note, that values close to 0° and 360° represent virtually the same wind direction but may introduce an error to the RMSE calculations, as the residuals can be as high as 359°). A lot of these values are observed during the night hours (lower right corner in the right panel of Figure 6.4). It is also apparent from the right panel, that the residuals for wind direction in the upper levels (yellow colors) are higher than for lower levels. This may be influenced by differences in the atmospheric boundary layer height between the model and the measurements. In the boundary layer, turbulence and eddies influence wind speed and direction. Above the boundary layer wind speed and direction tend toward geostrophic conditions. This may lead to big discrepancies between model and measurement if the border of boundary layer and free atmosphere is wrongly modeled. In general, methane plumes disperse inside the boundary layer and move decoupled from the free atmosphere above, in particular regarding short time scales as discussed within this thesis. For plume dispersion, darker marker colors are more relevant than yellow markers.

When only considering the methane measurement time frame each day from roughly 7 UTC to 17 UTC Fig. 6.4 reduces to Fig. 6.5. The height information is omitted in Fig. 6.5, as during the day, the wind speed during mid-latitude, convective, summer situations is nearly independent of height (Holton, 1973). It is apparent, that during the three campaign days presented in this thesis, the prevailing wind direction (right panel) is northeast to southeast and prevailing wind speeds range from $4\mathrm{ms}^{-1}$ to $9\,\mathrm{ms}^{-1}$.

Additional elimination of the top two layers of the matched data set, reduces the wind direction RMSE from 38° to 26° indicating inaccuracies of the model to simulate the PBL height or the wind direction close to the top of the PBL. The comparison of wind lidar data with simulated wind information for the presented methane observational time frame yields an RMSE for wind speed of $1.7\,\mathrm{ms}^{-1}$ and an RMSE for wind direction of 26°.

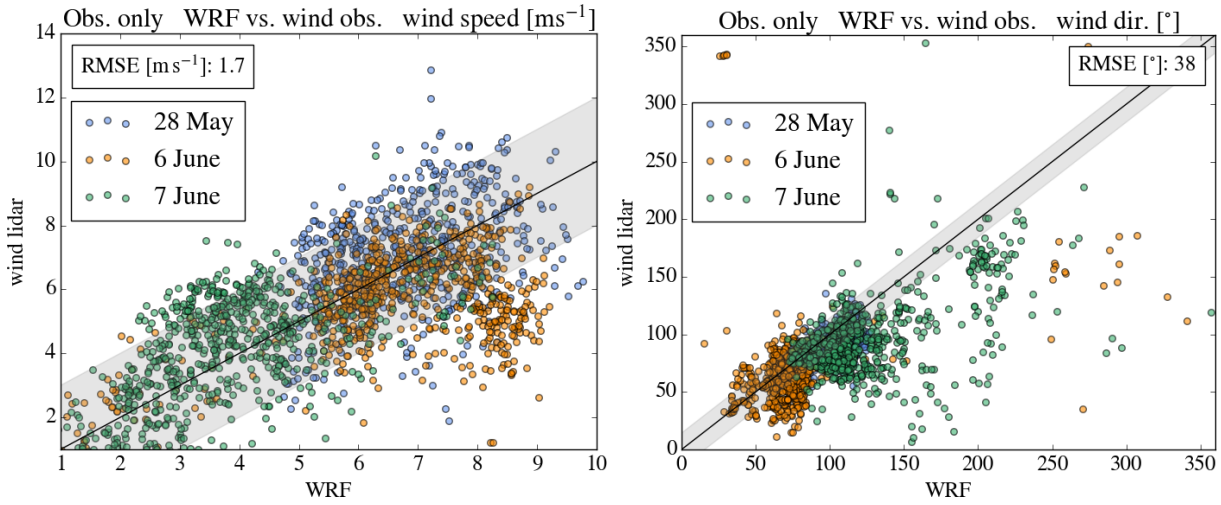

Figure 6.5: Comparison of WRF wind estimates and wind lidar observations for the observational period between 7 UTC and 17 UTC for the three case studies 28 May (blue), 6 June (orange), and 7 June (green). Shaded areas include roughly 80 % of the data points for $\pm 2\,\mathrm{ms}^{-1}$ for wind speed in the left panel and include roughly 50 % of wind direction measurements in a $\pm 15°$ range in the right panel. Wind direction simulations differ most from the observations for 7 June (green), a day with generally lower wind speeds, than the other two discussed cases. This indicates wind information uncertainties, when it comes to low wind speeds.

6.3 Lagrangian methane simulations using FLEXPART

The windfields modeled by WRF are used to drive the trajectory calculations in FLEXPART. For the trajectories, every known coal mining shaft in the USCB is set to emit 50 000 particles with a total mass of 10^5 kg in the model environment over the simulation period of 17.6 h from 00:10:00 UTC until 17:50:00 UTC at the day of interest. Although the measurements are limited to direct sunlight, the simulations already include the night before to account for long air parcel travel times from the furthest shafts to reach all instruments of the region. The trajectories start at every shaft location in a 10 m x 10 m x 10 m box on the ground.

Lagrangian particle dispersion does not rely on gridded numerical calculations, however, the model output can be provided in grid form which in this case are 100 x 100 boxes stacked in 24 layers with a horizontal resolution of roughly 1.3 km. The 24 individual height levels increase from 25 m near ground up to 500 m at the models top boundary at 3 km. The output timestep is 6 min. Note, that the CH_4 simulations only consider the shaft-wise emissions of the USCB. The atmospheric CH_4 background is not modeled, since the comparison with the observations is restricted to the pure CH_4 enhancements emitted by the USCB coal mines. The FLEXPART enhancements are given in ng CH_4 per m^2. All FLEXPART boxes above the measurement instrument locations are summed up to receive simulated column enhancements ($\Delta\,XCH_4$) for each FTS location and for

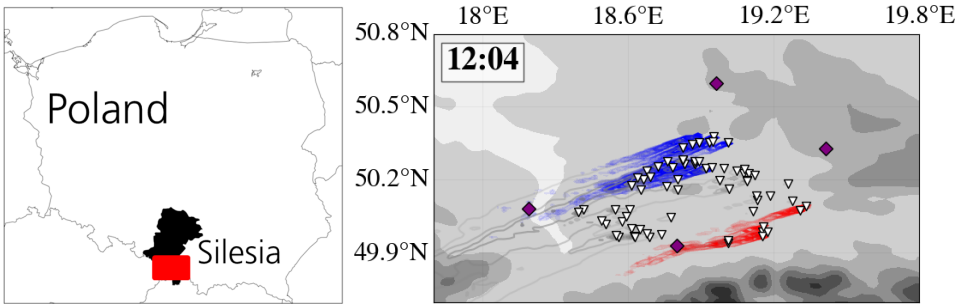

Figure 6.6: Approximate FLEXPART domain location in Silesia, Poland in the left panel. The red rectangle represents the outline of the FLEXPART simulations displayed in the right panel. The simulations show coal mine emission plumes for every shaft in the USCB for noon on 6 June 2018.

every timestep of the model. The FTS generally sample the atmosphere once every minute and the FLEXPART CH_4 output is interpolated to that temporal resolution. After unit conversion from ppm on the observational side to ng m^{-2} on the modeled side, simulated and observed CH_4 enhancements can be compared.

Figure 6.6 shows Poland and Silesia with the approximate FLEXPART domain in red on the left panel. The right hand side panel is an example of a simulation snapshot of the USCB mining ventilation shafts and their methane emission plumes for noon on 6 June 2018. Purple diamonds represent the stationary FTS in the four cardinal directions. North-easterly winds dominate the scene. Red plumes affect the southern measurement station (Pustelnik), blue plumes affect the western instrument (Raciborz). Gray plumes do not affect any measurement station.

Similar to the WRF ensemble described in Section 4.3, the FLEXPART simulations are also iterated with slightly different input parameters to provide an uncertainty analysis. The ensemble consists of seven runs: the `CONTROL` run with best guess input, the `WINDp5` run with +5° wind direction change of the whole wind field, the `WINDm5` run with −5° wind direction change of the whole wind field, the `SPEEDp06` run with the wind speed increased by 0.9 m s^{-1}, the `SPEEDm06` run with the wind speed decreased by m s^{-1}, the `PBLp100` run with the PBL height increased by 100 m, and the `PBLm100` run with the PBL height decreased by 100 m. In addition an a-priori run is simulated with the E-PRTR shaft-wise emissions as input.

Another application of the FLEXPART simulations within this work is to model the air mass travel time through the USCB, as schematically displayed in Fig. 6.7. The observed XCH_4 enhancements are dependent on this travel time, as ΔXCH_4 is calculated as the difference of downwind and upwind XCH_4 measurements. Since the distance between upwind and downwind instruments can exceed 50 km, an instantaneous comparison of upwind and downwind observations would generally introduce an error. Hence, it is preferred to compare upwind and downwind observations of roughly the same air mass, which crosses the individual FTS at different points in time.

To this end, a virtual methane source is implemented, emitting at the location of the

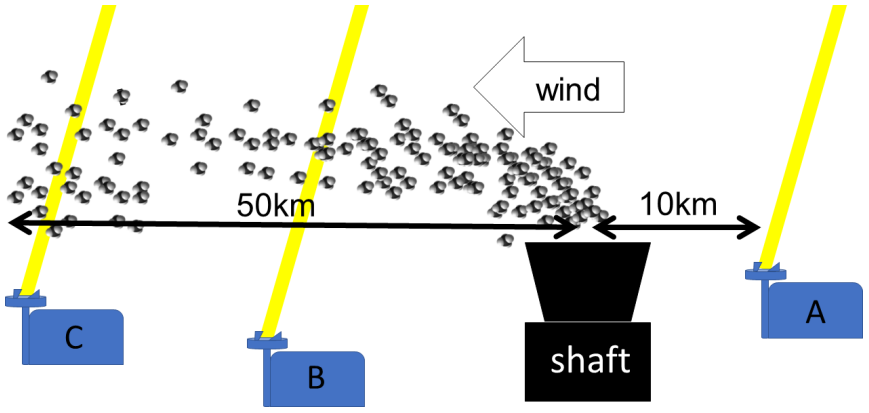

Figure 6.7: Schematic display of the Lagrangian time lag. Instrument A measures the background methane concentration. The methane enhancements induced by the emissions of the shaft are calculated by subtracting the background measurements from the observations of instruments B and C. Depending on wind speed, the air mass measured by instrument A will reach instrument B and C after a different travel time. The Lagrangian background calculations consider the time delay for each downwind instrument.

background instrument, and individually initialized at the time of the first methane observation for each case study. As the upwind and downwind instruments are generally not in line with the wind direction, the virtual plume released at the upwind location does eventually not reach the downwind instrument. However, the air mass travel time is estimated as the period required for the virtual methane plume to first cross the downwind instruments' notional line, perpendicular to the wind direction. Thus, the observational XCH_4 enhancements are calculated as the difference between the downwind FTS measurements, and the background FTS measurements shifted forward in time. This time dependent background is called *Lagrangian* background as it is flow following, i.e. moving together with the "observer" as in any Lagrangian model. From east to west, the simulated travel time for methane in the course of this thesis ranges from 1.5 to 4.6 h depending on wind speed and the target station.

The presented modeling framework is set up to simulate methane emission measurements, which are then compared to actual methane observations. From the simulation-measurement departures, shaft-wise scaling factors to the forward model emissions are then estimated by a minimization procedure explained in section 6.4.

6.4 Phillips-Tikhonov regularized emission estimation

The previous section illustrated how methane columns can be simulated with a Lagrangian transport model. The resulting residuals between modeled and measured CH_4 enhancements are minimized by scaling the simulated shaft contributions to fit the observations best. This inversion method is used to estimate source rates on regional scale as well as

their uncertainties, introduced by a model ensemble and the observational noise. The here presented inversion method follows the Phillips-Tikhonov regularization formalism introduced for the spectral retrieval of CH_4 in section 3.3. Its application to estimate regional coal mining emissions is discussed below.

The FLEXPART CH_4 enhancements $\mathbf{K}$ (m $\times$ n) with the dimensions of m coal mining shafts, each with n simulated enhancements representing the observational period, describe the forward model. To account for forward model uncertainties, an ensemble of seven model runs is introduced (see previous section 6.3). The following discussion will be focused on the `CONTROL` run of the ensemble, which is based on the best guess meteorological input parameters. The other six ensemble members with slightly altered meteorological variables provide the error range of the emission estimates and are in general not discussed individually.

Observed XCH_4 enhancements $\mathbf{y}$ of dimension n, are calculated for each downwind FTS with respect to the Lagrangian background as discussed in section 6.3.

The "state" vector $\mathbf{x}$ consists of m factors (without unit), which individually (each case study, one scaling factor per shaft and day) scale the simulated enhancements of each coal mining shaft m in $\mathbf{K}$ in a way, that the residuals $\|\mathbf{K}\,\mathbf{x} - \mathbf{y}\|_2$ become minimal. The minimization is realized via a least-squares fit.

Without further treatment, the solutions of $\min \|\mathbf{K}\,\mathbf{x} - \mathbf{y}\|_2^2$ tend to deliver physically impossible values for the finally retrieved emission estimates, e.g. negative values. Negative scaling factors $\mathbf{x}$ are avoided by only allowing for positive solutions, i.e. by using a non-negative least squares solver for the minimization problem.

Furthermore, the idealized forward model can not represent the true atmospheric state, i.e. the inverse problem becomes ill-posed in a sense that the measurements do not contain unambiguous information on the emissions. This eventually leads to unrealistically high emission estimations, which even are physically impossible, but are mathematically the perfect solution.

One approach to avoid unphysical solutions is to regularize the ill-posed problem, by including a-priori knowledge of the emitting sources. For that purpose, the Phillips-Tikhonov inversion method introduced in section 3.3 is used here to consider approximate emission information for each coal mine ventilation shaft. The a-priori information $\mathbf{x}_\mathrm{a}$ (of dimension m) comprises the E-PRTR annual emissions for each shaft, converted to relative (without unit) emissions with respect to the total, shaft-wise released mass in the model, for the simulation period.

The inclusion of a-priori knowledge into the minimization problem $\min \|\mathbf{K}\,\mathbf{x} - \mathbf{y}\|_2^2$ is formally described following Phillips (1962); Tikhonov (1963); Twomey (1963)

$$\mathbf{x}_\lambda = \min \left\{ \|\mathbf{K}\,\mathbf{x} - \mathbf{y}\|_2^2 + \lambda^2 \, \|\mathbf{I}\,(\mathbf{x} - \mathbf{x}_\mathrm{a})\|_2^2 \right\} \tag{6.1}$$

with the solution $\mathbf{x}_\lambda$ (of dimension m), the modeled CH_4 enhancements $\mathbf{K}$, the scaling factors $\mathbf{x}$, the observed CH_4 enhancements $\mathbf{y}$, the regularization parameter λ, the identity matrix $\mathbf{I}$ (m $\times$ m) containing ones on the diagonal, the a-priori information $\mathbf{x}_\mathrm{a}$, and the L_2 norm $||\cdot||_2$.

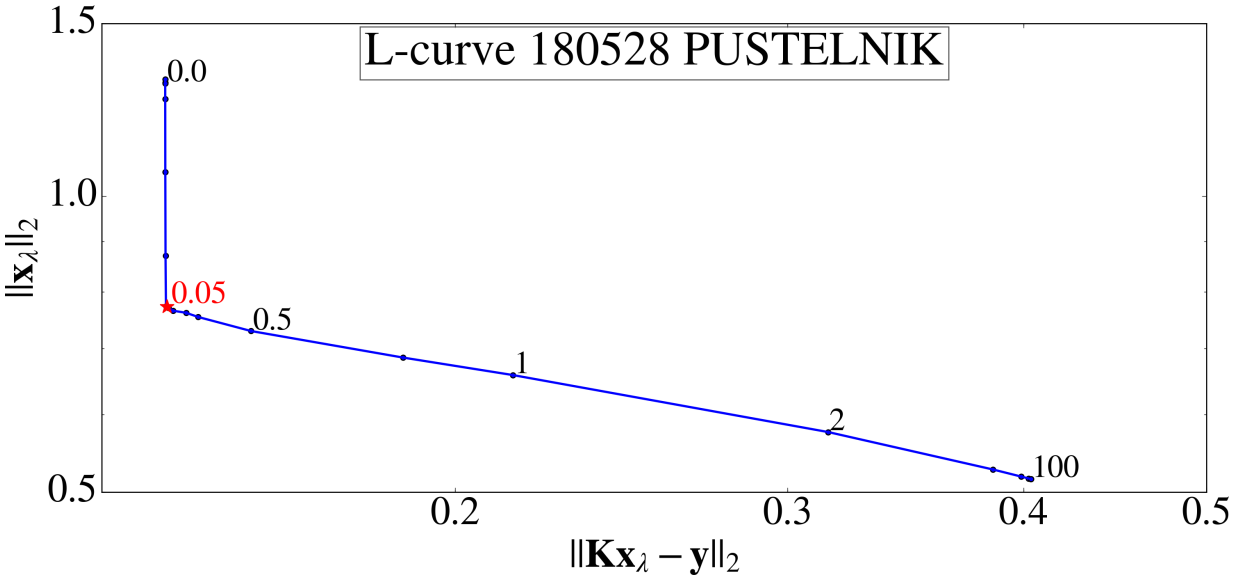

Figure 6.8: L-curve of the southern station Pustelnik of the Phillips-Tikhonov regularized least squares fit between simulated measurements and observations on 28 May. Different regularization parameters λ are labeled next to the dot markers along the blue curve and range from 0 (no regularization) to 100 (strong regularization with the a-priori as resulting emission estimate). The edge of the "L" ($\lambda = 0.05$) marks the chosen regularization parameter which fits best to avoid each, under- and over-representing the a-priori.

The presented Phillips-Tikhonov regularization (Equ. 6.1) gives all point sources a flexible allowance reaching from no restriction ($\lambda = 0$), i.e. zero regularization to strong regularization (for large λ) which leads to the a-priori input as solution. Increasing the regularization parameter λ increases the weight on the second term of the equation which basically leads to minimizing the residuals between the model and the a-priori. Since the solution $\mathbf{x}_\lambda$ scales the modeled emissions, the finally retrieved emissions do not considerably differ from the E-PRTR annual averages for high λ. It is important to find the right trade-off between strong regularization (and not much information gain compared to the a-priori) and weak regularization which may lead to unphysical emission estimates. This trade-off can be handled with the regularization parameter which is individually chosen for each case study, based on graphical L-curve identification (Hansen, 1992; Hansen and O'Leary, 1993; Golub and Von Matt, 1997; Hansen, 1999; Calvetti et al., 2000; Johnston and Gulrajani, 2000; Hase, 2000; Butz et al., 2011; Schepers et al., 2012; Butz et al., 2012; Sussmann et al., 2012; Borsdorff et al., 2014; Maasakkers et al., 2020).

Figure 6.8 displays an example of a L-curve, visualizing the normalized residuals between the model and the measurements $\|\mathbf{K}\,\mathbf{x}_\lambda - \mathbf{y}\|_2$, plotted against the scaling factor $\|\mathbf{x}_\lambda\|_2$ for different regularization factors λ.

With increasing regularization (rising λ), the residuals, too, get bigger as the solution is pulled towards the a-priori which generally does not represent the truth. For a particular regularization parameter there is a clear edge, as the normed scaling factor remains basically

unchanged with further increased regularization. This edge shapes the "L" and also marks one possible choice for a reasonable regularization parameter, which is $\lambda = 0.05$ for the example in Fig. 6.8.

The implementation of the Phillips-Tikhonov regularization follows (Hansen and O'Leary, 1993; Hansen, 1999; Golub and Von Matt, 1997). With simple matrix construction of

$$\mathbf{C} = \begin{bmatrix} \mathbf{K} \\ \lambda\,\mathbf{I} \end{bmatrix} \text{ and } \mathbf{d} = \begin{bmatrix} \mathbf{y} \\ \lambda\,\mathbf{I}\,\mathbf{x}_\mathrm{a} \end{bmatrix} \tag{6.2}$$

equation 6.1 reduces to

$$\mathbf{x}_\lambda = \min\left\{\|\mathbf{C}\,\mathbf{x} - \mathbf{d}\|_2^2\right\} \tag{6.3}$$

which is further treated with a non-negative least-squares solver. For this work, the `python` module `scipy.optimize.nnls` is used. This module solves the Karush-Kuhn-Tucker conditions for non-negative problems.

The solution $\mathbf{x}_\lambda$ is multiplied with the simulated emissions. Every shaft in FLEXPART emits the same arbitrary chosen mass of 10^5 kg spread over the whole simulation duration, $s_\mathrm{dur} = 17.6$ h. The estimated emissions, EE for each shaft expressed in kt a^{-1} are calculated as follows:

$$\mathbf{EE}(\mathbf{x}_\lambda) = \mathbf{x}_\lambda \cdot \frac{10^5\mathrm{kg} \cdot 24\frac{\mathrm{h}}{\mathrm{day}} \cdot 365\frac{\mathrm{day}}{\mathrm{a}}}{s_\mathrm{dur} \cdot 10^3\frac{\mathrm{kg}}{\mathrm{t}} \cdot 10^3\frac{\mathrm{t}}{\mathrm{kt}}} \tag{6.4}$$

The estimated emissions, **EE** can now be compared to inventory data for single shafts or summed up to compare regional emissions.

Two kinds of error are considered within the analysis: 1) Errors due to noise of the FTS observations. 2) Errors due to atmospheric variability, which generally dominate the error budget.

1) is addressed, by assuming that the CH_4 observations $\mathbf{y}$ are defined as $\mathbf{y} = \overline{\mathbf{y}} + \mathbf{e}$ with the observational noise, $\mathbf{e}$ and the unperturbed data, $\overline{\mathbf{y}}$. The FTS measurement noise is denoted with 0.6 ppb, based on the standard deviation of the averaged background measurements of two stationary instruments (The Glade and Za Miastem) from 7 UTC to 10 UTC on 28 May 2018 (see right panel in Fig. 6.9). The unit conversion of the measurement noise to the unit of $\mathbf{K}$ allows for the error calculation according to (Hansen, 1999)

$$\mathbf{x}_\lambda^\mathbf{e} = \min\left\{||\mathbf{K}\,\mathbf{x} - \mathbf{e}||_2^2 + \lambda^2\,\mathbf{I}\right\}. \tag{6.5}$$

Equation 6.5 translates the measurement noise $\mathbf{e}$ into that estimated emission component which remains unresolved. This component is dependent on λ, since with rising regularization strength, the influence of the observation on the emission estimates decreases and so does the influence of the measurement noise. Following equation 6.4, the pure observational noise component $\boldsymbol{\varepsilon}$ of the estimated emissions is calculated with $\mathbf{x}_\lambda^\mathbf{e}$.

2) To introduce atmospheric variability to the model, an ensemble of six additional model runs is set up which differ in basic meteorological parameters from the `CONTROL` run (see section 6.3). The ensemble includes changes of $\pm 5°$ wind direction, ± 0.9 ms^{-1} wind

speed, and ±100 m PBL height. For these model runs every shaft is a-priori assumed to emit the same amount of methane. In addition, an `a-priori` run is initialized, which relies on the shaft-wise E-PRTR emissions. This run does not contribute to the error estimation but illustrates the differences between the observations (and the converged emission estimates) and the a-priori emissions in the following discussion. The `a-priori` run generally reveals big residuals when compared to the observations. Note, that the initial guess of the forward model and the a-priori are different in our setup.

The standard deviation of all model runs σ_{ensemble} is summed (in quadrature) with the error caused by the observational noise $\boldsymbol{\varepsilon}$, leading to σ_{combined} which combines the errors discussed in 1) and 2):

$$\sigma_{\text{combined}} = \sqrt{\sigma^2_{\text{ensemble}} + \boldsymbol{\varepsilon}^2}. \tag{6.6}$$

For the case studies discussed in section 6.5, the errors of the emission estimates introduced by the observational noise range between $0.08\,\text{kt}\,\text{a}^{-1}$ and $0.54\,\text{kt}\,\text{a}^{-1}$ which is small compared to the errors introduced by the dispersion modeling ensemble which range between $16\,\text{kt}\,\text{a}^{-1}$ and $133\,\text{kt}\,\text{a}^{-1}$.

6.5 Case studies of the model based approach

Here, we employ the methodology developed in section 6.4 to six case studies. All case studies below generally involve easterly winds. As a result, the southern station Pustelnik is influenced only by a small group of shafts (6 to 13) in the southeast of the USCB. Whereas the western station Raciborz measures methane emitted by roughly 25 to 50 shafts. In all cases, the eastern station The Glade provides the XCH_4 background measurements. The estimated emissions are then compared to inventory data. In the following, three cases (28 May, 6 June, 7 June 2018) are described for the southern (Pustelnik) and the western (Raciborz) station. The simulated travel time which accounts for the Lagrangian background, ranges from 1.5 to 4.6 h depending on wind speed and the target station. The resulting emission estimates and their corresponding errors are summarized in Table 6.2.

6.5.1 28 May 2018

During the FLEXPART simulation period from 00:15 UTC to 17:30 UTC the winds mainly blow from the east, which is represented by the situation around noon in the top panel of Figure 6.9. All shafts north of 50.2 ° do not influence the simulated measurements. The wind speeds of 5 to $6\,\text{ms}^{-1}$ correspond to an air travel time from The Glade (eastern station) to Pustelnik (southern station) of roughly 1.5 h and to Raciborz (western station) of roughly 3 h. E.g. the air mass observed around 10 UTC at the western station Raciborz passed the upwind station The Glade about 3 h earlier. This time lag is considered for the XCH_4 enhancement calculation.

The sum over all FLEXPART levels at each pixel is the simulated measurement for each stationary EM27/SUN. The residuals between simulated measurements and actual

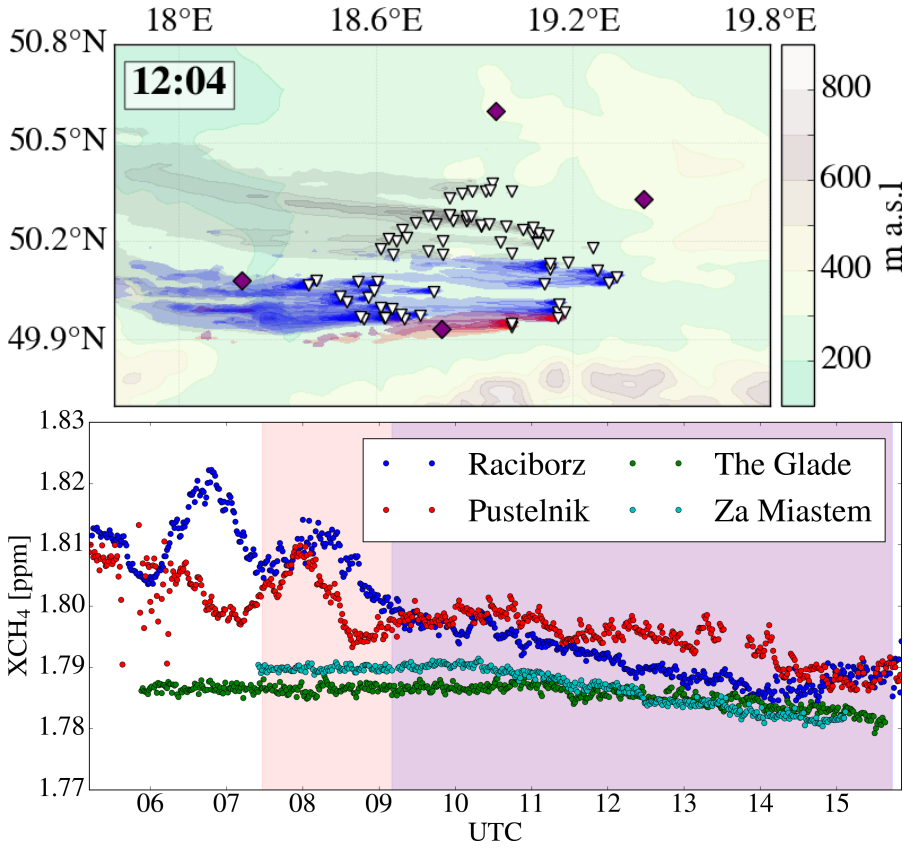

Figure 6.9: Top panel: FLEXPART simulation around noon on 28 May 2018 of the emitted methane and its dispersion through the USCB and above the four stationary EM27/SUN (purple diamonds). Coal mine ventilation shafts are depicted as white triangles. The USCB map includes terrain height information color coded from green (low) to white (high). The northern edge of the Tatra is visible on the bottom right. Colored plumes correspond to that fraction of the plumes influencing the respective EM27/SUN (blue = western station Raciborz, red = southern station Pustelnik, gray = plumes not affecting any station). The scene clearly indicates easterly winds. Bottom panel: EM27/SUN measurements of all four instruments. The northern instrument Za Miastem (cyan) and the eastern instrument The Glade (green), are not influenced by any methane from the USCB, and due to its upwind location, The Glade serves as background station. Blue (Raciborz) and red (Pustelnik) observations serve as downwind stations. The striking peaks during the morning hours of the southern and western instruments are most likely connected to night-time methane accumulation and subsequent transport with rising convection and mixing during the morning hours. The background colors indicate the time frames used for the inversion method considering the time lag due to travel times between downwind and upwind (The Glade) stations: red for just the southern station Pustelnik, and purple for both stations Pustelnik and Raciborz.

observed methane enhancements at every time step are minimized according to Equ. 6.1.

Western station Raciborz

Under easterly wind conditions, the western instrument Raciborz measured downwind of the mining shafts as depicted in Figure 6.9. The number of shafts which are involved in the simulated measurements varies during the day and amounts to a total of 49 of the 72 known mining shafts in the USCB. The Lagrangian time lag with respect to the background measurements is roughly 3 h. The observed methane enhancements are generally well represented by the regularized model (Fig. 6.10).

After convergence, the residuals amount to a mean bias of 2.2×10^{-7} kgm^{-2} and a root mean square error of 7.1×10^{-6} kgm^{-2}. The distinctly shaped L-curve (Fig. 6.11) indicates a regularization parameter $\lambda = 0.02$. Different regularization steps are depicted in Figures 6.10 and 6.12, to illustrate the convergence of $\mathbf{K}\,\mathbf{x}$ with the a-priori, with respect to a rising regularization parameter λ. For the remaining case studies, this illustration is omitted and just the a-priori and the final solution are discussed.

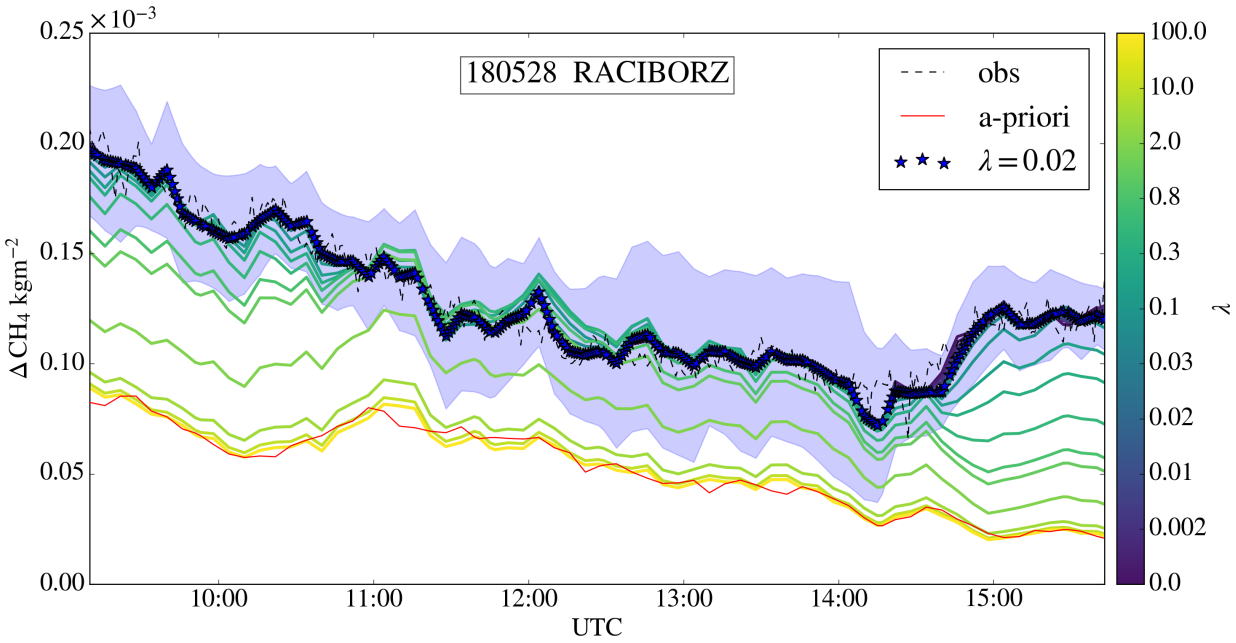

Figure 6.10: Simulated measurements (colored lines) compared to FTS observations (dashed line). The darker the color the lower the influence of the a-priori on the solution. Regularized solutions with high λ (green and yellow lines) generally match with the `a-priori` model run (red line) which is using the E-PRTR information as boundary condition for every shaft. Blue stars display the regularized solution for $\lambda = 0.02$ which is chosen to calculate the emission estimates. The blue background represents the combined standard deviation of the model ensemble and the measurement noise.

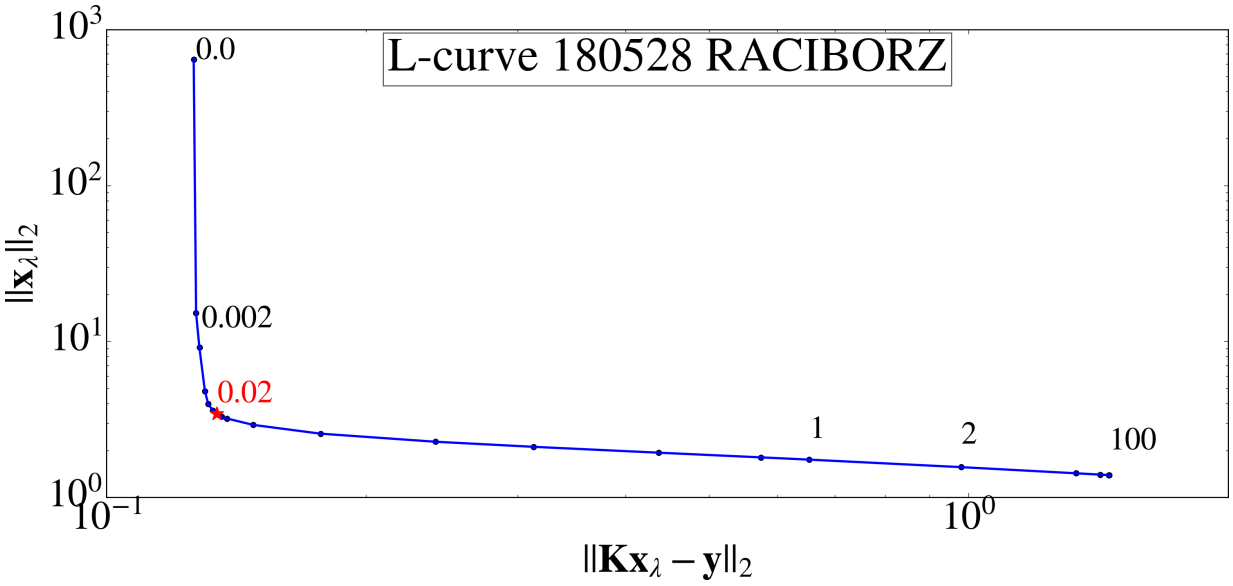

Figure 6.11: The L-curve shows a distinct L-shape which suggests the regularization parameter $\lambda = 0.02$ (red star).

Figure 6.12 depicts the estimated emission rates for the 49 involved shafts, calculated according to Equation 6.4. Uncertainty from the ensemble combined with the measurement noise are visible as error bars. With increasing regularization strength, the influence of the a-priori increases. This results in a decreasing error estimate from left to right for each bar, as the single ensemble members are pulled to the same shaft-wise a-priori values. With sufficiently high λ, all ensemble members show the same distribution of emission estimates which equals the a-priori emissions.

It is apparent from Fig. 6.12, that most estimates indicate higher emission values than the E-PRTR inventory suggests. The sum of the simulated emissions is with $846 \pm 133\,\mathrm{kt\,a^{-1}}$ roughly 2.2 times greater than the sum of the same shafts according to E-PRTR (roughly $377\,\mathrm{kt\,a^{-1}}$). The atmospheric variability introduced by the ensemble leads to a relative, total emission uncertainty of $\pm 16\,\%$. The error on the emission estimates caused by the observational noise $\boldsymbol{\varepsilon}$ is $0.39\,\mathrm{kt\,a^{-1}}$. Nonetheless, atmospheric and/or mining process variability hinder the comparison between snapshot measurements and annual mean inventory data, which needs to be considered for all discussed cases.

In general, the western FTS is influenced by more shafts than the southern FTS. More involved shafts come with more possibilities for the minimization procedure to find a reasonable, best fitting solution. However, the enhanced number of possibilities makes it more likely, that different contributing shafts are in line with the wind direction which aggravates the separation of individual shaft contributions. This might also be the case for shafts located close to each other.

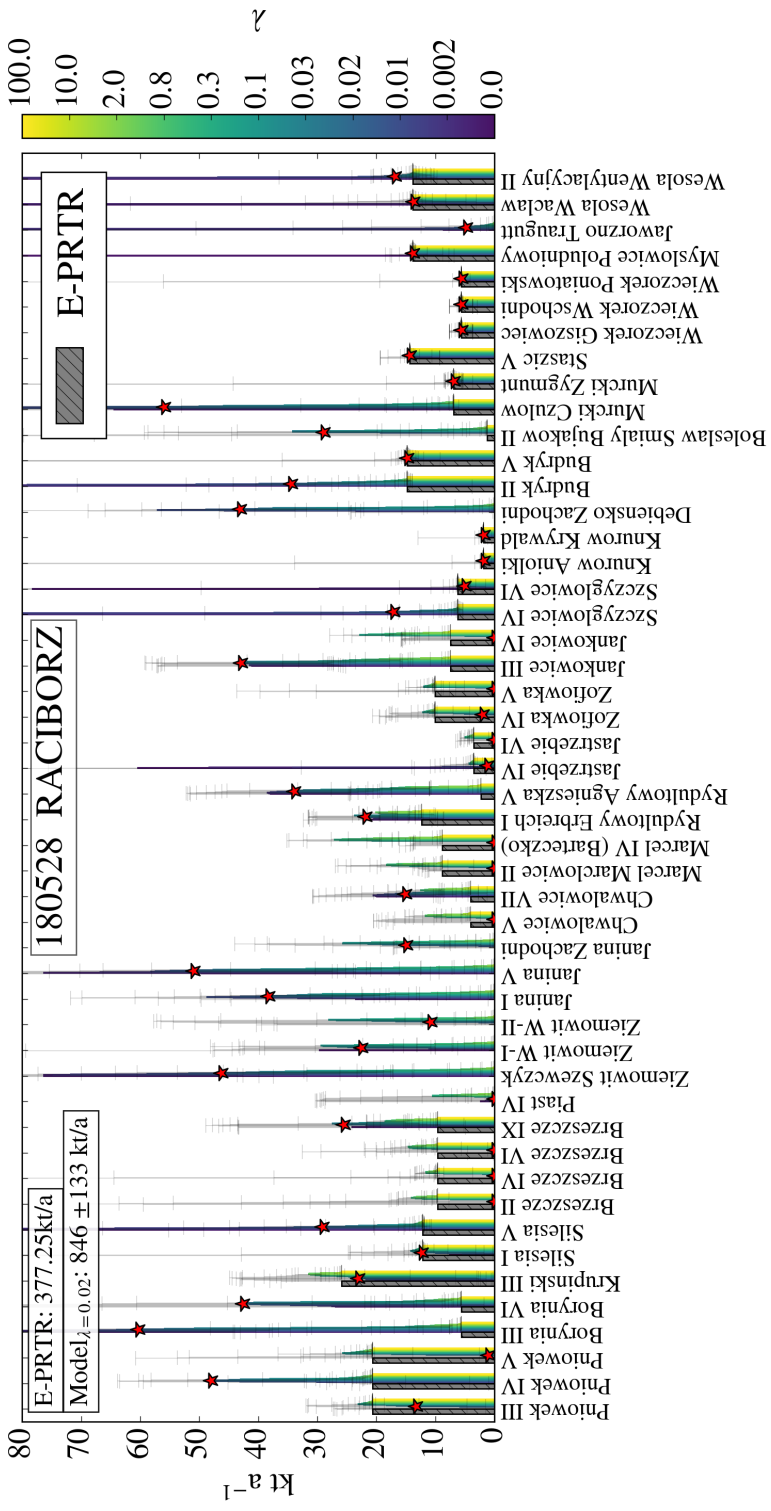

Figure 6.12: Estimated emission rates and their respective error bars containing the ensemble uncertainty and the measurement noise for the western station Racíborz on 28 May 2018. The regularization steps are color coded from dark to light colors with increasing λ. Red stars mark the final "best guess" estimate for each shaft originating from the `CONTROL` run for the regularization parameter suggested by the L-curve.

The estimated shaft-wise emissions in Fig. 6.12 are listed by the names of the coal mines. In general, shafts with the same name are also located within a few kilometers radius. For mines such as, e.g. Pniowek, Brzeszcze, Jankowice, and Murcki, the majority of the emissions is mainly constrained to one shaft within the respective group. However, for mines such as, e.g. Silesia, Janina, Budryk, Wieczorek, and Wesola the shaft-wise emissions seem to be independent of each other. This indicates, that single contributions within some groups of shafts cannot be identified by the forward model. Furthermore, uncertainties of the forward model most likely deteriorate the emission estimation, since small wind direction errors may affect multiple contributing shafts.

Southern station Pustelnik

Under easterly wind conditions, the southern station Pustelnik is influenced by two shafts from the "Silesia" mine and by two to four shafts of the "Breczceze" mine, depending on small wind direction changes of a few degrees. The minimization only considers these six shafts. The Lagrangian shift towards the background measurements is roughly 1.5 h.

It is assumed, that the forward model does not sufficiently simulate the observed methane enhancements (Fig. 6.13), at least for two periods in the morning (roughly until 10 UTC) and the afternoon (from 14 UTC on), since the modeled enhancements differ widely from the observations. This assumption is further endorsed by a significant deterioration of the L-curve shape, when these periods are included in the inversion routine. To this end, the morning and afternoon, (grayed out periods in Fig. 6.13) are excluded from further processing.

The exclusion of parts of the data set will recur for other case studies. In similar ways, the assumption remains, that high residuals between the converged estimates and the observations are related to forward model uncertainties, which is graphically diagnosed by a deterioration of the L-curve shape, if these periods are considered by the inversion routine.

The remaining residuals of the converged estimates in Figure 6.13 show some discrepancies between the simulations and the measurements with a mean bias of $3.8 \times 10^{-7}\,\mathrm{kg\,m^{-2}}$ and a root mean square error of $9.76 \times 10^{-6}\,\mathrm{kg\,m^{-2}}$. The number of shafts contributing to this scene is with a maximum of six relatively small. Additionally, all six shafts are generally in line parallel to the easterly wind directions. This leads to the system being prone to wind direction changes of a few degrees, since not all six shafts contribute continuously to the simulated measurements over the whole period.

The trade off between low residuals and high regularization is graphically solved by interpreting the L-curve in Fig. 6.14. In this case the chosen regularization parameter is $\lambda = 0.05$.

Every contributing shaft in the model has its individual emission estimate. These estimates are summarized in Figure 6.15 as blue bars, together with the combined uncertainty from the ensemble and the measurement noise, visible as error bars.

The error on the emission estimates caused by the observational noise $\boldsymbol{\varepsilon}$ is with $0.54\,\mathrm{kt\,a^{-1}}$ relatively large compared to the other discussed cases. This is related to the overall lowest

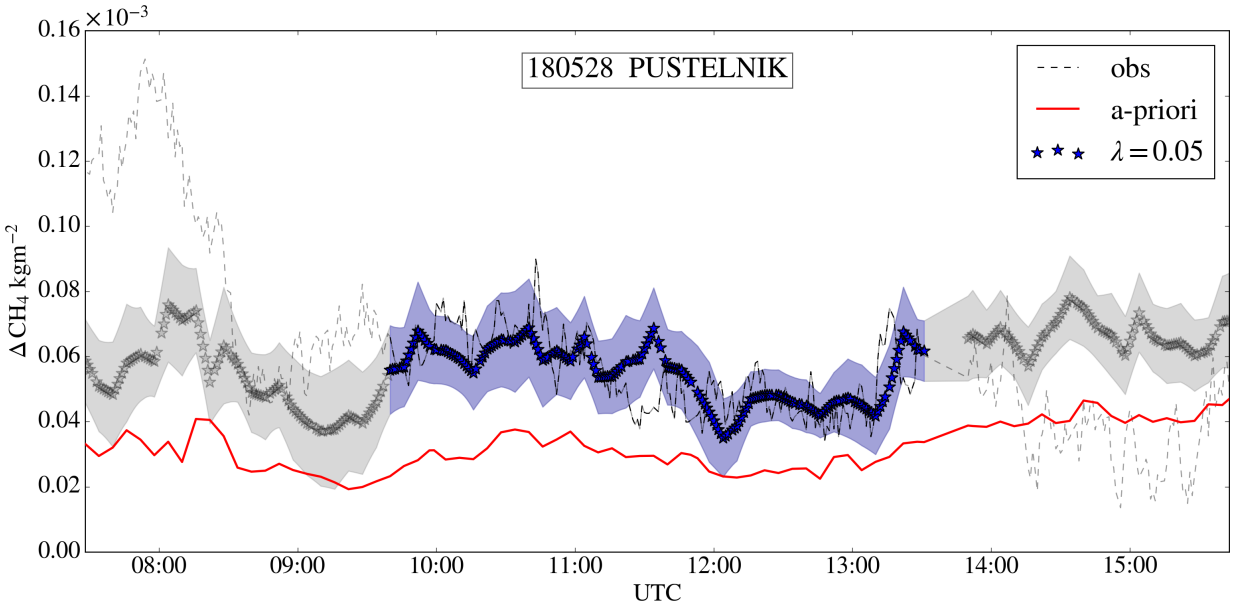

Figure 6.13: Simulated measurements (blue stars) compared to FTS observations (dashed line). Grayed-out periods are excluded from the regularization procedure, due to the forward model not being able to resolve this features; the gray stars show how the regularized solution would look like. The red line illustrates the enhancements, which are caused by the a-priori emissions. Blue stars display the regularized solution for $\lambda = 0.05$ which is chosen to calculate the emission estimates. The blue background represents the combined standard deviation of the model ensemble and the measurement noise.

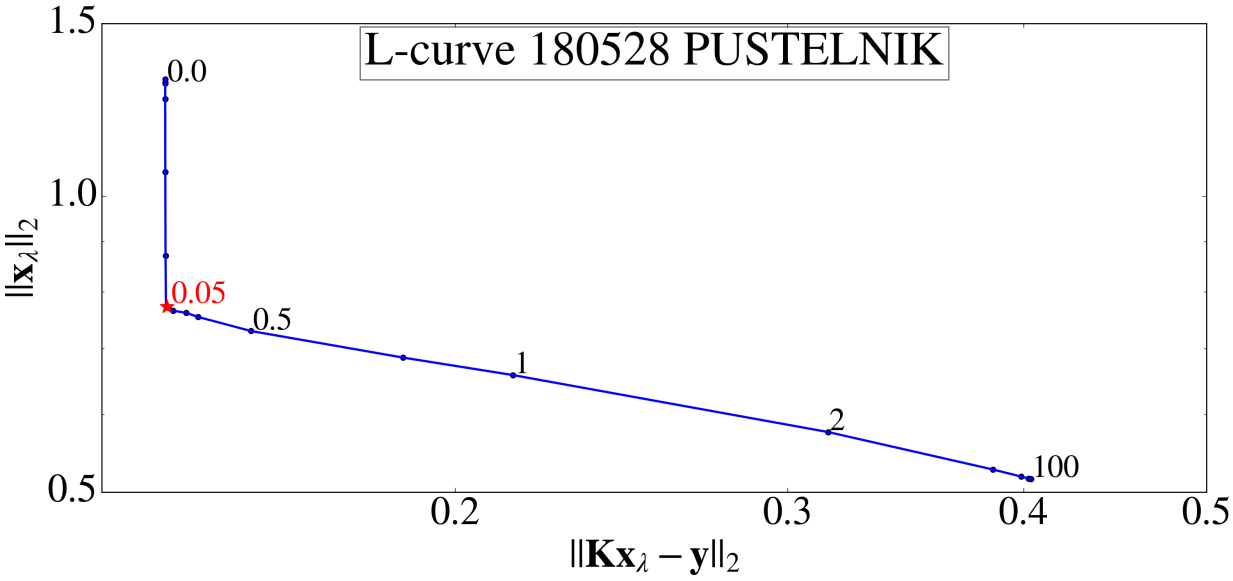

Figure 6.14: The L-curve shows a distinct L-shape which suggests the regularization parameter $\lambda = 0.05$ (red star).

XCH_4 enhancements for Pustelnik on 28 May. The observational noise of 0.6 ppb considered in the error budget has a greater impact on lower XCH_4 enhancements.

The sum of all contributing emission estimates is $76 \pm 24\,\mathrm{kt\,a^{-1}}$ for the six analyzed shafts, mostly originating from the Silesia mine, which is closer to the FTS than the Brzeszcze mine. The uncertainty of roughly 32% mainly introduced by the ensemble, indicates a high diversity of the individual model runs. The E-PRTR reports the respective emissions for all examined six shafts with $62.82\,\mathrm{kt\,a^{-1}}$ which is within the specified error range of our emission estimate.

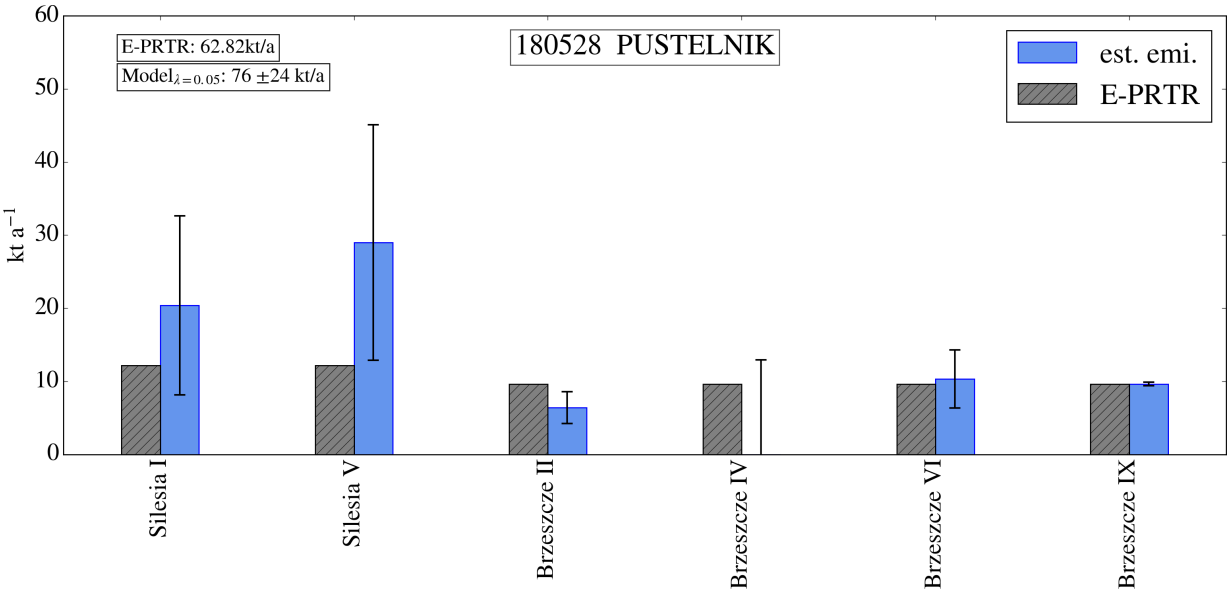

Figure 6.15: Estimated emission rates (blue bars) and their respective error bars containing the ensemble uncertainty and the measurement noise for the southern station Pustelnik on 28 May 2018.

6.5.2 6 June 2018

The general wind direction is northeast-north for the whole day in the area of interest (top panel in Figure 6.16). Mines like Krupinski ($25.9\,\mathrm{kt\,a^{-1}}$), Zofiowka ($21\,\mathrm{kt\,a^{-1}}$), Borynia ($11.2\,\mathrm{kt\,a^{-1}}$), and Pniowek ($61.8\,\mathrm{kt\,a^{-1}}$), which the E-PRTR lists with relatively high methane emissions, are in the center between the plumes which affect the southern and western station and do not influence the simulated measurements of either station. The observational time frames usable for the fitting procedure with respect to the Lagrangian background are roughly 7 h for Pustelnik and about 5.5 h for Raciborz. The Lagrangian time lag towards the background observations is about 2 h for the southern station Pustelnik and roughly 4.3 h for the western station Raciborz.

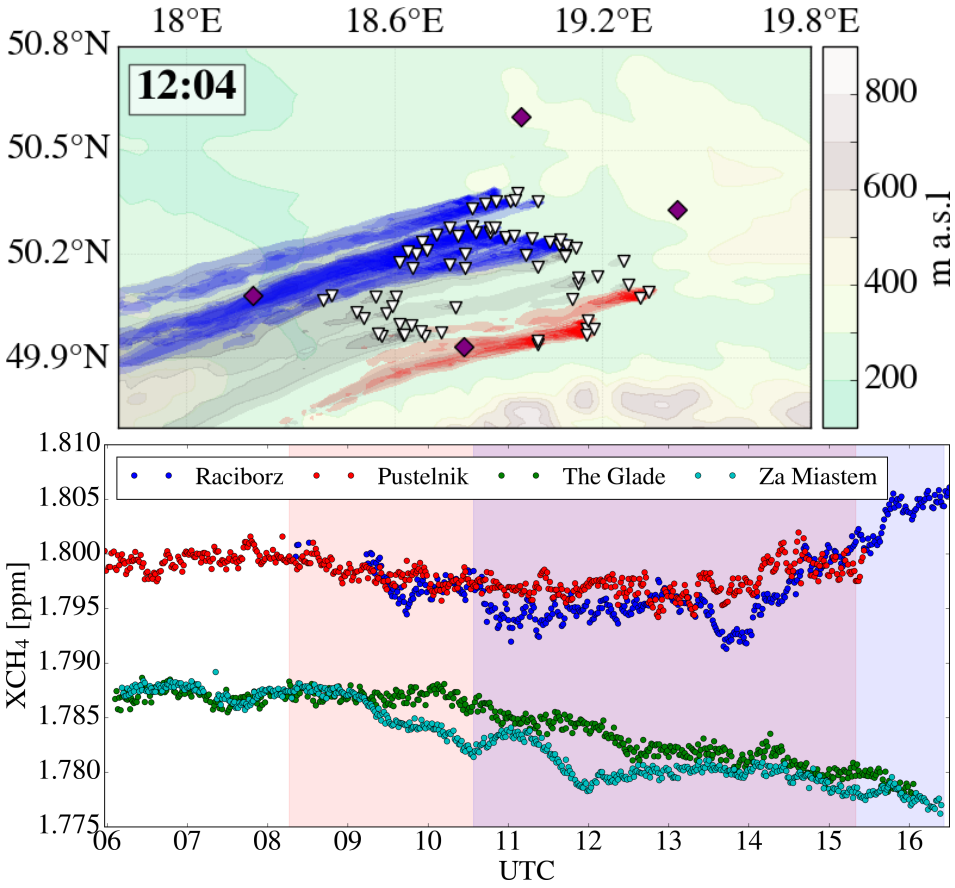

Figure 6.16: Top panel: FLEXPART simulation around noon on 06 June 2018 of the emitted methane and its dispersion through the USCB and above the four stationary EM27/SUN (purple diamonds). Coal mine ventilation shafts are depicted as white triangles. The USCB map includes terrain height information color coded from green (low) to white (high). The northern edge of the Tatra is visible on the bottom right. Colored plumes correspond to that fraction of the plumes influencing the respective EM27/SUN (blue = western station Raciborz, red = southern station Pustelnik, gray = plumes not affecting any station). The scene clearly indicates easterly winds. Bottom panel: EM27/SUN measurements of all four instruments. The northern instrument Za Miastem (cyan) and the eastern instrument The Glade (green), are not influenced by any methane from the USCB, and due its upwind location, The Glade serves as background station. Blue (Raciborz) and red (Pustelnik) observations serve as downwind stations. The background colors indicate the time frames used for the inversion method considering the time lag due to travel times between downwind and upwind (The Glade) stations: red for just the southern station Pustelnik, purple for both stations Pustelnik and Raciborz, and blue for just the western station Raciborz.

Western station Raciborz

Under northeast-north wind conditions the western station Raciborz is influenced by methane emitted by shafts from the northern part of the USCB. In this region, the coal extraction depth constantly rose in recent years (exceeding 1000 m in many mines), leading to an increase in methane emissions, although the coal production decreased (Kędzior and Dreger, 2019). Therefore, this part of the USCB is of special interest. Fig. 6.17 shows an overall well fitted `CONTROL` run solution for $\lambda = 0.1$ with a mean bias of $9.2 \times 10^{-7}\,\mathrm{kg\,m^{-2}}$ and a RMSE of $1.2 \times 10^{-5}\,\mathrm{kg\,m^{-2}}$.

The L-curve in Fig. 6.19 suggests a regularization parameter $\lambda = 0.1$. However, the weak L-shape may have various origins: The forward model might be erroneous leading to a flawed solution of the inversion routine. This may be caused by a decaying atmospheric boundary layer towards the end of the measurement day. The measured boundary layer height of the closest wind lidar and for that particular day is depicted in the upper panel of Figure 5.3. The lidar measurements reveal, that the PBL starts to collapse around 16 UTC. It is conceivable, that the WRF simulations do not resolve the decaying process sufficiently, which could influence the wind simulations and hence, impact the forward model.

The lineup of all contributing shafts and their respective error analysis is pictured in Figure 6.18. The best guess solution estimates $717 \pm 69\,\mathrm{kt\,a^{-1}}$ for the sum of all contributing shafts. This estimate is three times higher than the E-PRTR emission sum for the same shafts ($241.63\,\mathrm{kt\,a^{-1}}$). Atmospheric variability introduced by the ensemble leads to a relative, total emission uncertainty of $\pm 10\,\%$, which is low compared to the other discussed cases. This does not conclusively suggest a consistent ensemble, but could rather be attributed to the regularization strength. The error on the emission estimates caused by the observational noise $\boldsymbol{\varepsilon}$ is $0.21\,\mathrm{kt\,a^{-1}}$.

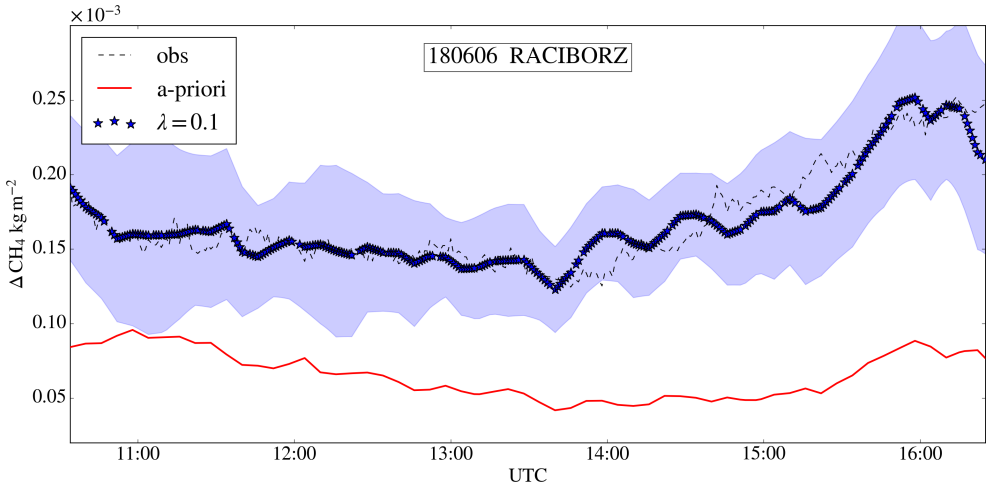

Figure 6.17: Simulated measurements (blue stars) compared to FTS observations (dashed line) for the western station Raciborz for 6 June 2018. The red line illustrates the enhancements, which are caused by the a-priori emissions. The blue background represents the combined standard deviation of the model ensemble and the measurement noise.

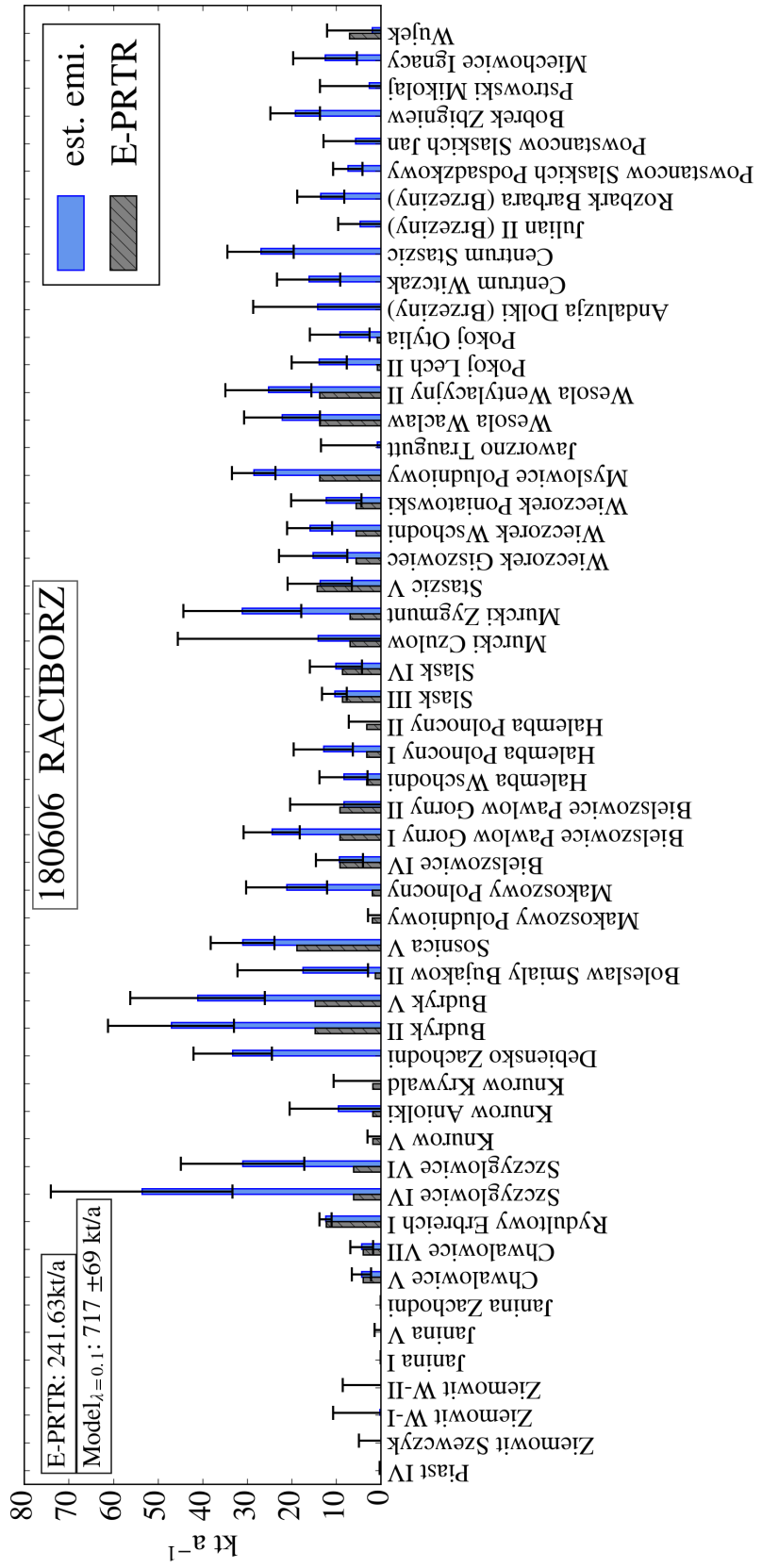

Figure 6.18: Estimated emission rates and their respective error bars containing the ensemble uncertainty and the measurement noise for the western station Raciborz on 6 June 2018.

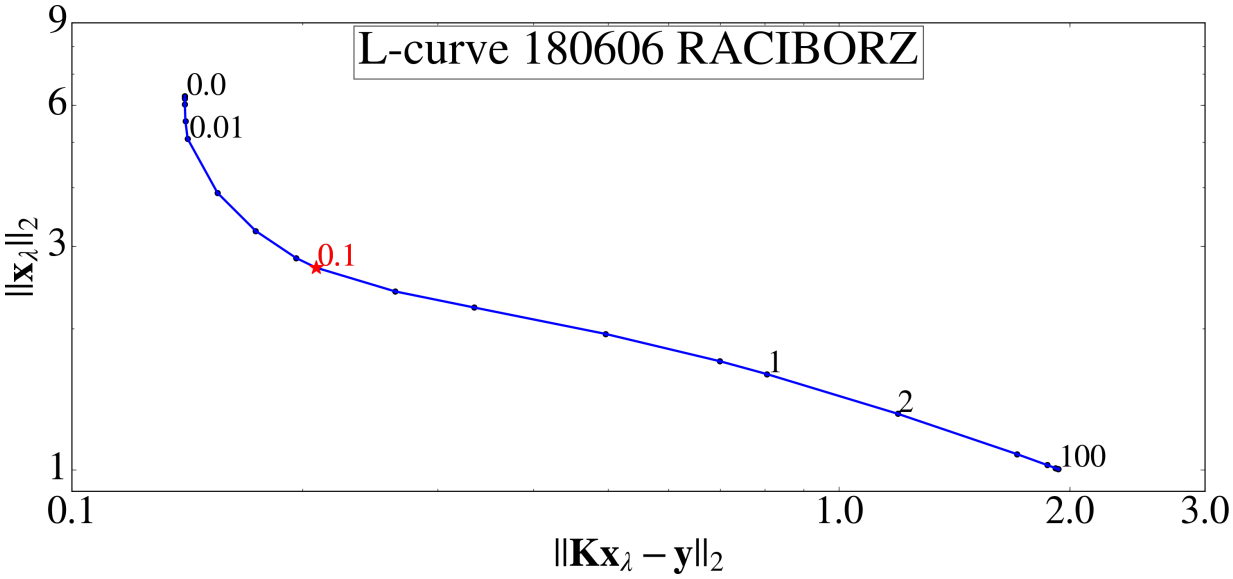

Figure 6.19: The L-curve does not show a distinct L-shape. The regularization parameter $\lambda = 0.1$ (red star) is chosen. However, the generally smooth transitions between the residuals $\|\mathbf{K}\mathbf{x} - \mathbf{y}\|_2$ cannot be identified unambiguously as L-shape and in principle allow for other λ.

Southern station Pustelnik

The southern station Pustelnik is influenced by methane originating from the southeastern part of the USCB. Fig. 6.20 shows the simulated methane enhancements for $\lambda = 0.3$, compared to the observations. The southeastern part of the USCB influencing the scene contains 13 shafts under these wind conditions. A reduced number of shafts limits the possibilities for the inversion routine to find suitable solutions. The residuals of the best guess `CONTROL` run with $\lambda = 0.3$ (according to the L-curve in Fig. 6.21) exhibit a mean bias of $3.9 \times 10^{-6}\,\mathrm{kg\,m^{-2}}$ and a RMSE of $1.4 \times 10^{-5}\,\mathrm{kg\,m^{-2}}$.

There are three shafts (Piast IV, Janina V, and Brzeszcze IV) which are of special interest for this scene. Due to small wind direction changes in the model around 12 UTC, Piast IV and Janina V, which are on the northern edge of the contributing shaft group, start to influence the simulated measurements. Around 13 UTC the shafts Piast IV and Brzeszcze IV stop to influence the scene. The fitting routine fails to find a suitable solution for all time steps, which is comprehensible, as from the model perspective the shafts effectively are turned on and off in a short period of time. Most likely due to an erroneous forward model, the period between 12 UTC and 13 UTC shows a distinct peak which is not observed by the FTS. Once this period is excluded from the analysis, the L-curve shape significantly improves. To this end, this period is not considered by the inversion procedure.

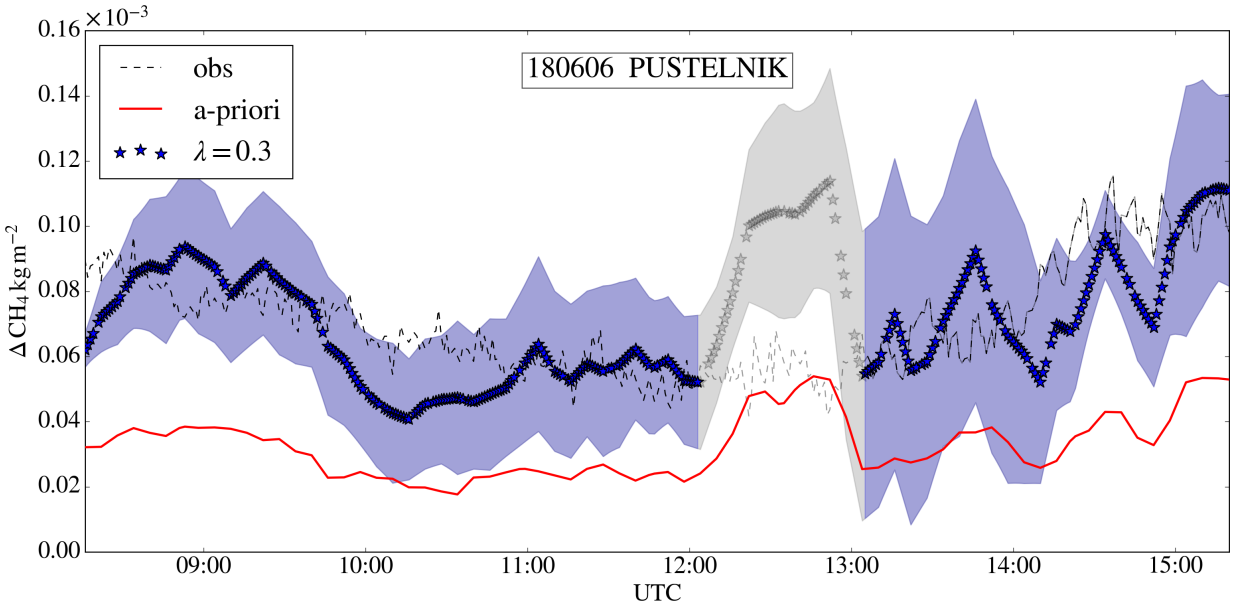

Figure 6.20: Simulated measurements (blue stars) compared to FTS observations (dashed line) for the southern station Pustelnik for 6 June 2018. The red line illustrates the enhancements, which are caused by the a-priori emissions. Most striking is a simulated enhancement peak between 12 and 13 UTC which is not represented by the observations. The peak is most likely connected to an erroneous forward model, and hence, excluded from the analysis (grayed-out period). The blue background represents the combined standard deviation of the model ensemble and the measurement noise.

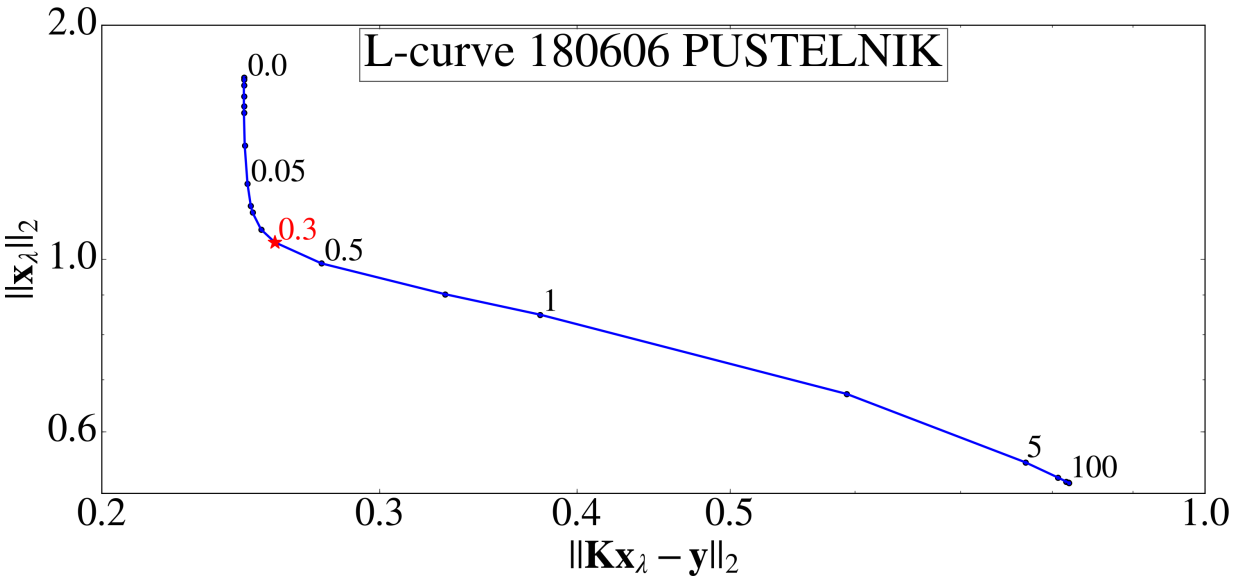

Figure 6.21: The L-curve does not show a clear L-shape. The regularization parameter $\lambda = 0.3$ (red star) is chosen.

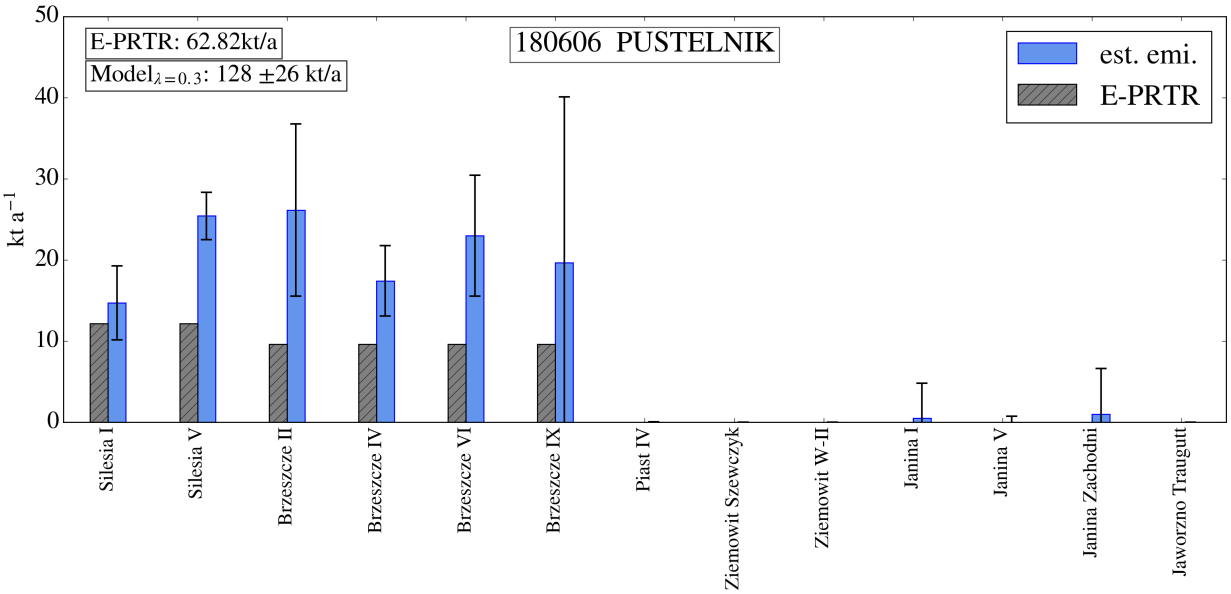

Figure 6.22: Estimated emission rates and their respective error bars containing the ensemble uncertainty and the measurement noise for the southern station Pustelnik on 6 June 2018. In general only six shafts contribute to the total regional emission sum.

The best guess emission estimate sum is dominated by the Silesia and Brzeszcze mine (Fig. 6.22). All other shafts generally influence the simulation in other ensemble runs with e.g. slightly rotated wind direction and their influence is regularized towards zero by the inversion method. It is apparent, that most estimates indicate higher emissions than the E-PRTR inventory suggests. The sum of the simulated emissions is with $128 \pm 26\,\mathrm{kt\,a^{-1}}$ roughly twice the sum of the same shafts according to E-PRTR ($62.82\,\mathrm{kt\,a^{-1}}$). Atmospheric variability introduced by the ensemble leads to a relative, total emission uncertainty of $\pm 20\,\%$. The error on the emission estimates caused by the observational noise $\boldsymbol{\varepsilon}$ is $0.36\,\mathrm{kt\,a^{-1}}$.

6.5.3 7 June 2018

On 7 June 2018 the wind was blowing from generally eastern directions (left panel in Figure 6.23). Similar to the situation on 28 May 2018, all shafts north of $50.2\,^\circ$ do not influence the simulated measurements. This leaves the northern part of the USCB unobserved for the FTS instruments. Due to clouds interrupting the measurements in the morning at the eastern station The Glade, the theoretically available period for the inversion shortens to roughly 3 h for the southern station Pustelnik, and to roughly 1.3 h for the western station Raciborz. The simulated travel time for methane is about 2 h for the southern station and about 4.6 h for the western station.

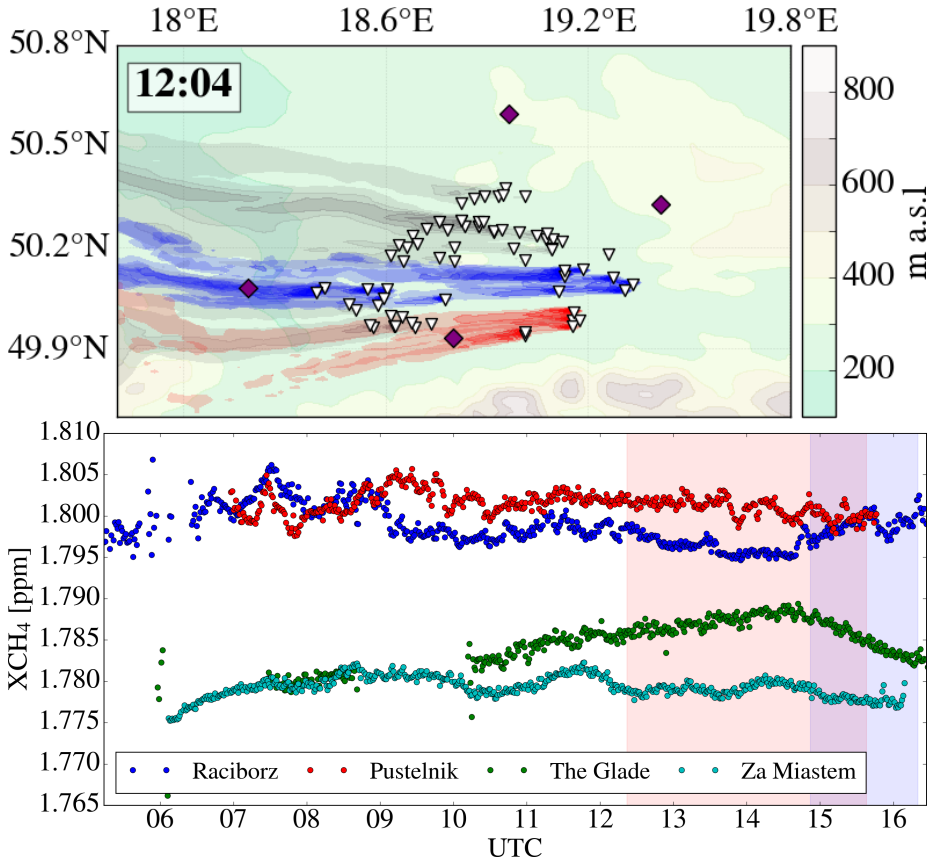

Figure 6.23: Top panel: FLEXPART simulation around noon on 07 June 2018 of the emitted methane and its dispersion through the USCB and above the four stationary EM27/SUN (purple diamonds). Coal mine ventilation shafts are depicted as white triangles. The USCB map includes terrain height information color coded from green (low) to white (high). The northern edge of the Tatra is visible on the bottom right. Colored plumes correspond to that fraction of the plumes influencing the respective EM27/SUN (blue = western station Raciborz, red = southern station Pustelnik, gray = plumes not affecting any station). The scene clearly indicates easterly winds. Bottom panel: EM27/SUN measurements of all four instruments. The northern instrument Za Miastem (cyan) and the eastern instrument The Glade (green), are not influenced by any methane from the USCB, and due to its upwind location, The Glade serves as background station. Blue (Raciborz) and red (Pustelnik) observations serve as downwind stations. The background colors indicate the time frames used for the inversion method considering the time lag due to travel times between downwind and upwind (The Glade) stations: red for just the southern station Pustelnik, purple for both stations Pustelnik and Raciborz, and blue for just the western station Raciborz.

Western station Raciborz

40 shafts contribute to the plume reaching the western station Raciborz. Fig. 6.24 shows an overall well fitted best guess solution for $\lambda = 0.02$ with a mean bias of $1.0 \times 10^{-7}\,\mathrm{kg\,m^{-2}}$

and a RMSE of $7.1 \times 10^{-6}\,\mathrm{kg\,m^{-2}}$. The L-curve in Figure 6.25 shows a distinct L-shape and indicates a favorable regularization parameter of $\lambda = 0.02$.

The summed shaft-wise estimates (Fig. 6.26) amount to $534 \pm 67\mathrm{kt\,a^{-1}}$ which is roughly two times higher than the E-PRTR emission sum for the same shafts ($262.41\mathrm{kt\,a^{-1}}$). Atmospheric variability introduced by the ensemble leads to a relative, total emission uncertainty of $\pm 13\,\%$. The error on the emission estimates caused by the observational noise $\boldsymbol{\varepsilon}$ is $0.084\,\mathrm{kt\,a^{-1}}$.

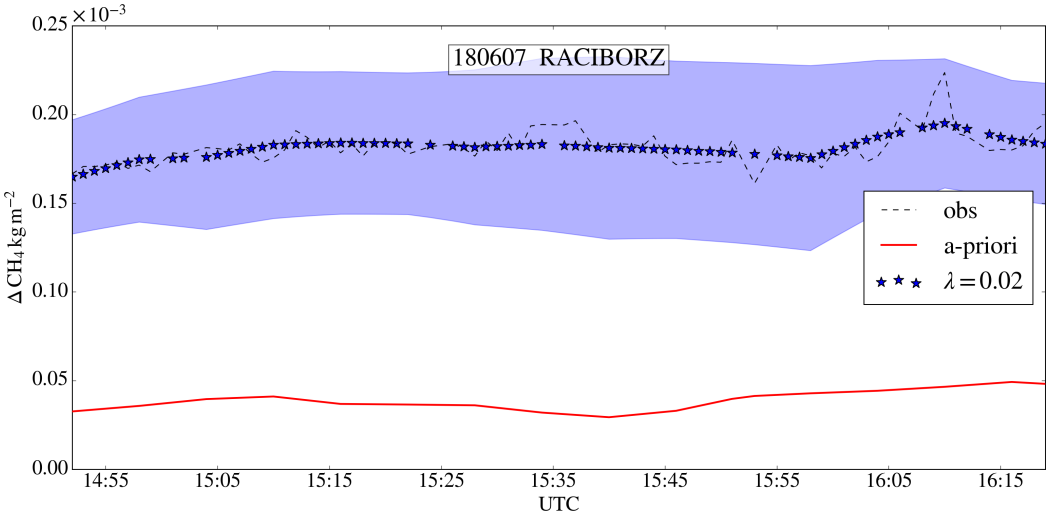

Figure 6.24: Simulated measurements (blue stars) compared to FTS observations (dashed line) for the western station Raciborz for 7 June 2018. The red line illustrates the enhancements, which are caused by the a-priori emissions. The blue background represents the combined standard deviation of the model ensemble and the measurement noise.

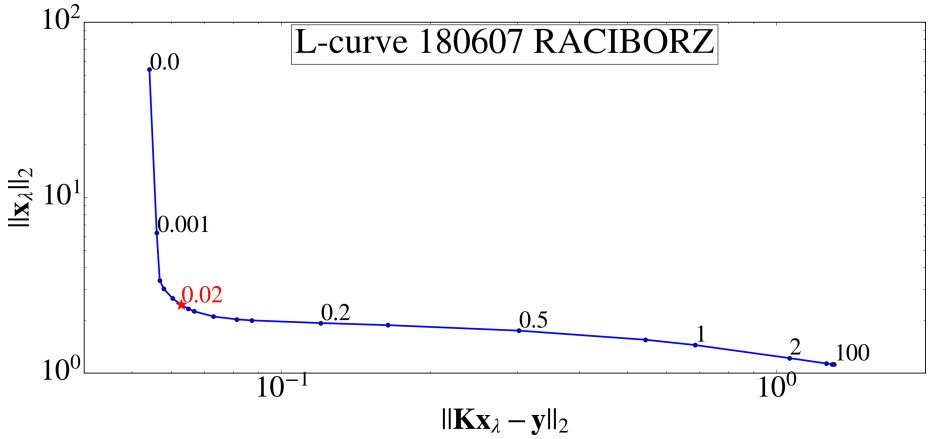

Figure 6.25: The L-curve shows a clear L-shape. The regularization parameter $\lambda = 0.02$ (red star) is chosen.

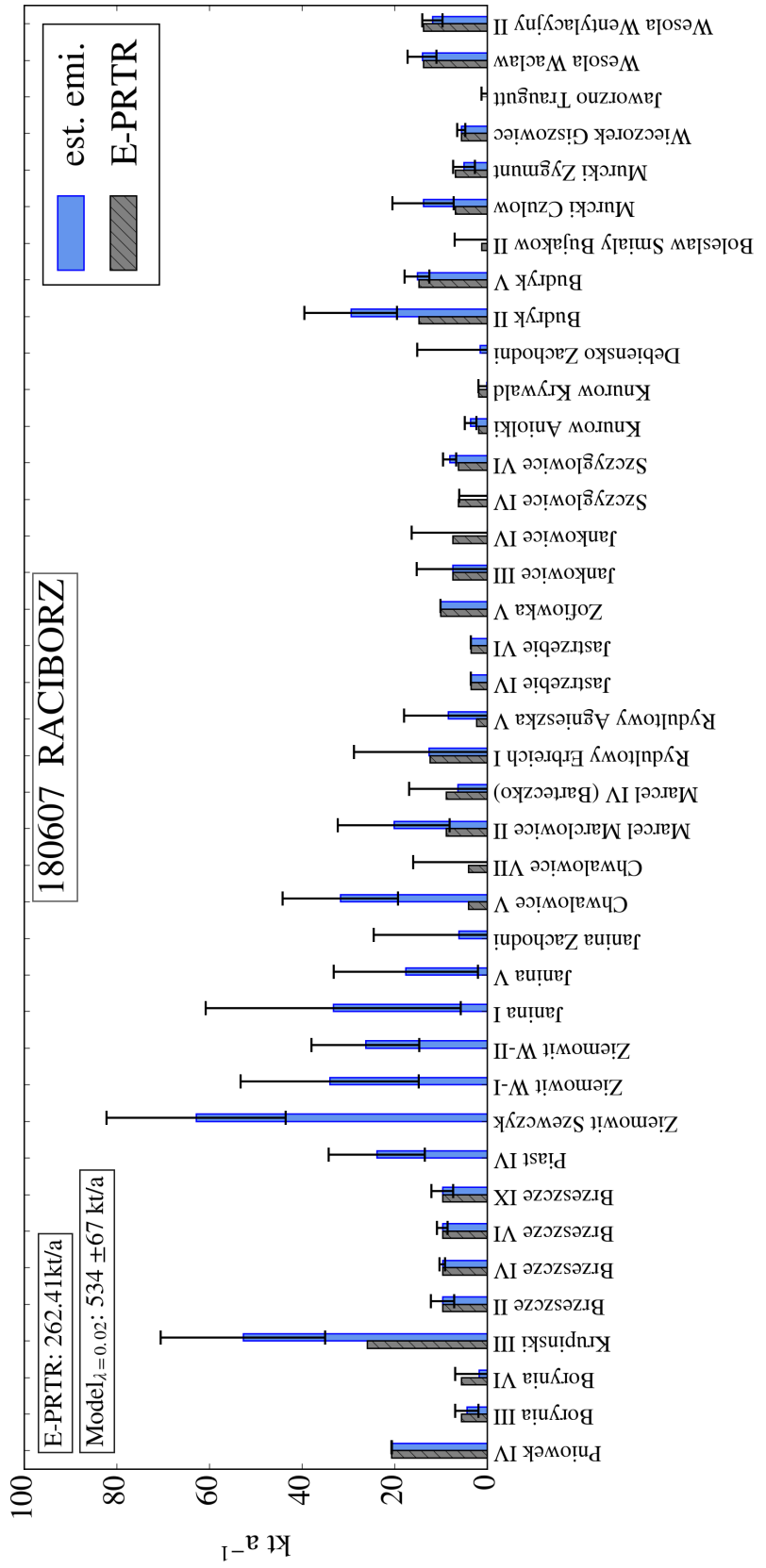

Figure 6.26: Estimated emission rates and their respective error bars containing the ensemble uncertainty and the measurement noise for the western station Raciborz on 7 June 2018.

Southern station Pustelnik

Six shafts are considered by the simulations for the southern instrument Pustelnik. The fitting routine cannot resolve the first hour of the observed enhancements, indicating errors of the forward model (Figure 6.27). This period is excluded from the fitting routine, since it significantly improves the L-shape of the L-curve. The residuals between simulations and observations exhibit a mean bias of $5.1 \times 10^{-7}\,\mathrm{kg\,m^{-2}}$ and a RMSE of $8.5 \times 10^{-6}\,\mathrm{kg\,m^{-2}}$. The regularization parameter is chosen according to the L-curve in Figure 6.28 as $\lambda = 0.1$.

The fitting procedure almost evenly distributes the emission estimates over six shafts to fit the observations (Figure 6.29). The best guess solution estimates $90 \pm 16\,\mathrm{kt\,a^{-1}}$ for the sum of all contributing shafts. This estimate is 1.4 times higher than the E-PRTR emission sum for the same shafts ($62.82\,\mathrm{kt\,a^{-1}}$). Atmospheric variability introduced by the ensemble leads to a relative, total emission uncertainty of $\pm 18\,\%$. The error on the emission estimates caused by the observational noise $\boldsymbol{\varepsilon}$ is $0.25\,\mathrm{kt\,a^{-1}}$.

The results of the regional study are summarized in Table 6.2. Atmospheric variability introduced by the model ensemble leads to errors between 10 % and 32 %. In general, the inversions including more shafts (western station Raciborz) and therefore have more possibilities to find suitable solutions show lower mean bias and RMSE values than the cases only involving six to thirteen shafts (southern station Pustelnik). This indicates, that

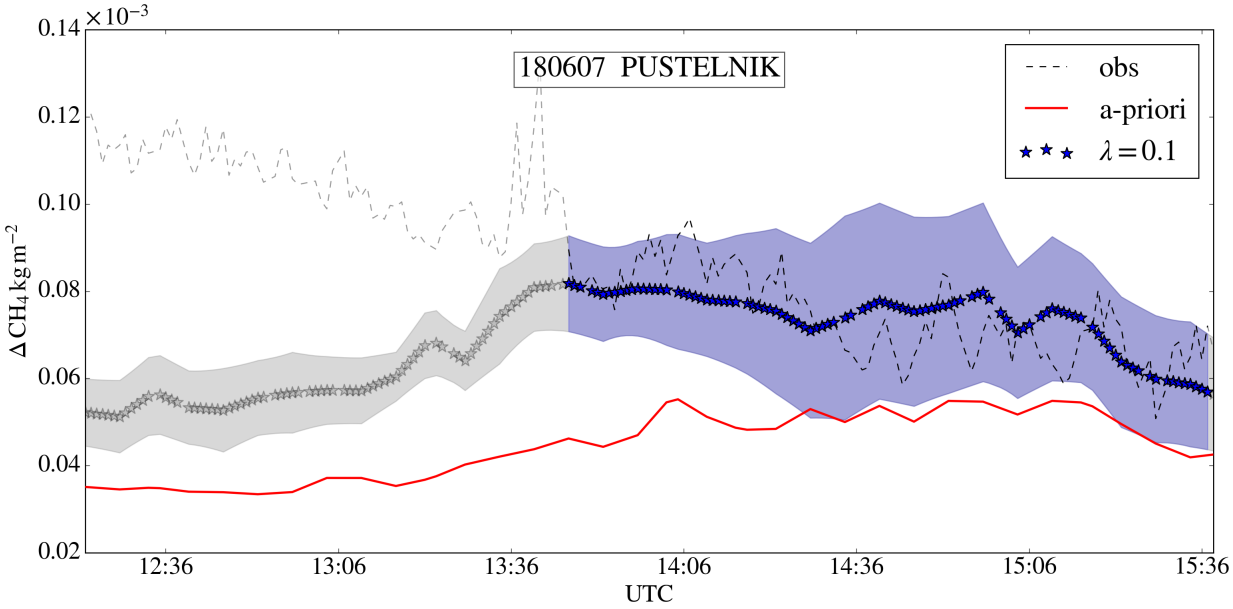

Figure 6.27: Simulated measurements (blue stars) compared to FTS observations (dashed line) for the southern station Pustelnik for 7 June 2018. The red line illustrates the enhancements, which are caused by the a-priori emissions. Most likely due to forward model uncertainties, the first hour of the observations is not simulated correctly leading to the exclusion of this period (grayed-out). The blue background represents the combined standard deviation of the model ensemble and the measurement noise.

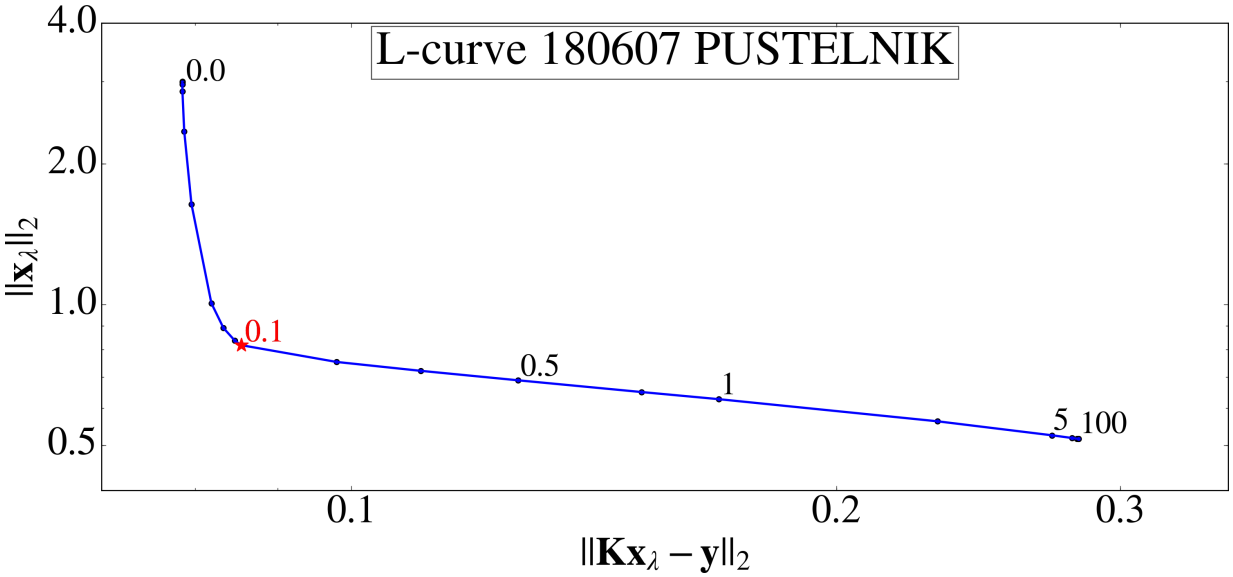

Figure 6.28: The L-curve shows a clear L-shape. The regularization parameter $\lambda = 0.1$ (red star) is chosen.

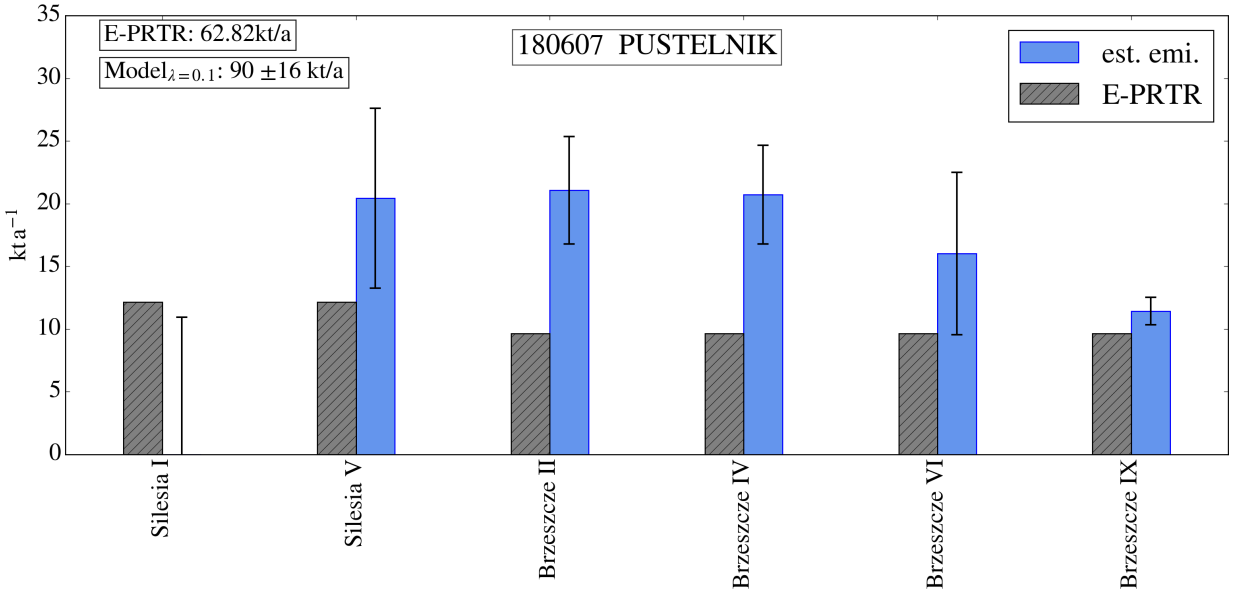

Figure 6.29: Estimated emission rates and their respective error bars containing the ensemble uncertainty and the measurement noise for the southern station Pustelnik on 7 June 2018.

either the model does not resolve the atmospheric condition which has higher influence on smaller scales or that not every major source is represented in the model. The errors due to observational noise are generally two to three orders of magnitude smaller than the errors introduced by atmospheric variability. The emission sum for the case study

on the southern station Pustelnik on 28 May 2018 matches the E-PRTR inventory data within its error range. The five other discussed case studies suggest 1.4 to 3 times higher emissions than reported by the E-PRTR. However, atmospheric and mining process related variability acerbate the comparison between snap-shot observations performed on single days and reported annual averages.

Date	Station	Estimated emissions ($kt\,a^{-1}$)	Combined σ		E-PRTR 2014	Control run residuals ($kgm^{-2} \times 10^{-6}$)		Observational error ε
			($kt\,a^{-1}$)	%	($kt\,a^{-1}$)	BIAS	RMSE	($kt\,a^{-1}$)
28 May	Rac. (West)	**846**	**133**	16	377.25	0.22	7.1	0.39
	Pus. (South)	**76**	**24**	32	62.82	0.38	9.8	0.54
06 June	Rac. (West)	**717**	**69**	10	241.63	9.2	11.7	0.21
	Pus. (South)	**128**	**26**	20	62.82	3.9	14.2	0.36
07 June	Rac. (West)	**534**	**67**	13	262.41	0.1	7.1	0.08
	Pus. (South)	**90**	**16**	18	62.82	0.51	8.4	0.25

Table 6.2: Overview of all case studies regarding the regional emission estimation including respective emission sums and their standard deviation (bold numbers). Mean bias and RMSE of the `CONTROL` run residuals refer to the regularized solution. The error due to observational uncertainties is listed in the last column.

It is apparent from Figures 6.15, 6.22, and 6.29, that the same two mines are observed during the three case studies of the southern station Pustelnik. Due to generally easterly wind conditions, the southern FTS measured methane emitted by the Silesia mine (two shafts) and the Brzeszcze mine (four shafts). A shaft-wise comparison of the estimates might be ambiguous, since some of the shafts are located in line parallel to the wind direction. However, the total emission estimates for all six shafts ($76 \pm 24 kt\,a^{-1}$ for 28 May, $128 \pm 26 kt\,a^{-1}$ for 6 June, and $90 \pm 16 kt\,a^{-1}$ for 7 June, see Table 6.2) can be compared and exhibit a general day-by-day variability of roughly $52\,kt\,a^{-1}$, which by far exceeds the uncertainties introduced by atmospheric variability. This indicates, that on these three days, the mining ventilation variability in the USCB is observed.

Chapter 7

Discussion and outlook

This work describes ground-based FTS remote sensing of XCH_4 enhancements in the plumes of hard coal mining ventilation shafts with the purpose to estimate the underlying emissions. Two measurement campaigns are carried out in the USCB. The first campaign served as a pre-survey and led to improvements of the instrumentation and a better understanding of the emission situation in the target region. The second campaign splits into two parts: 1) mobile FTS observations of plumes emitted by single shafts or group of shafts with consecutive emission estimation with a mass balance approach published by Luther et al. (2019). 2) a model based approach involving a stationary FTS network. The second approach uses WRF simulations with 3D wind lidar data assimilation which feeds into a Lagrangian particle dispersion model (FLEXPART) and allows for regional scale analysis. The resulting XCH_4 simulations are least-squares fitted towards the observations under consideration of a Phillips-Tikhonov regularized approach with E-PRTR emission inventory data as a-priori. In addition, an ensemble with slightly altered atmospheric key parameters (wind speed, wind direction, PBL height) represents atmospheric variability and introduces an error margin.

The error analysis of the mobile FTS approach concludes with an error range between 15 % and 30 %, considering combined errors related to the FTS measurements and vertical, horizontal, and temporal averaging of wind speed and wind direction as observed by three co-deployed 3D wind lidars. The emission estimates for four out of five transects generally agree with the E-PRTR inventory data, although snapshot-like measurements are not representative of annual average inventory data, in particular under consideration of a highly variable atmosphere and mining ventilation process.

The stationary network approach generally suggests higher emission estimates than the related E-PRTR data, although other studies (Luther et al., 2019; Kostinek et al., 2020; Fiehn et al., 2020) show a principle consensus of their estimates and the E-PRTR inventory. However, one out of six case studies agree with the E-PRTR inventory within the error range. The other five cases suggest 1.4 to 3 times higher emissions than reported by the E-PRTR. The errors introduced by the model ensemble, representing atmospheric variability, range between 10% and 32% for the regularized least squares fit. The regularization parameters are chosen via the L-curve interpretation.

When estimating greenhouse gas emissions, it is important to sustain the results with a

profound error analysis. The calculation and propagation of errors caused by e.g. the measurement noise or by modeling of the atmospheric transport and dispersion by means of an ensemble introducing artificial uncertainties representing atmospheric variability, occupies a major part of this work. This work presents two emission estimation methods aiming at two different scales. Each presented method has different error key aspects, however, the measurement uncertainty is in general much smaller than factors regarding atmospheric variability.

Measurement errors are negligibly small compared to wind (or atmospheric variability) induced errors. The dispersion of emitted methane inside the PBL is a highly variable process which may change from eddy to eddy and measurement to measurement. The tools provided in the course of this thesis address the atmospheric variability on two different scales, with two different approaches providing principle measurement and modeling strategies to confine and quantify coal mine methane emissions.

Once the emissions are estimated, under consideration of all discussed uncertainties, the final emission estimates still need to be put in perspective to, e.g. results of other measurement approaches (top down) and inventory data (bottom up). Other approaches, e.g. airborne in-situ measurements combined with Lagrangian particle dispersion modeling (Kostinek et al., 2020) find a general accordance of their emission estimates and the E-PRTR ($466\,\mathrm{kt\,a^{-1}}$) inventory for single downwind flights crossing the entire plume leaving the USCB. Similar results are presented by Fiehn et al. (2020), but for an airborne in-situ mass balance approach. An airborne passive imager concentrating on single clusters of shafts inside the USCB using the cross-sectional flux method, found emission estimates in the range of roughly 30% lower to about 50% higher than the E-PRTR emissions (Krautwurst et al., 2021). The ground-based mobile FTS observations presented in the course of this thesis (Chapter 5) and published in Luther et al. (2019) suggest a principle accordance of single facility estimates of the E-PRTR inventory and the observations. The model approach discussed in Chapter 6 generally estimates 1.4 to 3 times higher emissions than reported by the E-PRTR. These results represent the whole spectrum for reported USCB emissions which range between $344\,\mathrm{kt\,a^{-1}}$ (EUROSTAT, 2020b) (which is related to the whole of Poland) and $720\,\mathrm{kt\,a^{-1}}$ (EDGAR v4.3.2).

The transport of methane plumes through the USCB is a highly variable process, although the terrain is generally flat and the wind direction did not change significantly during the discussed case studies. In addition, the mining process is a generally unknown variable dependent on the present situation in the mines. The methane concentration inside the mines is monitored, to quickly react and adapt the ventilation to ensure safety for the workers. Thus, the methane content in the exhaust air may vary within minutes. However, all comparisons between inventory data and observed emissions in this work represent annual averages, as inventory data is generally reported annually. Comparing annual mean values with up-scaled observations based on single transects or hour-long measurements is expected to show deviations and only long-term measurements could build the basis for reliable comparisons.

Methane sources other than coal mining are not discussed in this work. According to the E-PRTR, the second largest methane source in Poland is waste management including

landfills which amounts to roughly 17 kt a^{-1} with only a few landfills located mostly in the north-east of the USCB. Livestock methane may influence the observations on a very local scale, however, total livestock methane emissions in the USCB are negligibly small compared to coal mining methane emission.

In the following, the two methods presented in this work are analyzed regarding strengths and possible improvements.

Facility scale – mobile FTS observations

Traversing the plume and combining the enhancements with wind information to a typical mass balance approach is a relatively inexpensive way to flexibly estimate emissions on facility scales. As discussed in Chapter 5, this method only requires one value for wind speed and wind direction for each available enhancement sample. On one hand, this can be provided relatively simple by just measuring these variables together with the methane total column information. On the other hand, these variables represent the whole boundary layer which is certainly a rough approximation. This method is also in particular prone to large errors under low wind speed conditions ($< 2\,\mathrm{m\,s^{-1}}$), because relative wind speed errors directly translate into relative emission estimation errors. Integrating direct, local wind measurements may reduce wind related errors. Finding a way to include the wind profile information other than averaging over the PBL might also improve the estimation. On the fly or near real time total column estimates would further accelerate the plume detection, which is only feasible with fast and accurate sun tracking allowing for the vehicle to drive while measuring. Limited by the range of the time consuming stop-and-go pattern and the public road dependency, the method is restricted to single facilities or groups of shafts with a general plume width of roughly 10 km.

The errors induced by wind speed and direction changes between the first and last measurement are only roughly estimated and can lead to wrong interpretations if the wind conditions are too variable during the measurement period. Inflow from other sources into the favored scene may also be wrongly interpreted and need to be regarded via background correction or by dismissing the respective observations. Direct sun measurements make this method dependent on clear sky conditions. Nevertheless, this method may be a possibility to quickly locate e.g. leakages and estimate the underlying emissions. It is further conceivable that this method is used to validate airborne or space missions regarding the advantage of high accuracy and precision due to direct-sun observations and the flexibility of the moving platform.

Regional scale – the stationary network

By means of WRF-driven FLEXPART simulations and a regularized least squares fit between methane observations and simulated enhancements, the emissions of different regions inside the USCB are estimated. An ensemble of model runs with slightly altered meteorological conditions, represents atmospheric variability. Wind-lidar profiles are assimilated into the WRF model. The assimilation process is based on several adjusting screws, e.g.

the radius or the strength of influence of the assimilated input. These properties are completely inherited from Kostinek et al. (2020), as the underlying WRF configuration and the region and time frame of interest are the same. However, Kostinek et al. (2020) validated the assimilation performance with airborne in-situ wind measurements which are observed a few tens of kilometers downwind of the wind lidar measurements. An in-depth analysis of the assimilation process and its reliability on the local scale might improve the simulated wind field. The RMSE for observed and simulated wind direction for all situations used for the emission estimation is 26 °. Wind direction changes as small as 5 ° can lead to significant differences between single ensemble members. Such small wind direction changes determine, whether the plume will affect the simulated (and of course the real) measurements, or not. A large spread of the model ensemble will transition into a large error range for the observed case.

Erroneous forward modeling eventually leads to periods which cannot adequately reproduce the observations. Such periods are diagnosed via changes in the L-curve shape when omitting the respective period. If the L-curve shape significantly improves, the period is excluded from the inversion routine.

In general, the best guess emission estimates based on the FTS network are higher, than the E-PRTR suggestions. Within the errors introduced by the ensemble, one of six examined cases generally match with the E-PRTR estimates. The other five case studies imply 1.4 to 3 times higher emissions.

Similar wind conditions on the three discussed days, led to the southern FTS measurements being influenced by methane emitted by the same group of shafts. The day-by-day variability ($52\,\mathrm{kt\,a^{-1}}$) of the emission estimates suggests a strong variation in the total ventilated methane source for this group, exceeding atmospheric variability introduced by the model ensemble ($16\,\mathrm{kt\,a^{-1}}$ to $26\,\mathrm{kt\,a^{-1}}$). This indicates, that the actual day-by-day variability of the mining ventilation process has been observed.

Not only wind direction uncertainties need to be considered, but also wind speed variability. Uncertainties of the modeled wind speed cause the Lagrangian background to be subtracted from the wrong measurement increment, leading to errors in the enhancement calculations. However, the Lagrangian shift is necessary to account for the airmass travel times ranging between 1.5 h and 4.3 h.

It is also conceivable to select and concentrate on smaller groups of shafts. However, it is not possible to reliably estimate single shaft emissions within a group of shafts, e.g. considering multiple shafts located in line parallel to the wind direction. The Lagrangian background estimation does not consider changing wind speeds during the observed periods. This could be addressed in future studies.

Atmospheric variability is the great unknown and needs to be considered by a profound error approximation. For both presented methods, the wind information contains the biggest uncertainties. The mobile approach mostly suffers from wind speed uncertainties, whereas the model based approach mostly suffers from wind direction uncertainties. Within the respective error ranges, both methods find reasonable methane emission estimates for facilities, sub-regions and regions for an European coal mining hot-spot, the USCB. Both measurement principles makes it possible to monitor emissions of comparable sized facilities

and regions or cities, if the cloud and wind situation allows for it.

In order to validate emission declarations within the UNFCCC, a mix of different greenhouse gas measurement and quantification methods is required. Ground-based, direct sunlight remote sensing in combination with inversion methods as presented in the course of this thesis may help with monitoring regions or facilities, or to detect leakages. Even after coal production in the USCB, it could still be of interest to monitor this region.

References

Alvarez, R. A., Zavala-Araiza, D., Lyon, D. R., Allen, D. T., Barkley, Z. R., Brandt, A. R., Davis, K. J., Herndon, S. C., Jacob, D. J., Karion, A., Kort, E. A., Lamb, B. K., Lauvaux, T., Maasakkers, J. D., Marchese, A. J., Omara, M., Pacala, S. W., Peischl, J., Robinson, A. L., Shepson, P. B., Sweeney, C., Townsend-Small, A., Wofsy, S. C., and Hamburg, S. P.: Assessment of methane emissions from the U.S. oil and gas supply chain, Science, 361, 186–188, https://doi.org/10.1126/science.aar7204, URL https://science.sciencemag.org/content/361/6398/186, 2018.

Amediek, A., Ehret, G., Fix, A., Wirth, M., Büdenbender, C., Quatrevalet, M., Kiemle, C., and Gerbig, C.: CHARM-F - a new airborne integrated-path differential-absorption lidar for carbon dioxide and methane observations: measurement performance and quantification of strong point source emissions, Appl. Opt., 56, 5182–5197, https://doi.org/10.1364/AO.56.005182, 2017.

Andersen, T., Scheeren, B., Peters, W., and Chen, H.: A UAV-based active AirCore system for measurements of greenhouse gases, Atmospheric Measurement Techniques, 11, 2683–2699, https://doi.org/10.5194/amt-11-2683-2018, 2018.

Antoszczyszyn, T. and Michalska, A.: The potential risk of environmental contamination by mercury contained in Polish coal mining waste, Journal of Sustainable Mining, 15, 191–196, https://doi.org/10.1016/j.jsm.2017.04.002, 2016.

Archer, D.: Fate of fossil fuel CO2 in geologic time, Journal of Geophysical Research: Oceans, 110, https://doi.org/10.1029/2004JC002625, URL https://agupubs.onlinelibrary.wiley.com/doi/abs/10.1029/2004JC002625, 2005.

Arrhenius, S.: XXXI. On the influence of carbonic acid in the air upon the temperature of the ground, The London, Edinburgh, and Dublin Philosophical Magazine and Journal of Science, 41, 237–276, https://doi.org/10.1080/14786449608620846, 1896.

BBC: State mourning for Poland miners, URL http://news.bbc.co.uk/2/hi/8264624.stm, accessed: 2020-11-17, 2009.

Beer, R.: Remote sensing by Fourier transform spectrometry, vol. 170, John Wiley & Sons, 1992.

Berman, E. S., Fladeland, M., Liem, J., Kolyer, R., and Gupta, M.: Greenhouse gas analyzer for measurements of carbon dioxide, methane, and water vapor aboard an unmanned aerial vehicle, Sensors and Actuators B: Chemical, 169, 128–135, https://doi.org/10.1016/j.snb.2012.04.036, 2012.

Blaylock, B. K., Horel, J. D., and Crosman, E. T.: Impact of Lake Breezes on Summer Ozone Concentrations in the Salt Lake Valley, Journal of Applied Meteorology and

Climatology, 56, 353–370, https://doi.org/10.1175/JAMC-D-16-0216.1, URL https://doi.org/10.1175/JAMC-D-16-0216.1, 2017.

Borsdorff, T., Hasekamp, O. P., Wassmann, A., and Landgraf, J.: Insights into Tikhonov regularization: application to trace gas column retrieval and the efficient calculation of total column averaging kernels, Atmospheric Measurement Techniques, 7, 523–535, https://doi.org/10.5194/amt-7-523-2014, URL https://amt.copernicus.org/articles/7/523/2014/, 2014.

Bousquet, P., Ciais, P., Miller, J., Dlugokencky, E. J., Hauglustaine, D., Prigent, C., Van der Werf, G., Peylin, P., Brunke, E.-G., Carouge, C., Langenfelds, R., Lathière, J., Papa, F., Ramonet, M., Schmidt, M., Steele, L. P., Tyler, S. C., and White, J.: Contribution of anthropogenic and natural sources to atmospheric methane variability, Nature, 443, 439, 2006.

Bovensmann, H., Burrows, J. P., Buchwitz, M., Frerick, J., Noël, S., Rozanov, V. V., Chance, K. V., and Goede, A. P. H.: SCIAMACHY: Mission Objectives and Measurement Modes, Journal of the Atmospheric Sciences, 56, 127–150, https://doi.org/10.1175/1520-0469(1999)056<0127:SMOAMM>2.0.CO;2, URL https://doi.org/10.1175/1520-0469(1999)056<0127:SMOAMM>2.0.CO;2, 1999.

Brioude, J., Arnold, D., Stohl, A., Cassiani, M., Morton, D., Seibert, P., Angevine, W., Evan, S., Dingwell, A., Fast, J. D., Easter, R. C., Pisso, I., Burkhart, J., and Wotawa, G.: The Lagrangian particle dispersion model FLEXPART-WRF version 3.1, Geoscientific Model Development, 6, 1889–1904, https://doi.org/10.5194/gmd-6-1889-2013, URL https://gmd.copernicus.org/articles/6/1889/2013/, 2013.

Bun, R., Nahorski, Z., Horabik-Pyzel, J., Danylo, O., See, L., Charkovska, N., Topylko, P., Halushchak, M., Lesiv, M., Valakh, M., and Kinakh, V.: Development of a high-resolution spatial inventory of greenhouse gas emissions for Poland from stationary and mobile sources, Mitigation and Adaptation Strategies for Global Change, 24, 853–880, https://doi.org/10.1007/s11027-018-9791-2, URL https://doi.org/10.1007/s11027-018-9791-2, 2019.

Buschmann, M., Deutscher, N. M., Palm, M., Warneke, T., Weinzierl, C., and Notholt, J.: The arctic seasonal cycle of total column CO2 and CH4 from ground-based solar and lunar FTIR absorption spectrometry, Atmospheric Measurement Techniques, 10, 2397–2411, 2017.

Butz, A., Hasekamp, O. P., Frankenberg, C., Vidot, J., and Aben, I.: CH4 retrievals from space-based solar backscatter measurements: Performance evaluation against simulated aerosol and cirrus loaded scenes, Journal of Geophysical Research: Atmospheres, 115, https://doi.org/https://doi.org/10.1029/2010JD014514, URL https://agupubs.onlinelibrary.wiley.com/doi/abs/10.1029/2010JD014514, 2010.

Butz, A., Guerlet, S., Hasekamp, O., Schepers, D., Galli, A., Aben, I., Frankenberg, C., Hartmann, J.-M., Tran, H., Kuze, A., Keppel-Aleks, G., Toon, G., Wunch, D., Wennberg, P., Deutscher, N., Griffith, D., Macatangay, R., Messerschmidt, J., Notholt, J., and Warneke, T.: Toward accurate CO2 and CH4 observations from GOSAT, Geophysical Research Letters, 38, https://doi.org/https://doi.org/10.1029/2011GL047888, URL https://agupubs.onlinelibrary.wiley.com/doi/abs/10.1029/2011GL047888, 2011.

Butz, A., Galli, A., Hasekamp, O., Landgraf, J., Tol, P., and Aben, I.: TROPOMI aboard Sentinel-5 Precursor: Prospective performance of CH4 retrievals for aerosol and cirrus loaded atmospheres, Remote Sensing of Environment, 120, 267–276, https://doi.org/https://doi.org/10.1016/j.rse.2011.05.030, URL https://www.sciencedirect.com/science/article/pii/S003442571200082X, the Sentinel Missions - New Opportunities for Science, 2012.

Butz, A., Dinger, A. S., Bobrowski, N., Kostinek, J., Fieber, L., Fischerkeller, C., Giuffrida, G. B., Hase, F., Klappenbach, F., Kuhn, J., Lübcke, P., Tirpitz, L., and Tu, Q.: Remote sensing of volcanic CO_2, HF, HCl, SO_2, and BrO in the downwind plume of Mt. Etna, Atmos. Meas. Tech., 10, 1–14, https://doi.org/10.5194/amt-10-1-2017, 2017.

Calvetti, D., Morigi, S., Reichel, L., and Sgallari, F.: Tikhonov regularization and the L-curve for large discrete ill-posed problems, Journal of Computational and Applied Mathematics, 123, 423–446, https://doi.org/https://doi.org/10.1016/S0377-0427(00)00414-3, URL https://www.sciencedirect.com/science/article/pii/S0377042700004143, numerical Analysis 2000. Vol. III: Linear Algebra, 2000.

Cambaliza, M. O. L., Shepson, P. B., Caulton, D. R., Stirm, B., Samarov, D., Gurney, K. R., Turnbull, J., Davis, K. J., Possolo, A., Karion, A., Sweeney, C., Moser, B., Hendricks, A., Lauvaux, T., Mays, K., Whetstone, J., Huang, J., Razlivanov, I., Miles, N. L., and Richardson, S. J.: Assessment of uncertainties of an aircraft-based mass balance approach for quantifying urban greenhouse gas emissions, Atmos. Chem. Phys., 14, 9029–9050, https://doi.org/10.5194/acp-14-9029-2014, 2014.

Cambaliza, O. L. M., Shepson, P., Bogner, J., Caulton, R. D., Stirm, B., Sweeney, C., Montzka, A. S., Gurney, K., Spokas, K., Salmon, O., Lavoie, T., Davis, K., Karion, A., Moser, B., and Richardson, S.: Quantification and source apportionment of the methane emission flux from the city of Indianapolis, Elementa Science of the Anthropocene, 3, https://doi.org/10.12952/journal.elementa.000037, 2015.

Chen, J., Viatte, C., Hedelius, J. K., Jones, T., Franklin, J. E., Parker, H., Gottlieb, E. W., Wennberg, P. O., Dubey, M. K., and Wofsy, S. C.: Differential column measurements using compact solar-tracking spectrometers, Atmos. Chem. Phys., 16, 8479–8498, https://doi.org/10.5194/acp-16-8479-2016, 2016.

Chen, J., Dietrich, F., Maazallahi, H., Forstmaier, A., Winkler, D., Hofmann, M. E., Denier van der Gon, H., and Röckmann, T.: Methane emissions from the Munich Oktoberfest., Atmospheric Chemistry & Physics, 20, https://doi.org/10.5194/acp-20-3683-2020, 2020.

Conley, S., Franco, G., Faloona, I., Blake, D. R., Peischl, J., and Ryerson, T. B.: Methane emissions from the 2015 Aliso Canyon blowout in Los Angeles, CA, Science, 351, 1317–1320, https://doi.org/10.1126/science.aaf2348, 2016.

Conley, S., Faloona, I., Mehrotra, S., Suard, M., Lenschow, D. H., Sweeney, C., Herndon, S., Schwietzke, S., Pétron, G., Pifer, J., Kort, E. A., and Schnell, R.: Application of Gauss's theorem to quantify localized surface emissions from airborne measurements of wind and trace gases, Atmospheric Measurement Techniques, 10, 3345–3358, https://doi.org/10.5194/amt-10-3345-2017, URL `https://www.atmos-meas-tech.net/10/3345/2017/`, 2017.

Dahmann, D., Morfeld, P., Monz, C., Noll, B., and Gast, F.: Exposure assessment for nitrogen oxides and carbon monoxide in German hard coal mining, International archives of occupational and environmental health, 82, 1267–1279, https://doi.org/10.1007/s00420-009-0418-5, 2009.

Davis, K. J. and Gerlach, R.: Transition of biogenic coal-to-methane conversion from the laboratory to the field: A review of important parameters and studies, International Journal of Coal Geology, 185, 33–43, https://doi.org/10.1016/j.coal.2017.11.006, 2018.

Davis, S. P., Abrams, M. C., and Brault, J. W.: Fourier transform spectrometry, Elsevier, 2001.

Desbiens, R., Genest, J., Tremblay, P., and Bouchard, J.-P.: Correction of instrument line shape in Fourier transform spectrometry using matrix inversion, Appl. Opt., 45, 5270–5280, https://doi.org/10.1364/AO.45.005270, URL `http://ao.osa.org/abstract.cfm?URI=ao-45-21-5270`, 2006.

Dietrich, F., Chen, J., Voggenreiter, B., Aigner, P., Nachtigall, N., and Reger, B.: MUCCnet: Munich Urban Carbon Column network, Atmospheric Measurement Techniques, 14, 1111–1126, https://doi.org/10.5194/amt-14-1111-2021, URL `https://amt.copernicus.org/articles/14/1111/2021/`, 2021.

Dlugokencky, E.: NOAA/GML methane trends, URL `https://esrl.noaa.gov/gmd/ccgg/trends_ch4/`, accessed: 2020-07-10, 2019.

Dlugokencky, E. J., Nisbet, E. G., Fisher, R., and Lowry, D.: Global atmospheric methane: budget, changes and dangers, Philosophical Transactions of the Royal Society A: Mathematical, Physical and Engineering Sciences, 369, 2058–2072, https://doi.org/10.1098/rsta.2010.0341, URL `https://royalsocietypublishing.org/doi/abs/10.1098/rsta.2010.0341`, 2011.

Dreger, M.: Changes in the methane emissions and hard coal output in the Brzeszcze mine (the Upper Silesian Coal Basin, Poland), Geology, Geophysics and Environment, 46, 159, https://doi.org/10.7494/geol.2020.46.2.159, URL https://journals.agh.edu.pl/geol/article/view/3722, 2020.

E-PRTR 2014: The European Pollutant Release and Transfer Register, URL http://prtr.ec.europa.eu, accessed: 2018-08-13.

ECMWF: ECMWF data, URL https://apps.ecmwf.int/archive-catalogue/, 2018.

Ehret, G., Bousquet, P., Pierangelo, C., Alpers, M., Millet, B., Abshire, J., Bovensmann, H., Burrows, J., Chevallier, F., Ciais, P., and et al.: MERLIN: A French-German Space Lidar Mission Dedicated to Atmospheric Methane, Remote Sensing, 9, 1052, https://doi.org/10.3390/rs9101052, URL http://dx.doi.org/10.3390/rs9101052, 2017.

ESRI: DeLorme World Base Map, URL http://server.arcgisonline.com/ArcGIS/rest/services/Specialty/DeLorme_World_Base_Map/MapServer/export?bbox=465524.673242,223740.873843,484241.251687,238103.141466&bboxSR=2180&imageSR=2180&size=1500,1151&dpi=96&format=png32&f=imageC, 2019.

Etheridge, D. M., Steele, L. P., Francey, R. J., and Langenfelds, R. L.: Atmospheric methane between 1000 A.D. and present: Evidence of anthropogenic emissions and climatic variability, Journal of Geophysical Research: Atmospheres, 103, 15 979–15 993, https://doi.org/10.1029/98JD00923, URL https://agupubs.onlinelibrary.wiley.com/doi/abs/10.1029/98JD00923, 1998.

EUROSTAT: European Energy Statistics 2020, URL https://ec.europa.eu/eurostat/cache/infographs/energy/bloc-2c.html, accessed: 2020-11-10, 2020a.

EUROSTAT: The European Statistical System, URL https://appsso.eurostat.ec.europa.eu/nui/show.do?dataset=env_ac_aibrid_r2&lang=en, accessed: 2020-01-18, 2020b.

Fiehn, A., Kostinek, J., Eckl, M., Klausner, T., Gałkowski, M., Chen, J., Gerbig, C., Röckmann, T., Maazallahi, H., Schmidt, M., Korbeń, P., Nęcki, J., Jagoda, P., Wildmann, N., Mallaun, C., Bun, R., Nickl, A.-L., Jöckel, P., Fix, A., and Roiger, A.: Estimating CH_4, CO_2 and CO emissions from coal mining and industrial activities in the Upper Silesian Coal Basin using an aircraft-based mass balance approach, Atmospheric Chemistry and Physics, 20, 12 675–12 695, https://doi.org/10.5194/acp-20-12675-2020, URL https://acp.copernicus.org/articles/20/12675/2020/, 2020.

Fourier, J.: Mémoire sur les températures du globe terrestre et des espaces planétaires, Mémoires de l'Académie Royale des Sciences de l'Institut de France, 7, 570–604, 1827.

Frankenberg, C., Meirink, J. F., van Weele, M., Platt, U., and Wagner, T.: Assessing Methane Emissions from Global Space-Borne Observations, Science, 308, 1010–1014, https://doi.org/10.1126/science.1106644, URL `https://science.sciencemag.org/content/308/5724/1010`, 2005.

Frey, M., Hase, F., Blumenstock, T., Groß, J., Kiel, M., Mengistu Tsidu, G., Schäfer, K., Sha, M. K., and Orphal, J.: Calibration and instrumental line shape characterization of a set of portable FTIR spectrometers for detecting greenhouse gas emissions, Atmos. Meas. Tech., 8, 3047–3057, https://doi.org/10.5194/amt-8-3047-2015, 2015.

Frey, M., Sha, M. K., Hase, F., Kiel, M., Blumenstock, T., Harig, R., Surawicz, G., Deutscher, N. M., Shiomi, K., Franklin, J. E., Bösch, H., Chen, J., Grutter, M., Ohyama, H., Sun, Y., Butz, A., Mengistu Tsidu, G., Ene, D., Wunch, D., Cao, Z., Garcia, O., Ramonet, M., Vogel, F., and Orphal, J.: Building the COllaborative Carbon Column Observing Network (COCCON): long-term stability and ensemble performance of the EM27/SUN Fourier transform spectrometer, Atmos. Meas. Tech., 12, 1513–1530, https://doi.org/10.5194/amt-12-1513-2019, 2019.

Frey, M. M., Hase, F., Blumenstock, T., Dubravica, D., Groß, J., Göttsche, F., Handjaba, M., Amadhila, P., Mushi, R., Morino, I., Shiomi, K., Sha, M. K., de Mazière, M., and Pollard, D. F.: Long-term column-averaged greenhouse gas observations using a COCCON spectrometer at the high surface albedo site Gobabeb, Namibia, Atmospheric Measurement Techniques Discussions, 2021, 1–42, https://doi.org/10.5194/amt-2020-444, URL `https://amt.copernicus.org/preprints/amt-2020-444/`, 2021.

Gerilowski, K., Tretner, A., Krings, T., Buchwitz, M., Bertagnolio, P. P., Belemezov, F., Erzinger, J., Burrows, J. P., and Bovensmann, H.: MAMAP – a new spectrometer system for column-averaged methane and carbon dioxide observations from aircraft: instrument description and performance analysis, Atmos. Meas. Tech., 4, 215–243, https://doi.org/10.5194/amt-4-215-2011, 2011.

Gisi, M., Hase, F., Dohe, S., and Blumenstock, T.: Camtracker: a new camera controlled high precision solar tracker system for FTIR-spectrometers, Atmos. Meas. Tech., 4, 47–54, https://doi.org/10.5194/amt-4-47-2011, 2011.

Gisi, M., Hase, F., Dohe, S., Blumenstock, T., Simon, A., and Keens, A.: XCO_2-measurements with a tabletop FTS using solar absorption spectroscopy, Atmos. Meas. Tech., 5, 2969–2980, https://doi.org/10.5194/amt-5-2969-2012, 2012.

Golub, G. H. and Von Matt, U.: Tikhonov regularization for large scale problems, Citeseer, 1997.

Granier, C., Darras, S., Denier Van Der Gon, H., Jana, d., Elguindi, N., Bo, g., Michael, g., Marc, g., Jalkanen, J.-P., Kuenen, J., Liousse, C., Quack, B., Simpson, D., and Sindelarova, K.: The Copernicus Atmosphere Monitoring Service global and regional

emissions (April 2019 version), Research report, Copernicus Atmosphere Monitoring Service, https://doi.org/10.24380/d0bn-kx16, URL https://hal.archives-ouvertes.fr/hal-02322431, 2019.

Hansen, P. C.: Analysis of Discrete Ill-Posed Problems by Means of the L-Curve, SIAM Review, 34, 561–580, https://doi.org/10.1137/1034115, URL https://doi.org/10.1137/1034115, 1992.

Hansen, P. C.: The L-curve and its use in the numerical treatment of inverse problems, 1999.

Hansen, P. C. and O'Leary, D. P.: The Use of the L-Curve in the Regularization of Discrete Ill-Posed Problems, SIAM Journal on Scientific Computing, 14, 1487–1503, https://doi.org/10.1137/0914086, URL https://doi.org/10.1137/0914086, 1993.

Hase, F.: Inversion von Spurengasprofilen aus hochaufgelösten bodengebundenen FTIR-Messungen in Absorption, Ph.D. thesis, 2000.

Hase, F., Hannigan, J., Coffey, M., Goldman, A., Höpfner, M., Jones, N., Rinsland, C., and Wood, S.: Intercomparison of retrieval codes used for the analysis of high-resolution, ground-based FTIR measurements, J. Quant. Spectrosc. Radiat. Transfer, 87, 25 – 52, https://doi.org/10.1016/j.jqsrt.2003.12.008, 2004.

Hase, F., Frey, M., Blumenstock, T., Groß, J., Kiel, M., Kohlhepp, R., Mengistu Tsidu, G., Schäfer, K., Sha, M. K., and Orphal, J.: Application of portable FTIR spectrometers for detecting greenhouse gas emissions of the major city Berlin, Atmos. Meas. Tech., 8, 3059–3068, https://doi.org/10.5194/amt-8-3059-2015, 2015.

Hedelius, J. K., Parker, H., Wunch, D., Roehl, C. M., Viatte, C., Newman, S., Toon, G. C., Podolske, J. R., Hillyard, P. W., Iraci, L. T., Dubey, M. K., and Wennberg, P. O.: Intercomparability of X_{CO_2} and X_{CH_4} from the United States TCCON sites, Atmospheric Measurement Techniques, 10, 1481–1493, https://doi.org/10.5194/amt-10-1481-2017, URL https://amt.copernicus.org/articles/10/1481/2017/, 2017.

Helmig, D., Rossabi, S., Hueber, J., Tans, P., Montzka, S. A., Masarie, K., Thoning, K., Plass-Duelmer, C., Claude, A., Carpenter, L., Lewis, A., and Punjabi, S.: Reversal of global atmospheric ethane and propane trends largely due to US oil and natural gas production, Nature Geoscience, 9, 490–495, https://doi.org/10.1038/ngeo2721, 2016.

Hmiel, B., Petrenko, V. V., Dyonisius, M. N., Buizert, C., Smith, A. M., Place, P. F., Harth, C., Beaudette, R., Hua, Q., Yang, B., Vimont, I., Michel, S. E., Severinghaus, J. P., Etheridge, D., Bromley, T., Schmitt, J., Faïn, X., Weiss, R. F., and Dlugokencky, E.: Preindustrial 14CH4 indicates greater anthropogenic fossil CH4 emissions, Nature, 578, 409–412, https://doi.org/10.1038/s41586-020-1991-8, URL https://doi.org/10.1038/s41586-020-1991-8, 2020.

Holton, J. R.: An introduction to dynamic meteorology, American Journal of Physics, 41, 752–754, 1973.

Hu, H., Landgraf, J., Detmers, R., Borsdorff, T., Aan de Brugh, J., Aben, I., Butz, A., and Hasekamp, O.: Toward Global Mapping of Methane With TROPOMI: First Results and Intersatellite Comparison to GOSAT, Geophysical Research Letters, 45, 3682–3689, https://doi.org/https://doi.org/10.1002/2018GL077259, URL https://agupubs.onlinelibrary.wiley.com/doi/abs/10.1002/2018GL077259, 2018.

IPCC: Climate Change 2013: The Physical Science Basis. Contribution of Working Group I to the Fifth Assessment Report of the Intergovernmental Panel on Climate Change, Cambridge University Press, Cambridge, United Kingdom and New York, NY, USA, https://doi.org/10.1017/CBO9781107415324, URL www.climatechange2013.org, 2013.

Jacobs, N., Simpson, W. R., Wunch, D., O'Dell, C. W., Osterman, G. B., Hase, F., Blumenstock, T., Tu, Q., Frey, M., Dubey, M. K., Parker, H. A., Kivi, R., and Heikkinen, P.: Quality controls, bias, and seasonality of CO_2 columns in the boreal forest with Orbiting Carbon Observatory-2, Total Carbon Column Observing Network, and EM27/SUN measurements, Atmospheric Measurement Techniques, 13, 5033–5063, https://doi.org/10.5194/amt-13-5033-2020, URL https://amt.copernicus.org/articles/13/5033/2020/, 2020.

Janssens-Maenhout, G., Crippa, M., Guizzardi, D., Muntean, M., Schaaf, E., Dentener, F., Bergamaschi, P., Pagliari, V., Olivier, J. G. J., Peters, J. A. H. W., van Aardenne, J. A., Monni, S., Doering, U., and Petrescu, A. M. R.: EDGAR v4.3.2 Global Atlas of the three major Greenhouse Gas Emissions for the period 1970–2012, Earth System Science Data Discussions, 2017, 1–55, https://doi.org/10.5194/essd-2017-79, URL https://essd.copernicus.org/preprints/essd-2017-79/, 2017.

Jiang, G.-S. and Shu, C.-W.: Efficient Implementation of Weighted ENO Schemes, Journal of Computational Physics, 126, 202 – 228, https://doi.org/https://doi.org/10.1006/jcph.1996.0130, URL http://www.sciencedirect.com/science/article/pii/S0021999196901308, 1996.

Jöckel, P., Tost, H., Pozzer, A., Kunze, M., Kirner, O., Brenninkmeijer, C. A. M., Brinkop, S., Cai, D. S., Dyroff, C., Eckstein, J., Frank, F., Garny, H., Gottschaldt, K.-D., Graf, P., Grewe, V., Kerkweg, A., Kern, B., Matthes, S., Mertens, M., Meul, S., Neumaier, M., Nützel, M., Oberländer-Hayn, S., Ruhnke, R., Runde, T., Sander, R., Scharffe, D., and Zahn, A.: Earth System Chemistry integrated Modelling (ESCiMo) with the Modular Earth Submodel System (MESSy) version 2.51, Geosci. Model Dev., 9, 1153–1200, https://doi.org/10.5194/gmd-9-1153-2016, 2016.

Johnston, P. R. and Gulrajani, R. M.: Selecting the corner in the L-curve approach to Tikhonov regularization, IEEE Transactions on Biomedical Engineering, 47, 1293–1296, https://doi.org/10.1109/10.867966, 2000.

Jones, T. S., Franklin, J. E., Chen, J., Dietrich, F., Hajny, K. D., Paetzold, J. C., Wenzel, A., Gately, C., Gottlieb, E., Parker, H., Dubey, M., Hase, F., Shepson, P. B., Mielke, L. H., and Wofsy, S. C.: Assessing Urban Methane Emissions using Column Observing Portable FTIR Spectrometers and a Novel Bayesian Inversion Framework, Atmospheric Chemistry and Physics Discussions, 2021, 1–30, https://doi.org/10.5194/acp-2020-1262, URL https://acp.copernicus.org/preprints/acp-2020-1262/, 2021.

Karakurt, I., Aydin, G., and Aydiner, K.: Mine ventilation air methane as a sustainable energy source, Renewable and Sustainable Energy Reviews, 15, 1042–1049, https://doi.org/10.1016/j.rser.2010.11.030, 2011.

Kiel, M., Wunch, D., Wennberg, P. O., Toon, G. C., Hase, F., and Blumenstock, T.: Improved retrieval of gas abundances from near-infrared solar FTIR spectra measured at the Karlsruhe TCCON station, Atmospheric Measurement Techniques, 9, 669–682, https://doi.org/10.5194/amt-9-669-2016, URL https://amt.copernicus.org/articles/9/669/2016/, 2016.

Kille, N., Chiu, R., Frey, M., Hase, F., Sha, M. K., Blumenstock, T., Hannigan, J. W., Orphal, J., Bon, D., and Volkamer, R.: Separation of Methane Emissions From Agricultural and Natural Gas Sources in the Colorado Front Range, Geophys. Res. Lett., 46, 3990–3998, https://doi.org/10.1029/2019GL082132, 2019.

Kim, A. G.: The composition of coalbed gas, Report of Investigations, 7762, 1973.

Kirschke, S., Bousquet, P., Ciais, P., Saunois, M., Canadell, J. G., Dlugokencky, E. J., Bergamaschi, P., Bergmann, D., Blake, D. R., Bruhwiler, L., Cameron-Smith, P., Castaldi, S., Chevallier, F., Feng, L., Fraser, A., Heimann, M., Hodson, E. L., Houweling, S., Josse, B., Fraser, P. J., Krummel, P. B., Lamarque, J.-F., Langenfelds, R. L., Le Quéré, C., Naik, V., O'Doherty, S., Palmer, P. I., Pison, I., Plummer, D., Poulter, B., Prinn, R. G., Rigby, M., Ringeval, B., Santini, M., Schmidt, M., Shindell, D. T., Simpson, I. J., Spahni, R., Steele, L. P., Strode, S. A., Sudo, K., Szopa, S., van der Werf, G. R., Voulgarakis, A., van Weele, M., Weiss, R. F., Williams, J. E., and Zeng, G.: Three decades of global methane sources and sinks, Nature Geoscience, 6, 813–823, https://doi.org/10.1038/ngeo1955, 2013.

Kędzior, S. and Dreger, M.: Methane occurrence, emissions and hazards in the Upper Silesian Coal Basin, Poland, International Journal of Coal Geology, 211, 103 226, https://doi.org/doi.org/10.1016/j.coal.2019.103226, URL http://www.sciencedirect.com/science/article/pii/S0166516218311492, 2019.

Klappenbach, F., Bertleff, M., Kostinek, J., Hase, F., Blumenstock, T., Agusti-Panareda, A., Razinger, M., and Butz, A.: Accurate mobile remote sensing of XCO_2 and XCH_4 latitudinal transects from aboard a research vessel, Atmos. Meas. Tech., 8, 5023–5038, https://doi.org/10.5194/amt-8-5023-2015, 2015.

Klappenbach, F. W.: Mobile spectroscopic measurements of atmospheric carbon dioxide and methane, Ph.D. thesis, Karlsruhe Institut für Technologie, 2016.

Kleinschek, R., Kostinek, J., Holzbeck, P., Knapp, M., Luther, A., Hase, F., and Butz, A.: Development of a Fast Solar Tracker Enabling Atmospheric Direct Sun Remote Sensing Applications on Different Moving Platforms, in: EGU General Assembly Conference Abstracts, p. 9596, 2020.

Knapp, M., Kleinschek, R., Hase, F., Agustí-Panareda, A., Inness, A., Barré, J., Landgraf, J., Borsdorff, T., Kinne, S., and Butz, A.: Shipborne measurements of XCO_2, XCH_4, and XCO above the Pacific Ocean and comparison to CAMS atmospheric analyses and S5P/TROPOMI, Earth System Science Data, 13, 199–211, https://doi.org/10.5194/essd-13-199-2021, URL `https://essd.copernicus.org/articles/13/199/2021/`, 2021.

Kondracki, J.: Natural Regions of Poland, POLISH GEOGRAPHICAL REVIEW, p. 48, 1956.

Kostinek, J., Roiger, A., Davis, K. J., Sweeney, C., DiGangi, J. P., Choi, Y., Baier, B., Hase, F., Groß, J., Eckl, M., Klausner, T., and Butz, A.: Adaptation and performance assessment of a quantum and interband cascade laser spectrometer for simultaneous airborne in situ observation of CH_4, C_2H_6, CO_2, CO and N_2O, Atmos. Meas. Tech., 12, 1767–1783, https://doi.org/10.5194/amt-12-1767-2019, 2019.

Kostinek, J., Roiger, A., Eckl, M., Fiehn, A., Luther, A., Wildmann, N., Klausner, T., Fix, A., Knote, C., Stohl, A., and Butz, A.: Estimating Upper Silesian coal mine methane emissions from airborne in situ observations and dispersion modeling, Atmospheric Chemistry and Physics Discussions, 2020, 1–24, https://doi.org/10.5194/acp-2020-962, URL `https://acp.copernicus.org/preprints/acp-2020-962/`, 2020.

Krautwurst, S., Gerilowski, K., Borchardt, J., Wildmann, N., Galkowski, M., Swolkien, J., Marshall, J., Fiehn, A., Roiger, A., Ruhtz, T., Gerbig, C., Necki, J., Burrows, J. P., Fix, A., and Bovensmann, H.: Quantification of CH_4 coal mining emissions in Upper Silesia by passive airborne remote sensing observations with the MAMAP instrument during CoMet, Atmospheric Chemistry and Physics Discussions, 2021, 1–39, https://doi.org/10.5194/acp-2020-1014, URL `https://acp.copernicus.org/preprints/acp-2020-1014/`, 2021.

Krings, T., Gerilowski, K., Buchwitz, M., Reuter, M., Tretner, A., Erzinger, J., Heinze, D., Pflüger, U., Burrows, J. P., and Bovensmann, H.: MAMAP - a new spectrometer system for column-averaged methane and carbon dioxide observations from aircraft: retrieval algorithm and first inversions for point source emission rates, Atmos. Meas. Tech., 4, 1735–1758, https://doi.org/10.5194/amt-4-1735-2011, 2011.

Krings, T., Gerilowski, K., Buchwitz, M., Hartmann, J., Sachs, T., Erzinger, J., Burrows, J. P., and Bovensmann, H.: Quantification of methane emission rates from coal mine

ventilation shafts using airborne remote sensing data, Atmos. Meas. Tech., 6, 151–166, https://doi.org/10.5194/amt-6-151-2013, 2013.

Kud, M.: personal communication, 2017.

Kurnia, J. C., Chaedir, B. A., Lim, D. C., Chen, L., Jiang, L., and Sasmito, A. P.: Numerical Evaluation of Potential Catalyst Savings for Ventilation Air Methane Catalytic Combustion in Helical Coil Reactors with Selective Wall Coating, Catalysts, 9, 380, https://doi.org/10.3390/catal9040380, 2019.

Kuze, A., Suto, H., Nakajima, M., and Hamazaki, T.: Thermal and near infrared sensor for carbon observation Fourier-transform spectrometer on the Greenhouse Gases Observing Satellite for greenhouse gases monitoring, Appl. Opt., 48, 6716–6733, https://doi.org/10.1364/AO.48.006716, URL http://ao.osa.org/abstract.cfm?URI=ao-48-35-6716, 2009.

Lorente, A., Borsdorff, T., Butz, A., Hasekamp, O., aan de Brugh, J., Schneider, A., Wu, L., Hase, F., Kivi, R., Wunch, D., Pollard, D. F., Shiomi, K., Deutscher, N. M., Velazco, V. A., Roehl, C. M., Wennberg, P. O., Warneke, T., and Landgraf, J.: Methane retrieved from TROPOMI: improvement of the data product and validation of the first 2 years of measurements, Atmospheric Measurement Techniques, 14, 665–684, https://doi.org/10.5194/amt-14-665-2021, URL https://amt.copernicus.org/articles/14/665/2021/, 2021.

Loulergue, L., Schilt, A., Spahni, R., Masson-Delmotte, V., Blunier, T., Lemieux, B., Barnola, J.-M., Raynaud, D., Stocker, T. F., and Chappellaz, J.: Orbital and millennial-scale features of atmospheric CH4 over the past 800,000 years, Nature, 453, 383–386, https://doi.org/10.1038/nature06950, URL https://doi.org/10.1038/nature06950, 2008.

Luther, A., Kleinschek, R., Scheidweiler, L., Defratyka, S., Stanisavljevic, M., Forstmaier, A., Dandocsi, A., Wolff, S., Dubravica, D., Wildmann, N., Kostinek, J., Jöckel, P., Nickl, A.-L., Klausner, T., Hase, F., Frey, M., Chen, J., Dietrich, F., Nęcki, J., Swolkień, J., Fix, A., Roiger, A., and Butz, A.: Quantifying CH_4 emissions from hard coal mines using mobile sun-viewing Fourier transform spectrometry, Atmospheric Measurement Techniques, 12, 5217–5230, https://doi.org/10.5194/amt-12-5217-2019, URL https://amt.copernicus.org/articles/12/5217/2019/, 2019.

Maasakkers, J. D., Jacob, D. J., Sulprizio, M. P., Scarpelli, T. R., Nesser, H., Sheng, J., Zhang, Y., Lu, X., Bloom, A. A., Bowman, K. W., Worden, J. R., and Parker, R. J.: 2010–2015 North American methane emissions, sectoral contributions, and trends: a high-resolution inversion of GOSAT satellite observations of atmospheric methane, Atmospheric Chemistry and Physics Discussions, 2020, 1–28, https://doi.org/10.5194/acp-2020-915, URL https://acp.copernicus.org/preprints/acp-2020-915/, 2020.

Maazallahi, H., Zavala-Araiza, D., Schwietzke, S., Menoud, M., Fernandez, J., Fisher, R., Lowry, D., Nisbet, E., van der Gon, H. D., and Röckmann, T.: Mapping, emission quantification, and attribution of methane enhancements across two European cities; Utrecht, NL and Hamburg, DE., in: Geophysical Research Abstracts, vol. 21, 2019.

Makarova, M. V., Alberti, C., Ionov, D. V., Hase, F., Foka, S. C., Blumenstock, T., Warneke, T., Virolainen, Y., Kostsov, V., Frey, M., Poberovskii, A. V., Timofeyev, Y. M., Paramonova, N., Volkova, K. A., Zaitsev, N. A., Biryukov, E. Y., Osipov, S. I., Makarov, B. K., Polyakov, A. V., Ivakhov, V. M., Imhasin, H. K., and Mikhailov, E. F.: Emission Monitoring Mobile Experiment (EMME): an overview and first results of the St. Petersburg megacity campaign-2019, Atmospheric Measurement Techniques Discussions, 2020, 1–45, https://doi.org/10.5194/amt-2020-87, URL `https://www.atmos-meas-tech-discuss.net/amt-2020-87/`, 2020.

Mays, K. L., Shepson, P. B., Stirm, B. H., Karion, A., Sweeney, C., and Gurney, K. R.: Aircraft-Based Measurements of the Carbon Footprint of Indianapolis, Environ. Sci. Technol., 43, 7816–7823, https://doi.org/10.1021/es901326b, 2009.

NASA: Goddard automailer, URL `https://acd-ext.gsfc.nasa.gov/Data_services/automailer/index.html`, 2018.

National Census of Population and Housing 2021: Yearbook of Labour Statistics 2019, URL `https://stat.gov.pl/en/topics/statistical-yearbooks/statistical-yearbooks/yearbook-of-labour-statistics-2019,10,7.html`, accessed: 2020-11-10.

NCEP: NCEP GDAS/FNL 0.25 Degree Global Tropospheric Analyses and Forecast Grids, URL `https://doi.org/10.5065/D65Q4T4Z`, 2017.

Nickl, A.-L., Mertens, M., Roiger, A., Fix, A., Amediek, A., Fiehn, A., Gerbig, C., Galkowski, M., Kerkweg, A., Klausner, T., Eckl, M., and Jöckel, P.: Hindcasting and forecasting of regional methane from coal mine emissions in the Upper Silesian Coal Basin using the online nested global regional chemistry–climate model MECO(n) (MESSy v2.53), Geoscientific Model Development, 13, 1925–1943, https://doi.org/10.5194/gmd-13-1925-2020, URL `https://gmd.copernicus.org/articles/13/1925/2020/`, 2020.

Nisbet, E. G., Dlugokencky, E. J., and Bousquet, P.: Methane on the Rise – Again, Science, 343, 493–495, https://doi.org/10.1126/science.1247828, 2014.

Nisbet, E. G., Dlugokencky, E. J., Manning, M. R., Lowry, D., Fisher, R. E., France, J. L., Michel, S. E., Miller, J. B., White, J. W. C., Vaughn, B., Bousquet, P., Pyle, J. A., Warwick, N. J., Cain, M., Brownlow, R., Zazzeri, G., Lanoisellé, M., Manning, A. C., Gloor, E., Worthy, D. E. J., Brunke, E.-G., Labuschagne, C., Wolff, E. W., and Ganesan, A. L.: Rising atmospheric methane: 2007–2014 growth and isotopic shift,

Global Biogeochemical Cycles, 30, 1356–1370, https://doi.org/10.1002/2016GB005406, 2016.

NOAA: Global Monitoring Laboratory, GGGRN, URL https://esrl.noaa.gov/gmd/ccgg/about.html, accessed: 2020-07-10.

O'Connor, E. J., Illingworth, A. J., Brooks, I. M., Westbrook, C. D., Hogan, R. J., Davies, F., and Brooks, B. J.: A Method for Estimating the Turbulent Kinetic Energy Dissipation Rate from a Vertically Pointing Doppler Lidar, and Independent Evaluation from Balloon-Borne In Situ Measurements, Journal of Atmospheric and Oceanic Technology, 27, 1652 – 1664, https://doi.org/10.1175/2010JTECHA1455.1, URL https://journals.ametsoc.org/view/journals/atot/27/10/2010jtecha1455_1.xml, 2010.

O'Shea, S. J., Allen, G., Fleming, Z. L., Bauguitte, S. J.-B., Percival, C. J., Gallagher, M. W., Lee, J., Helfter, C., and Nemitz, E.: Area fluxes of carbon dioxide, methane, and carbon monoxide derived from airborne measurements around Greater London: A case study during summer 2012, Journal of Geophysical Research: Atmospheres, 119, 4940–4952, https://doi.org/10.1002/2013JD021269, 2014.

Petty, G. W.: A first Course in Atmospheric Radiation, vol. 2, Camebridge University Press, 2006.

Phillips, D. L.: A Technique for the Numerical Solution of Certain Integral Equations of the First Kind, J. ACM, 9, 84–97, https://doi.org/10.1145/321105.321114, URL https://doi.org/10.1145/321105.321114, 1962.

Polandin: Cause of accident in coal mine announced, URL https://polandin.com/39304200/cause-of-accident-in-coal-mine-announced, accessed: 2020-11-17, 2018.

Rodgers, C. D.: Inverse methods for atmospheric sounding: theory and practice, vol. 2, World scientific, 2000.

Rothman, L., Gordon, I., Barbe, A., Benner, D., Bernath, P., Birk, M., Boudon, V., Brown, L., Campargue, A., Champion, J.-P., Chance, K., Coudert, L., Dana, V., Devi, V., Fally, S., Flaud, J.-M., Gamache, R., Goldman, A., Jacquemart, D., Kleiner, I., Lacome, N., Lafferty, W., Mandin, J.-Y., Massie, S., Mikhailenko, S., Miller, C., Moazzen-Ahmadi, N., Naumenko, O., Nikitin, A., Orphal, J., Perevalov, V., Perrin, A., Predoi-Cross, A., Rinsland, C., Rotger, M., Šimecková, M., Smith, M., Sung, K., Tashkun, S., Tennyson, J., Toth, R., Vandaele, A., and Auwera, J. V.: The HITRAN 2008 molecular spectroscopic database, J. Quant. Spectrosc. Radiat. Transfer, 110, 533 – 572, https://doi.org/10.1016/j.jqsrt.2009.02.013, 2009.

Saunois, M., Jackson, R. B., Bousquet, P., Poulter, B., and Canadell, J. G.: The growing role of methane in anthropogenic climate change, Environmental Research Letters, 11,

120 207, https://doi.org/10.1088/1748-9326/11/12/120207, URL https://doi.org/10.1088/1748-9326/11/12/120207, 2016.

Saunois, M., Stavert, A. R., Poulter, B., Bousquet, P., Canadell, J. G., Jackson, R. B., Raymond, P. A., Dlugokencky, E. J., Houweling, S., Patra, P. K., Ciais, P., Arora, V. K., Bastviken, D., Bergamaschi, P., Blake, D. R., Brailsford, G., Bruhwiler, L., Carlson, K. M., Carrol, M., Castaldi, S., Chandra, N., Crevoisier, C., Crill, P. M., Covey, K., Curry, C. L., Etiope, G., Frankenberg, C., Gedney, N., Hegglin, M. I., Höglund-Isaksson, L., Hugelius, G., Ishizawa, M., Ito, A., Janssens-Maenhout, G., Jensen, K. M., Joos, F., Kleinen, T., Krummel, P. B., Langenfelds, R. L., Laruelle, G. G., Liu, L., Machida, T., Maksyutov, S., McDonald, K. C., McNorton, J., Miller, P. A., Melton, J. R., Morino, I., Müller, J., Murguia-Flores, F., Naik, V., Niwa, Y., Noce, S., O'Doherty, S., Parker, R. J., Peng, C., Peng, S., Peters, G. P., Prigent, C., Prinn, R., Ramonet, M., Regnier, P., Riley, W. J., Rosentreter, J. A., Segers, A., Simpson, I. J., Shi, H., Smith, S. J., Steele, L. P., Thornton, B. F., Tian, H., Tohjima, Y., Tubiello, F. N., Tsuruta, A., Viovy, N., Voulgarakis, A., Weber, T. S., van Weele, M., van der Werf, G. R., Weiss, R. F., Worthy, D., Wunch, D., Yin, Y., Yoshida, Y., Zhang, W., Zhang, Z., Zhao, Y., Zheng, B., Zhu, Q., Zhu, Q., and Zhuang, Q.: The Global Methane Budget 2000–2017, Earth System Science Data, 12, 1561–1623, https://doi.org/10.5194/essd-12-1561-2020, URL https://essd.copernicus.org/articles/12/1561/2020/, 2020.

Scarpelli, T. R., Jacob, D. J., Maasakkers, J. D., Sulprizio, M. P., Sheng, J.-X., Rose, K., Romeo, L., Worden, J. R., and Janssens-Maenhout, G.: A global gridded ($0.1^\circ \times 0.1^\circ$) inventory of methane emissions from oil, gas, and coal exploitation based on national reports to the United Nations Framework Convention on Climate Change, Earth System Science Data, 12, 563–575, https://doi.org/10.5194/essd-12-563-2020, URL https://essd.copernicus.org/articles/12/563/2020/, 2020.

Schepers, D., Guerlet, S., Butz, A., Landgraf, J., Frankenberg, C., Hasekamp, O., Blavier, J.-F., Deutscher, N. M., Griffith, D. W. T., Hase, F., Kyro, E., Morino, I., Sherlock, V., Sussmann, R., and Aben, I.: Methane retrievals from Greenhouse Gases Observing Satellite (GOSAT) shortwave infrared measurements: Performance comparison of proxy and physics retrieval algorithms, Journal of Geophysical Research: Atmospheres, 117, https://doi.org/https://doi.org/10.1029/2012JD017549, URL https://agupubs.onlinelibrary.wiley.com/doi/abs/10.1029/2012JD017549, 2012.

Schütze, C. and Sauer, U.: Challenges associated with the atmospheric monitoring of areal emission sources and the need for optical remote sensing techniques—an open-path Fourier transform infrared (OP-FTIR) spectroscopy experience report, Environmental Earth Sciences, 75, 919, https://doi.org/10.1007/s12665-016-5482-z, URL https://doi.org/10.1007/s12665-016-5482-z, 2016.

Schwietzke, S., Sherwood, O. A., Bruhwiler, L. M., Miller, J. B., Etiope, G., Dlugokencky, E. J., Michel, S. E., Arling, V. A., Vaughn, B. H., White, J. W., and Tans, P. P.: Upward

revision of global fossil fuel methane emissions based on isotope database, Nature, 538, 88, https://doi.org/10.1038/nature19797, 2016.

Skamarock, W. C., Klemp, J. B., Dudhia, J., Gill, D. O., Barker, D. M., Duda, M. G., Huang, X.-Y., Wang, W., and Powers, J. G.: A description of the Advanced Research WRF version 3, in: NCAR Tech. Note NCAR/TN-475+ STR, https://doi.org/10.5065/D68S4MVH, 2008.

Skamarock, W. C., Klemp, J. B., Dudhia, J., Gill, D. O., Barker, D. M., Duda, M. G., Huang, X.-Y., Wang, W., and Powers, J. G.: A description of the Advanced Research WRF version 4, in: NCAR Tech. Note NCAR/TN-556+ STR, https://doi.org/10.5065/1dfh-6p97, 2019.

Smalikho, I. N.: Techniques of Wind Vector Estimation from Data Measured with a Scanning Coherent Doppler Lidar, J. Atmos. Oceanic Technol., 20, 276–291, https://doi.org/10.1175/1520-0426(2003)020<0276:TOWVEF>2.0.CO;2, 2003.

Smalikho, I. N. and Banakh, V. A.: Measurements of wind turbulence parameters by a conically scanning coherent Doppler lidar in the atmospheric boundary layer, Atmos. Meas. Tech., 10, 4191–4208, https://doi.org/10.5194/amt-10-4191-2017, 2017.

Stamnes, K., Thomas, G. E., and Stamnes, J. J.: Radiative transfer in the atmosphere and ocean, Cambridge University Press, https://doi.org/10.1017/9781316148549, 2017.

Stec, K.: Characteristics of seismic activity of the Upper Silesian Coal Basin in Poland, Geophysical Journal International, 168, 757–768, 2007.

Stephan, A., Wildmann, N., and Smalikho, I. N.: Effectiveness of the MFAS method for retrieval of height profiles of speed and direction of the wind from measurements by a Windcube 200s lidar, https://doi.org/10.1117/12.2504450, 2018a.

Stephan, A., Wildmann, N., and Smalikho, I. N.: Spatiotemporal visualization of wind turbulence from measurements by a Windcube 200s lidar in the atmospheric boundary layer, https://doi.org/10.1117/12.2504468, 2018b.

Stohl, A.: Computation, accuracy and applications of trajectories—a review and bibliography, Atmospheric Environment, 32, 947–966, 1998.

Stohl, A., Forster, C., Frank, A., Seibert, P., and Wotawa, G.: Technical note: The Lagrangian particle dispersion model FLEXPART version 6.2, Atmospheric Chemistry and Physics, 5, 2461–2474, https://doi.org/10.5194/acp-5-2461-2005, URL `https://acp.copernicus.org/articles/5/2461/2005/`, 2005.

Strąpoć, D., Mastalerz, M., Dawson, K., Macalady, J., Callaghan, A. V., Wawrik, B., Turich, C., and Ashby, M.: Biogeochemistry of Microbial Coal-Bed Methane, Annual Review of Earth and Planetary Sciences, 39, 617–

656, https://doi.org/10.1146/annurev-earth-040610-133343, URL https://doi.org/10.1146/annurev-earth-040610-133343, 2011.

Sussmann, R., Forster, F., Rettinger, M., and Bousquet, P.: Renewed methane increase for five years (2007–2011) observed by solar FTIR spectrometry, Atmospheric Chemistry and Physics, 12, 4885–4891, https://doi.org/10.5194/acp-12-4885-2012, URL https://acp.copernicus.org/articles/12/4885/2012/, 2012.

Swolkien, J.: personal communication, 2018.

Szczepanska, J. and Twardowska, I.: Distribution and environmental impact of coal-mining wastes in Upper Silesia, Poland, Environmental Geology, 38, 249–258, 1999.

Thakur, P. C., Graham-Bryce, I. J., Karis, W. G., and Sullivan, K. M.: Global methane emissions from the world coal industry, Environmental Monitoring and Assessment, 31, 73–91, https://doi.org/10.1007/BF00547183, URL https://doi.org/10.1007/BF00547183, 1994.

Thompson, A.: The Oxidizing Capacity of the Earth's Atmosphere: Probable Past and Future Changes, Science, 256, https://doi.org/10.1126/science.256.5060.1157, 1992.

Tikhonov, A. N.: On the solution of ill-posed problems and the method of regularization, in: Doklady Akademii Nauk, vol. 151, pp. 501–504, Russian Academy of Sciences, 1963.

Toja-Silva, F., Chen, J., Hachinger, S., and Hase, F.: CFD simulation of CO2 dispersion from urban thermal power plant: Analysis of turbulent Schmidt number and comparison with Gaussian plume model and measurements, J. Wind Eng. Ind. Aerodyn., 169, 177 – 193, https://doi.org/10.1016/j.jweia.2017.07.015, 2017.

Toon, G. C.: Atmospheric Line List for the 2014 TCCON Data Release, https://doi.org/10.14291/tccon.ggg2014.atm.r0/1221656, 2017.

Tratt, D. M., Young, S. J., Lynch, D. K., Buckland, K. N., Johnson, P. D., Hall, J. L., Westberg, K. R., Polak, M. L., Kasper, B. P., and Qian, J.: Remotely sensed ammonia emission from fumarolic vents associated with a hydrothermally active fault in the Salton Sea Geothermal Field, California, J. Geophys. Res. Atmos., 116, https://doi.org/10.1029/2011JD016282, 2011.

Tratt, D. M., Buckland, K. N., Hall, J. L., Johnson, P. D., Keim, E. R., Leifer, I., Westberg, K., and Young, S. J.: Airborne visualization and quantification of discrete methane sources in the environment, Rem. Sens. Envir., 154, 74 – 88, https://doi.org/10.1016/j.rse.2014.08.011, 2014.

Twomey, S.: On the Numerical Solution of Fredholm Integral Equations of the First Kind by the Inversion of the Linear System Produced by Quadrature, J. ACM, 10, 97–101, https://doi.org/10.1145/321150.321157, URL https://doi.org/10.1145/321150.321157, 1963.

Varon, D. J., Jacob, D. J., McKeever, J., Jervis, D., Durak, B. O. A., Xia, Y., and Huang, Y.: Quantifying methane point sources from fine-scale satellite observations of atmospheric methane plumes, Atmos. Meas. Tech., 11, 5673–5686, https://doi.org/10.5194/amt-11-5673-2018, 2018.

Vasiljević, N., Lea, G., Courtney, M., Cariou, J.-P., Mann, J., and Mikkelsen, T.: Long-range WindScanner system, Remote Sens., 8, 896, https://doi.org/10.3390/rs8110896, 2016.

Veefkind, J., Aben, I., McMullan, K., Förster, H., de Vries, J., Otter, G., Claas, J., Eskes, H., de Haan, J., Kleipool, Q., van Weele, M., Hasekamp, O., Hoogeveen, R., Landgraf, J., Snel, R., Tol, P., Ingmann, P., Voors, R., Kruizinga, B., Vink, R., Visser, H., and Levelt, P.: TROPOMI on the ESA Sentinel-5 Precursor: A GMES mission for global observations of the atmospheric composition for climate, air quality and ozone layer applications, Remote Sensing of Environment, 120, 70 – 83, https://doi.org/https://doi.org/10.1016/j.rse.2011.09.027, URL http://www.sciencedirect.com/science/article/pii/S0034425712000661, the Sentinel Missions - New Opportunities for Science, 2012.

Viatte, C., Lauvaux, T., Hedelius, J. K., Parker, H., Chen, J., Jones, T., Franklin, J. E., Deng, A. J., Gaudet, B., Verhulst, K., Duren, R., Wunch, D., Roehl, C., Dubey, M. K., Wofsy, S., and Wennberg, P. O.: Methane emissions from dairies in the Los Angeles Basin, Atmos. Chem. Phys., 17, 7509–7528, https://doi.org/10.5194/acp-17-7509-2017, 2017.

Vogel, F. R., Frey, M., Staufer, J., Hase, F., Broquet, G., Xueref-Remy, I., Chevallier, F., Ciais, P., Sha, M. K., Chelin, P., Jeseck, P., Janssen, C., Té, Y., Groß, J., Blumenstock, T., Tu, Q., and Orphal, J.: XCO_2 in an emission hot-spot region: the COCCON Paris campaign 2015, Atmospheric Chemistry and Physics, 19, 3271–3285, https://doi.org/10.5194/acp-19-3271-2019, URL https://acp.copernicus.org/articles/19/3271/2019/, 2019.

Wallace, J. M. and Hobbs, P. V.: Atmospheric science: an introductory survey, vol. 92, Elsevier, 2006.

Wendisch, M. and Yang, P.: Theory of Atmospheric Radiative Transfer. A Comprehensive Introduction, Wiley-VCH Verlag GmbH Co. KGaA, 2012.

White, W., Anderson, J., Blumenthal, D., Husar, R., Gillani, N., Husar, J., and Wilson, W.: Formation and transport of secondary air pollutants: ozone and aerosols in the St. Louis urban plume, Science, 194, 187–189, https://doi.org/10.1126/science.959846, 1976.

Wikipedia, List of mining disasters in Poland: List of mining disasters in Poland, URL https://en.wikipedia.org/wiki/List_of_mining_disasters_in_Poland, accessed: 2020-11-17, 2020.

Wildmann, N., Vasiljevic, N., and Gerz, T.: Wind turbine wake measurements with automatically adjusting scanning trajectories in a multi-Doppler lidar setup, Atmospheric Measurement Techniques, 11, 3801–3814, https://doi.org/10.5194/amt-11-3801-2018, URL https://www.atmos-meas-tech.net/11/3801/2018/, 2018.

Worden, J. R., Bloom, A. A., Pandey, S., Jiang, Z., Worden, H. M., Walker, T. W., Houweling, S., and Röckmann, T.: Reduced biomass burning emissions reconcile conflicting estimates of the post-2006 atmospheric methane budget, Nature communications, 8, 2227, https://doi.org/10.1038/s41467-017-02246-0, 2017.

Wunch, D., Toon, G. C., Blavier, J.-F. L., Washenfelder, R. A., Notholt, J., Connor, B. J., Griffith, D. W. T., Sherlock, V., and Wennberg, P. O.: The Total Carbon Column Observing Network, Philosophical Transactions of the Royal Society A: Mathematical, Physical and Engineering Sciences, 369, 2087–2112, https://doi.org/10.1098/rsta.2010.0240, URL https://royalsocietypublishing.org/doi/abs/10.1098/rsta.2010.0240, 2011.

Yang, S., Petersen, G. N., von Löwis, S., Preißler, J., and Finger, D. C.: Determination of eddy dissipation rate by Doppler lidar in Reykjavik, Iceland, Meteorological Applications, 27, e1951, https://doi.org/https://doi.org/10.1002/met.1951, URL https://rmets.onlinelibrary.wiley.com/doi/abs/10.1002/met.1951, 2020.

Yokota, T., Oguma, H., Morino, I., Higurashi, A., Aoki, T., and Inoue, G.: Test measurements by a BBM of the nadir-looking SWIR FTS aboard GOSAT to monitor CO2 column density from space, in: Passive Optical Remote Sensing of the Atmosphere and Clouds IV, edited by Tsay, S. C., Yokota, T., and Ahn, M.-H., vol. 5652, pp. 182 – 188, International Society for Optics and Photonics, SPIE, https://doi.org/10.1117/12.578497, URL https://doi.org/10.1117/12.578497, 2004.

Appendix A

How to use passive tracer in WRF

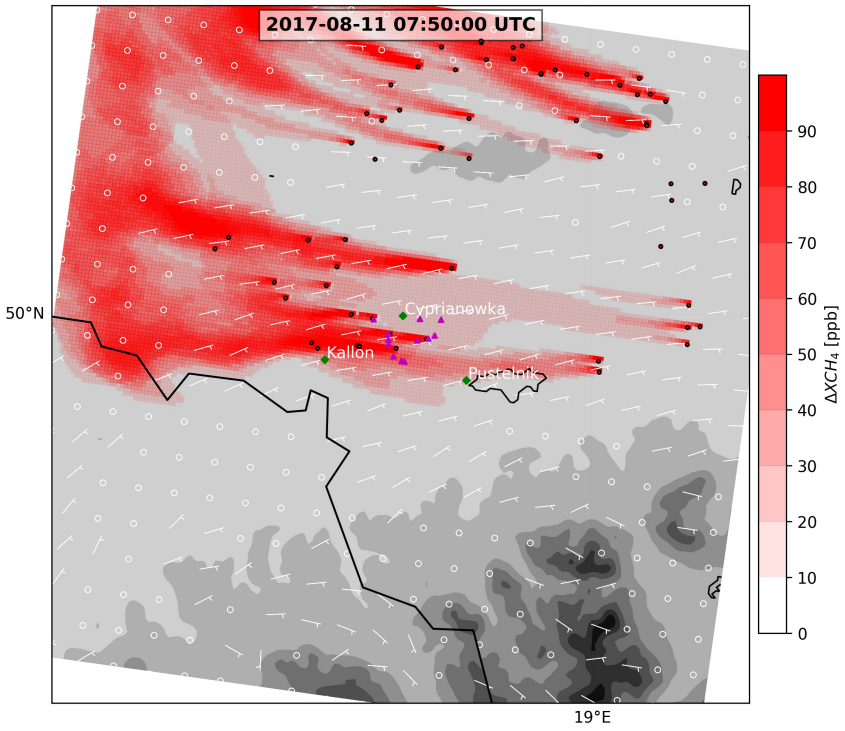

Figure A.1: Simulated methane coal-mine emissions in the Upper Silesian coal basin.

This guide is based on the web-tutorial from Brian Blaylock from the university of Utah `http://home.chpc.utah.edu/~u0553130/Brian_Blaylock/tracer.html`. His work was also published in Blaylock et al. 2017 (`http://journals.ametsoc.org/doi/abs/10.1175/JAMC-D-16-0216.1`). The process of passive tracer implementation consists of five

steps. 1) The tracers need to be allocated in the file `WRFV3/Registry/Registry.EM`. 2) Every tracer needs to be initialized in `WRFV3/dyn_em/module_initialize_real.F` with its WRF-coordinates i, j, k in the respective WRF domain. This generates one single emission blob at every introduced location. 3) To make the tracers continuous, the WRF coordinates are introduced to `WRFV3/dyn_em/solve_em.F`. 4) The WRF passive tracer option is enabled by changing the `tracer_opt` flag in the `namelist.input` file to the number 2 for each domain needed. In the last step 5) the WRF output is increased to receive tracer information on a more frequent basis than the standard output which is also adjusted in the `namelist.input` file. Passive tracers can be used to simulate how air-parcels are transported by the modelled winds when released at a certain location.

To activate the tracers several files need to be adapated:

- `WRFV3/Registry/Registry.EM`
- `WRFV3/dyn_em/module_initialize_real.F`
- `WRFV3/dyn_em/solve_em.F`
- `WRFV3/test/em_real/namelist.input`

Note that WRF needs to be re-compiled after changing the first three files.

WRFV3/Registry/Registry.EM

Add lines at the end of the file (copy paste to avoid typos). `tr17_1` - `tr17_8` should not be deleted but seem to be unused. Also make sure that the names chosen also appear in the last line after `package tracer_test1 tracer_opt==2` etc.

```
# Registry entries that are exclusive to Registry.EM

# Chem Scalars
rconfig   integer     chem_opt           namelist,physics      max_domains    0       rh       "chem_opt"             ""      ""
state   real    -             ikjftb   chem       1        -     -    -
#
# Tracer Scalars: If you want full resolved and non-resolved dispersion, compile WRF-Chem
#
state   real    -          ikjftb  tracer       1         -     -    -
state   real    tr17_1     ikjftb  tracer       1         -     irhusdf=(bdy_interp:dt)    "tr17_1"        "tr17_1"     "Dimensionless"
state   real    tr17_2     ikjftb  tracer       1         -     irhusdf=(bdy_interp:dt)    "tr17_2"        "tr17_2"     "Dimensionless"
state   real    tr17_3     ikjftb  tracer       1         -     irhusdf=(bdy_interp:dt)    "tr17_3"        "tr17_3"     "Dimensionless"
state   real    tr17_4     ikjftb  tracer       1         -     irhusdf=(bdy_interp:dt)    "tr17_4"        "tr17_4"     "Dimensionless"
state   real    tr17_5     ikjftb  tracer       1         -     irhusdf=(bdy_interp:dt)    "tr17_5"        "tr17_5"     "Dimensionless"
state   real    tr17_6     ikjftb  tracer       1         -     irhusdf=(bdy_interp:dt)    "tr17_6"        "tr17_6"     "Dimensionless"
state   real    tr17_7     ikjftb  tracer       1         -     irhusdf=(bdy_interp:dt)    "tr17_7"        "tr17_7"     "Dimensionless"
state   real    tr17_8     ikjftb  tracer       1         -     irhusdf=(bdy_interp:dt)    "tr17_8"        "tr17_8"     "Dimensionless"
state   real    N_SLV      ikjftb  tracer       1         -     irhusdf=(bdy_interp:dt)    "N_SLV"         "N_SLV"      "Dimensionless"
state   real    BKBplm     ikjftb  tracer       1         -     irhusdf=(bdy_interp:dt)    "BKBplm"        "BKBplm"     "Dimensionless"
state   real    PNIOWEK3      ikjftb  tracer       1         -     irhusdf=(bdy_interp:dt)    "PNIOWEK3"         "PNIOWEK3"      "Dimensionless"
state   real    PNIOWEK4      ikjftb  tracer       1         -     irhusdf=(bdy_interp:dt)    "PNIOWEK4"         "PNIOWEK4"      "Dimensionless"
state   real    PNIOWEK5      ikjftb  tracer       1         -     irhusdf=(bdy_interp:dt)    "PNIOWEK5"         "PNIOWEK5"      "Dimensionless"
state   real    BORYN      ikjftb  tracer       1         -     irhusdf=(bdy_interp:dt)    "BORYN"         "BORYN"      "Dimensionless"
state   real    KRUPI      ikjftb  tracer       1         -     irhusdf=(bdy_interp:dt)    "KRUPI"         "KRUPI"      "Dimensionless"
state   real    SILES      ikjftb  tracer       1         -     irhusdf=(bdy_interp:dt)    "SILES"         "SILES"      "Dimensionless"
state   real    RYDUL      ikjftb  tracer       1         -     irhusdf=(bdy_interp:dt)    "RYDUL"         "RYDUL"      "Dimensionless"
state   real    JASTZR4      ikjftb  tracer       1         -     irhusdf=(bdy_interp:dt)    "JASTZR4"         "JASTZR4"      "Dimensionless"
state   real    JASTZR6      ikjftb  tracer       1         -     irhusdf=(bdy_interp:dt)    "JASTZR6"         "JASTZR6"      "Dimensionless"
state   real    SOSNI      ikjftb  tracer       1         -     irhusdf=(bdy_interp:dt)    "SOSNI"         "SOSNI"      "Dimensionless"
state   real    DULCZ      ikjftb  tracer       1         -     irhusdf=(bdy_interp:dt)    "DULCZ"         "DULCZ"      "Dimensionless"

package   tracer_test1  tracer_opt==2      -           tracer:tr17_1,tr17_2,tr17_3,tr17_4,tr17_5,tr17_6,tr17_7,tr17_8,N_SLV,BKBplm,PNIOWEK3,PNIOWEK
4,PNIOWEK5,BORYN,KRUPI,SILES,RYDUL,JASTZR4,JASTZR6,SOSNI,DULCZ
```

Figure A.2: Registry.EM file with 13 additional tracers.

WRFV3/dyn_em/module_initialize_real.F

In this file the tracers are initialized in WRF. Somewhere around line 3360 after the line

`grid\%save_topo_from_real=1` with the same indent the tracers are initialized. Tracers can start at a single cell or multiple cells. The i and j coordinates refer to the WRF-domain in which the tracers are initialized.

```
3408       ! PniowekIII
3409       IF (config_flags%tracer_opt .eq. 2) THEN
3410          IF (grid%id == 3) THEN
3411            i = 96
3412            j = 99
3413            IF ( its .LE. i .and. ite .GE. i .and. jts .LE. j .and. jte .GE. j) THEN
3414             tracer(i, 1, j, P_PNIOWEK3) = 1.0
3415            END IF
3416          END IF
3417       END IF
3418
3419       ! PniowekIV
3420       IF (config_flags%tracer_opt .eq. 2) THEN
3421          IF (grid%id == 3) THEN
3422            i = 94
3423            j = 103
3424            IF ( its .LE. i .and. ite .GE. i .and. jts .LE. j .and. jte .GE. j) THEN
3425             tracer(i, 1, j, P_PNIOWEK4) = 1.0
3426            END IF
3427          END IF
3428       END IF
3429
3430       ! PniowekV
3431       IF (config_flags%tracer_opt .eq. 2) THEN
3432          IF (grid%id == 3) THEN
3433            i = 104
3434            j = 103
3435            IF ( its .LE. i .and. ite .GE. i .and. jts .LE. j .and. jte .GE. j) THEN
3436             tracer(i, 1, j, P_PNIOWEK5) = 1.0
3437            END IF
3438          END IF
3439       END IF
```

Figure A.3: Initializing tracers at single cells. Names are PNIOWEK3-5

```
3394       IF (config_flags%tracer_opt .eq. 2) THEN
3395        IF (grid%id == 3) THEN
3396           DO j = jds + 90, jds + 98, 1
3397             DO i = ids + 95, ids + 100, 1
3398                IF ( its .LE. i .and. ite .GE. i .and. jts .LE. j .and. jte .GE. j ) THEN
3399                  tracer(i, 1, j, N_SLV)  = 1.0
3400                END IF
3401             END DO
3402           END DO
3403        END IF
3404       END IF
```

Figure A.4: Initializing tracers at multiple cells. Tracer name is N_SLV with quantity 1.0

WRFV3/dyn_em/solve_em.F

Tracers are initialized in WRF but are not yet continuous i.e. tracers are only released once at the beginning of the simulation. With changes regarding the namelist.input in the next section WRF runs without changing anything in `solve_em.F`. In order to release tracers every timestep `solve_em.F` needs to be adapted. Somewhere around line 263 right after the line `ALLOCATE (max_horiz_cfl_tmp(grid\%num_tiles))` the following lines to be inserted for every tracer initialized earlier:

```
307    ! PniowekIII
308 IF ( config_flags%tracer_opt == 2 ) THEN
309    IF (grid%id == 3) THEN
310      i = 96
311      j = 99
312      IF (ips .LE. i .and. ipe .GE. i .and. jps .LE. j .and. jpe .GE. j ) THEN
313       tracer(i, 1, j, P_PNIOWEK3) = tracer(i, 1, j, P_PNIOWEK3) + 1.0
314      END IF
315    END IF
316 END IF
```

Figure A.5: Continuous tracer in solve_em.F. Tracer = Tracer +1 to prevent WRF from overwriting backflown tracer information.

WRFV3/test/em_real/namelist.input

```
tke_adv_opt                         = 2, 2, 2, 2,
do_avgflx_em                        = 1, 1, 1, 1,
tracer_opt                          = 2, 2, 2, 2,
/
```

Figure A.6: Tracers have to be turned on in the namelist.input. Every domain in which tracers are allowed should have the flag 2.

Increase WRF output

It is useful to increase the output-interval independent from the internal (namelist-given) output-interval of WRF. Designated variables can then be written to a new file. In namelist.input the following lines are added to the `&time_control` section:

```
iofields_filename                   = "myoutfields_d01.txt", "myoutfields_d02.txt", "myoutfields_d03.txt",
ignore_iofields_warning             = .true.
io_form_auxhist24                   = 2,
auxhist24_interval                  = 10, 10, 10, 10,
io_form_auxhist23                   = 2,
auxhist23_interval                  = 720, 720, 720, 720,
```

Figure A.7: Increase output to 10min. interval for auxhist24 and to 12h for auxhist23.

The files `myoutfields_d0X.txt` are domain specific and should look like:

```
+:h:24:T2,PSFC,PH,PHB,T,U10,V10,U,V,W,PNIOWEK3,PNIOWEK4,PNIOWEK5,BORYN,KRUPI,SILES,RYDUL,JASTZR4,JASTZR6,SOSNI,DULCZ
+:h:23:HGT,LANDMASK
```

Figure A.8: myoutfields_d03.txt: Increased output intervall for the variables 2m temperature, surface pressure, perturbation geopotential, base state geopotential, 10 meter wind U and V, windcomponents u, v, and w and finally the tracers.

The resulting files are called `auxhist23...` and `auxhist24...`.

Appendix B

S5P TROPOMI data compared to FTS observations

This work presents already retrieved TROPOMI XCH_4 observations of an early stage (level 2) without giving details on the retrieval. The finished XCH_4 TROPOMI data product may be different compared to the presented data.

The EM27/SUN calibration against the KIT TCCON instrument enables the TROPOMI XCH_4 validation with respect to TCCON. This study considers the level two data of the TROPOMI XCH_4 product. At this stage, the satellite data shows an albedo dependency which is apparent in Figure B.3, as areas with generally higher albedo (deserts such as the Sahara or the Australian outback) also indicate higher XCH_4 values than other regions of the earth. This might be related to uncertainties of the light-path caused by aerosols. The TROPOMI data product at the time of this study is not yet suitable in terms of absolute total column measurement comparisons. Hence, it is possible to compare regional gradients as for example in the USCB where the overall albedo variability is generally lower compared to the global albedo variability.

Sentinel-5 Precursor overpasses the USCB once per day around noon resulting in an observational time for 7 June 2018 at 11:15 UTC (Figure 6.1). Assuming cloud free conditions, TROPOMI allows for one comparison possibility per day for each stationary ground-based instrument. Other, erstwhile satellite methane products e.g. from the Japanese Greenhouse Gases Observing Satellite (GOSAT) have a sparser spatial sampling of up to 100 km between two consecutive measurements (Butz et al., 2011) and they do not measure the same pixels at every orbit.

To further increase comparison possibilities, every TROPOMI pixel within 0.1° distance to each stationary FTS is used to build an average satellite XCH_4 measurement, allowing other pixels, than the one enclosing the stationary FTS to influence the observation. However, clouds either obstructing the FTS or the satellite instrument lead to a total of twelve comparisons between satellite and ground-based data for the campaign period of roughly three weeks.

The left panel in Figure B.1 depicts XCH_4 measurements of the stationary network

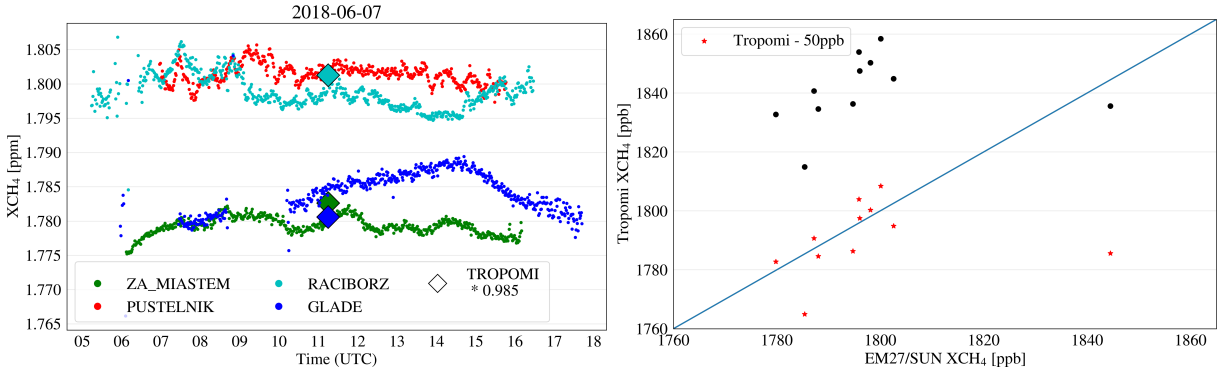

Figure B.1: Left panel: Measurements of the stationary FTS network on 7 June 2018. Colored diamonds refer to scaled TROPOMI data from the respective overpass for each pixel enclosing each FTS location. The rough basin enhancement from east (green) to west (cyan) is visible in both, satellite and ground-based data. The right panel displays the comparison of all simultaneous TROPOMI and ground-based FTS observations. The satellite data reveals a roughly 50 ppb overestimation.

as colored dots from the north (Za Miastem, green), the east (Glade, blue), the south (Pustelnik, red), and the west (Raciborz, cyan) observed on 7 June 2018. The stationary network clearly observes a regional methane gradient as enhancements of the southern (red) and western (cyan) station over the northern (green) and eastern (blue) station. This is expected, as easterly winds dominate the scene and transport the emitted methane towards the west. The respective TROPOMI orbit is depicted in Figure 6.1 and also shows higher methane observations in the west of the USCB indicating a plume following easterly winds. The TROPOMI XCH_4 measurements are indicated as diamonds using the same color as the respective FTS observations in Figure B.1. Scaling the TROPOMI data with a fitting parameter of 0.985 visualizes, that the methane gradient from upwind USCB to downwind USCB has generally the same magnitude of roughly 20 ppb at the time of the satellite overpass.

The right panel in Figure B.1 depicts all available TROPOMI and EM27/SUN comparisons during CoMet. The corresponding TROPOMI orbits are depicted in B.2. The sparse dataset summarized in Fig. B.2 does not allow for a detailed analysis or validation of the TROPOMI instrument but the observations are generally precise in the range of ± 5 ppb considering a systematic residual of about 50 ppb and neglecting two outliers.

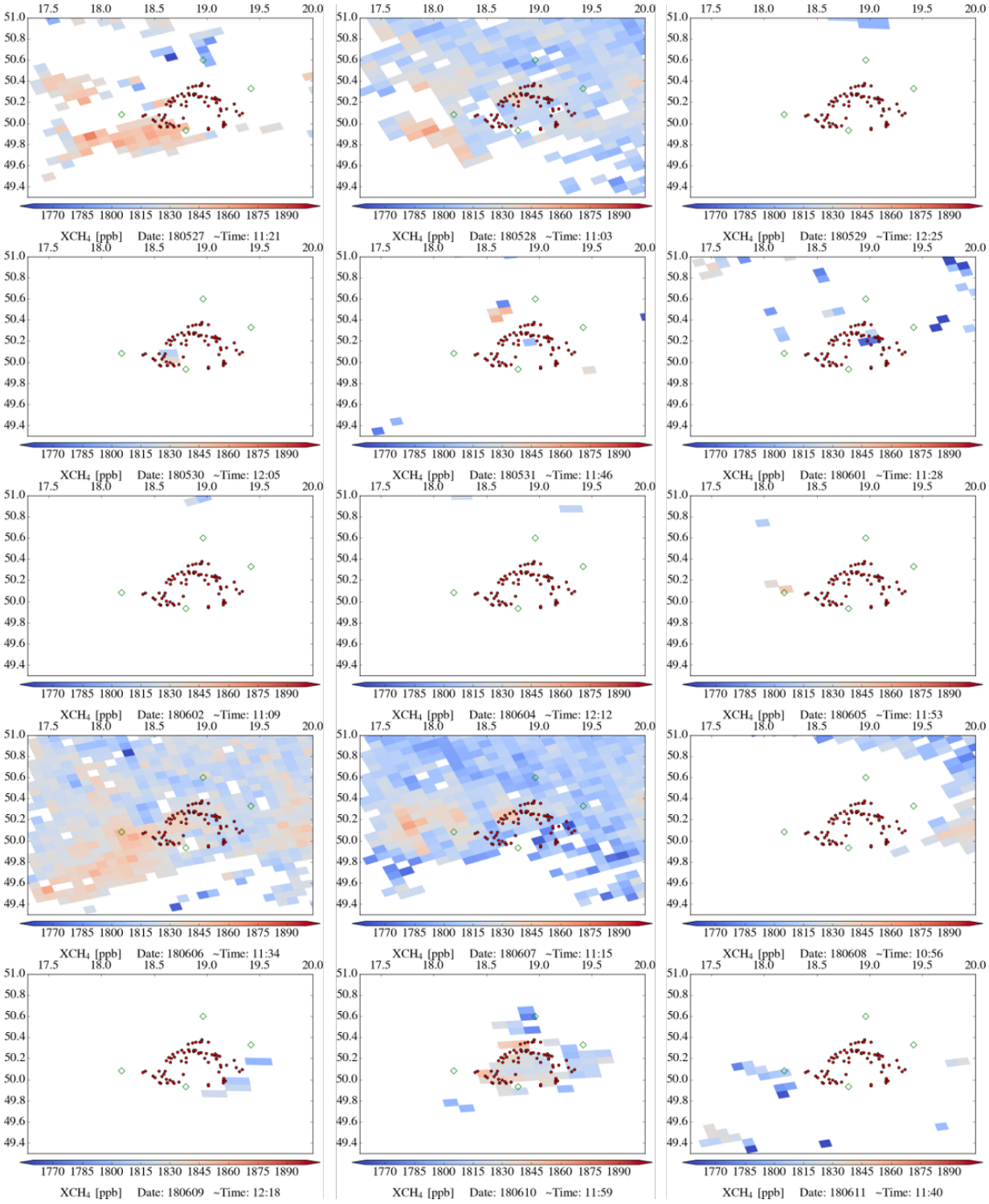

Figure B.2: All TROPOMI overflys during CoMet.

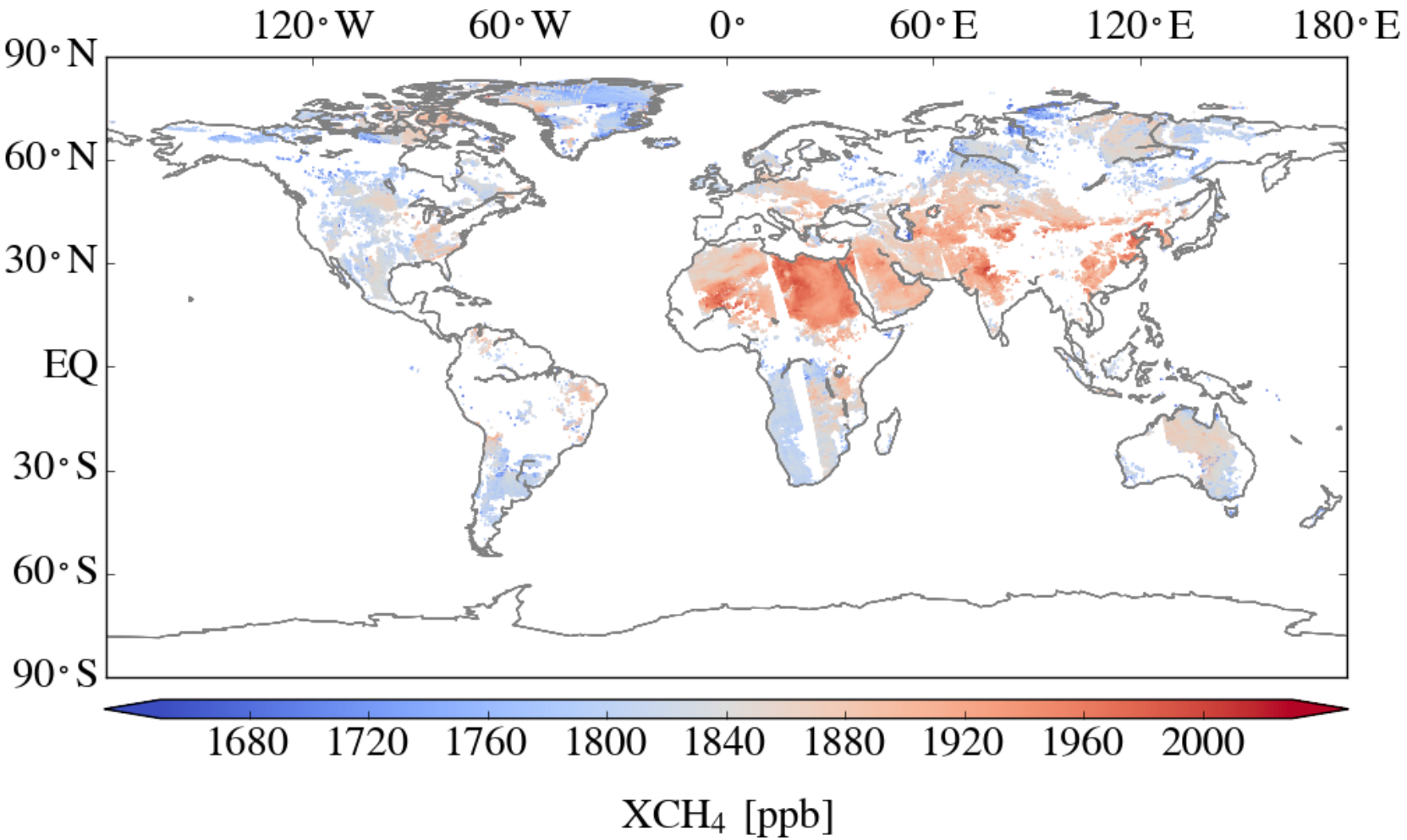

Figure B.3: TROPOMI overfly on 6 June 2018.

Appendix C

Ceilometer measruements during CoMet0.5

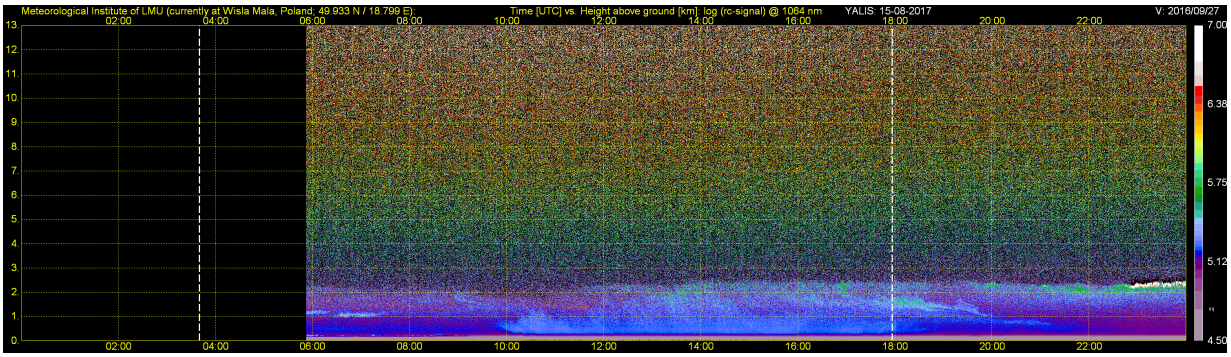

Figure C.1: Ceilometer measurement at station Pustelnik on 15 August 2017. Convection starts to be visible around 10 UTC enhancing the apparent PBL height to roughly 2 km. Around 18 UTC, the PBL starts to decay. Shortly before midnight, some clouds appear as strong backscatter signal.

List of Figures

List of Tables

Acknowledgements

This work used resources of the Deutsches Klimarechenzentrum (DKRZ) granted by its Scientific Steering Committee (WLA) under project ID b1104.
We acknowledge funding for the CoMet campaign by BMBF (German Federal Ministry of Education and Research) through AIRSPACE (grant no. FKZ: 01LK1701A). We thank DLR VO-R for funding the young investigator research group "Greenhouse Gases".

I want to thank Prof. Dr. André Butz for his support and guidance in all kind of situations which appear during the PhD process. I could always be sure, that you really are interested in this work. Thank you for your inspiring knowledge, straightforwardness and honesty.

I sincerely thank Prof. Dr. Mark Wenig for reviewing this thesis.

I want to thank Prof. Dr. Markus Rapp, Dr. Hans Schlager, and Dr. Anke Roiger for the possibility to work at the IPA, DLR in Oberpfaffenhofen and to have access to many different atmospheric research fields only a few steps apart. In addition, I want to thank Dr. Anke Roiger for useful suggestions and for leading the young investigator group on greenhouse gases, where I received a warm welcome.

The CoMet FTS activities would not have been possible without the personnel and technical support from: Frank Hase, Matthias Frey, and Darko Dubravica (KIT), Jia Chen, Andreas Forstmaier, and Florian Dietrich (TU Munich), Christoph Knote and Matthias Wiegner (LMU), Alexandru Dandocsi (INOE2000), Leon Scheidweiler (IUP Heidelberg), Sebastian Wolff (DLR), Sara Defratyka (LSCE), Jarek Necki, Justyna Swolkien, Michal Kud, Pawel Pagoda, Mila Stanisavljevic (AGH).

I sincerely want to thank Ralph Kleinschek for answering all my questions, for talking about anything and everything, for working on the same project, and in particular, that i now know things such as that people used to ice skate on hog lard before they were able to maintain natural ice with cooling technologies.

Speaking for the arrangement of instrument shipments, rentals, estimates, invoices and basically everything which needs a lot of experience, I sincerely thank Susanne Flierl for her enthusiasm. The same applies for Winfried Beer on the technical side, who always gave immediate support.

Certainly, I will miss the chats, and discussions at the blackboard (and at the dartboard) with Jonas, Julian, Johan and Dennis. Discussing a random problem with a few sketches is, what I will miss the most. I also want to thank all the nice people I met during my time at DLR and who are part of the reason I started drinking more and more coffee.

Josef, Franzi, Lukas, Steevy, Simon, Julia, Ayra, Nec, Nina, Hänni, Lucky, Ferdl, Schausi, Mutschi, Hossein, i can always count on you. THANK YOU!

My parents Wolfgang and Annemarie and my sister Julia do not stop supporting me unconditionally. And yes grandma, I'm finally done with my studies but I'm still not sure what you mean by 'getting a real job now' ;-)

Anna-Lena, Deine Freude, Dein Großmut, Deine Geduld, Deine Würde und Deine Liebe sind nicht von dieser Welt. Danke, dass wir unsere Liebe und unser Leben teilen dürfen ☆